Photoelectrocatalytic Water Splitting on Tungsten (VI) Oxide Films Prepared by Supercritical Deposition in a Cold-wall Reactor and by a Hydrothermal Technique

By

Gözde Tekeli

A Dissertation Submitted to the

Graduate School of Sciences and Engineering

in Partial Fulfillment of the Requirements for

the Degree of

Master of Science

in

Chemical and Biological Engineering

KOÇ
UNIVERSITY

August, 09 2018

MSc Thesis

Koç University

Graduate School of Sciences and Engineering

This is to certify that I have examined this copy of a master's thesis by

Gözde Tekeli

and have found that it is complete and satisfactory in all respects, and

that any and all revisions required by the final

examining committee have been made.

Committee members:

Prof. Can Erkey (Advisor)

Asst. Prof. Sarp Kaya (Co-advisor)

Assoc. Prof. Uğur Ünal

Asst. Prof. Zeynep Ülker Demir

Asst. Prof. Erdal Uzunlar

Date: 09.08.2018

to my beloved mother…

ABSTRACT

Energy demand is growing and there is a vital need to find new energy sources that are sustainable, clean, and renewable. Hydrogen that is produced from water has been considered as one the most promising energy sources for decades. One of the technologies for production of hydrogen from water is photoelectrochemical water splitting where water and sunlight react on photocatalytic surfaces. In this manner, photoelectrochemical cell (PEC) configurations have been developed for the photo-electrolysis of water within a photoelectrode which is used both to absorb the light and also to catalyse the splitting of water into hydrogen and oxygen. Many studies have concentrated on development of photocatalytic materials for this purpose. Tungsten (VI) trioxide (WO_3) is a promising photoelectrode material since it has an appropriate band gap and high stability in acidic conditions.

In this study, supercritical fluid deposition method (SCD) was developed as an alternative technique to produce WO_3 films on a conductive glass, fluorine doped tin oxide (FTO) for photoelectrochemical water splitting. For this purpose, a cold-wall reactor was designed for deposition of the films onto heated substrates from supercritical solutions at substantially lower temperatures than the substrate temperature. WO_3 films were deposited using 0.4 wt.% tungsten hexacarbonyl ($W(CO)_6$) solutions in supercritical CO_2. Four types of deposition procedures were investigated with no additional oxygen (O_2) gas and with addition of O_2 in different steps of the deposition. Depositions were carried out at 8.27 MPa CO_2 and a heating stage temperature of 300 °C for each method. Coating of the FTO surface were confirmed via scanning electron microscopy (SEM) and energy dispersive X-ray analysis. SEM results indicated that the produced films were very thin (most probably less than 100 nm). For some cases, SEM analysis from cross-sectional view showed the incomplete film growth on some parts of the sample. Structure of the WO_3 films were determined as mixtures of monoclinic WO_3 and an unknown phase of tungsten oxide species with a different state of tungsten from the analysis results of the grazing incidence X-ray diffraction spectra. Photoelectrochemical characterization was performed with cyclic voltammetry method under illumination at 1.0 sun AM 1.5 G in 1 M sulfuric acid solution (H_2SO_4) with and without using 10 vol.% methanol as a hole scavenger. The best photocurrent was obtained as 0.0225 mA/cm^2 at 1.23 V from the film produced with the addition of oxygen before starting the deposition in 1 M H_2SO_4. Increase in the photocurrent activity was observed with the addition of hole scavenger to the electrolyte. To make comparison between the films deposited by conventional method and new developed supercritical carbon dioxide technique, hydrothermal synthesis of WO_3 films were performed. Films were deposited by direct growth on FTO substrate and by drop casting of a colloidal solution of WO_3 powder. The effect of the post calcination and hydrothermal reaction period on the film structure and morphology were investigated. The best method was determined as the 6 h reaction time and annealing at 500 °C for 1 h. The highest photocurrent was obtained as 0.76 mA/cm^2 in 1 M H_2SO_4 from the film which was produced by drop casting.

ÖZET

Enerji talebi arttıkça, sürdürülebilir, temiz ve yenilenebilir yeni enerji kaynakları bulmak önemli bir ihtiyaç haline gelmiştir. Sudan üretilen hidrojen, uzun süredir en çok umut vaad eden enerji kaynaklarından biri olarak kabul edilmektedir. Sudan hidrojen üretim teknolojilerinden biri, fotokatalitik yüzeylerde su ve güneş ışığının reaksiyona girdiği fotoelektrokimyasal su ayrıştırmadır. Bu şekilde, hem ışığı absorbe etmek hem de suyun hidrojen ve oksijene ayrılmasını katalize etmek için kullanılan bir fotoelektrot içindeki suyun foto-elektrolizi için fotoelektrokimyasal (PEC) hücre konfigürasyonları geliştirilmiştir. Birçok çalışma bu amaç için fotokatalitik materyallerin geliştirilmesi üzerinde yoğunlaşmıştır. Tungsten (VI) trioksit (WO_3), uygun bir bant aralığına ve asidik koşullarda yüksek stabiliteye sahip olduğu için umut verici bir fotoelektrot materyalidir.

Bu çalışmada, fotoelektrokimyasal su ayrışımı için bir iletken cam, flor katkılı kalay oksit (FTO) üzerinde WO_3 filmlerin üretilmesi için alternatif bir teknik olarak süperkritik deposizyon (SCD) yöntemi geliştirilmiştir. Bu amaçla, filmlerin ısıtılmış substratlar üzerine, substrat sıcaklığından önemli ölçüde daha düşük sıcaklıklarda olan süperkritik çözeltilerden deposizyonu için bir soğuk-duvar reaktörü tasarlanmıştır. WO_3 filmleri, süperkritik CO_2 içinde ağırlıkça % 0.4 tungsten hekzakarbonil $(WCO)_6)$ çözeltileri kullanılarak sentezlendi. Ek oksijen (O_2) gazı olmaksızın ve çökeltinin farklı adımlarında yapılan O_2 ilavesiyle dört tip sentezleme yöntemi incelendi. Her bir yöntem için 8.27 Mpa basınçta CO_2 ve 300 ° C de bir ısıtma zemini sıcaklığında sentezler gerçekleştirilmiştir. FTO yüzeyinin kaplanması, taramalı elektron mikroskobu (SEM) ve enerji dağılımlı X-ışını analizi ile doğrulanmıştır. SEM sonuçları, üretilen filmlerin çok ince (muhtemelen büyük olasılıkla 100 nm'den az) olduğunu gösterdi. Bazı durumlarda, kesitsel görünümden elde edilen SEM analizi, numunelerin bazı kısımlarında tamamlanmamış film büyümesi olduğunu gösterdi. WO_3 filmlerinin yapısı, X-ışını kırınım spektrumlarının analiz sonuçlarından, farklı bir tungsten durumu olan, monoklinik WO_3 ve bilinmeyen bir tungsten oksit türü fazı olarak belirlenmiştir. Fotoelektrokimyasal karakterizasyon, 1 M sülfürik asit çözeltisi (H_2SO_4) içinde 1.0 güneş AM 1.5 G'de bir ışık tutucu olarak % 10 hacim metanol ile ve methanolsuz kullanıldıklarında ışık altında döngüsel voltametri yöntemiyle gerçekleştirildi. En iyi foto-akımı, 1 M H_2SO_4 içinde, deposizyon başlamadan önce oksijen ilave edilerek üretilen filmden 1.23 V'de 0.0225 mA/cm^2 olarak elde edildi. Elektrotata delik tutucu eklenmesi ile foto-akım aktivitesinde artış gözlemlendi. Geleneksel yöntemle sentezlenen filmler ile yeni geliştirilmiş süperkritik deposizyon arasında karşılaştırma yapmak için, WO_3 filmlerinin hidrotermal sentezi gerçekleştirilmiştir. Filmler, FTO substratında doğrudan büyüme ve WO_3 tozunun bir kolloidal çözeltisinin damla dökülmesiyle sentezlenmiştir. Post kalsinasyon ve hidrotermal reaksiyon periyodunun film yapısı ve morfolojisi üzerindeki etkisi araştırıldı. En iyi yöntem 6 saat reaksiyon süresi ve 1 saat 500 ° C'de tavlama olarak belirlenmiştir. En yüksek foto-akımı, damla dökümle üretilen filmden 1 M H_2SO_4 içinde 0.76 mA/cm^2 olarak elde edildi.

ACKNOWLEDGEMENT

First, I would like to thank to my advisor, Prof. Dr. Can Erkey for giving me to chance to work on such a unique research project. It was a great honour to conduct my MSc degree within great guidance. I always was enjoyed while discussing with him since the conversations were ended up with creative ideas. Most importantly, he taught me not to act hastily since working in a research field is long-time journey.

Second, I would like to thank to my co-advisor Asst. Prof. Sarp Kaya for being such a kind and helpful in any time no matter how he was busy. It was a blessing for me to work and meet with him. He behaved me not only as a student but also as a friend. He will be my role model for the rest of my carrier and whenever I felt desperate in my works, I will remind to myself his dedication, self-discipline and hard working. He always encouraged me to push the boundaries and guide me to overcome the problems.

I also would like to thank to committee members, Assoc. Prof. Uğur Ünal, Asst. Prof Zeynep Demir Ülker and Asst. Prof. Erdal Uzunlar to sparing their valuable time and considerations with me.

I want to also offer my thanks to members of Koç University Surface Sciences Laboratory (KUYTAM), Dr. M. Barış Yağcı and Dr Ceren Akkaya to help us in our sample characterizations.

I have special thanks to Dr. Selmi Erim Bozbağ for spending his valuable time to conduct my experimental set-up and guiding me throughout my project.

I also would like to our Energy Technologies and Supercritical Fluids Research Group members, Yaprak Özbakır, Shadi Khan Baloch, Zeynep İnönü, Faheem Ahmad, Umaima Saleem, Seçil Ünsal, Işk Sena Akgün, İbrahim Şahin, Şansım Bengisu Barım and Hande Güneş,

I also offer my thanks to Sarp Kaya’s group members, Mahsa Barzgar Vishlaghi, Sonia Mobassem, Hana Zarenezhad, Mohammad Panahi, Navid Solati, Timuçin Balkan, Cüneyt Karakaya, Dilan Aksoy, Amir Rahimi, Haseeb Ullah, and Sinem Apaydın.

I also special thanks to amazing friends that I made here Işık Sena Akgül, Betül Şeker and Sinem Apaydın. They made Istanbul more valuable for me.

I have also special thanks to my dear friends from METU, Eşenur Kırkoğlu and Ezgi Kuru. I would not change spending time with them for a world. I also want to thank my friends from high school, Büşra Kaya, Gencay Gül, Tufan Buğra Özkan and Ilgın Ulular for their support and believing in me.

I also want to thank my family: my father Vefa Tekeli, my brother Orhun Tekeli and my twin sister Hande Tekeli who always showed love and supported me in my entire life. They were tried to make things easier for me all the time. I always felt grateful for having such a wonderful family.

I was also grateful to my soul mate, Can Köksal for his endless support and love. He was always patient, kind and helpful. He never got bored listening my complaining about my research. He never hesitated the spend his time to come Istanbul from Ankara.

Finally, I dedicated this thesis to my mother who is watching me from the sky. Thank you for being such a great mother and role model. Without her, I could not be such a strong woman.

TABLE OF CONTENTS

LIST OF TABLES

LIST OF FIGURES

NOMENCLATURE

$E^{o}_{Ag/AgCl}$	*standard potential of $E_{Ag/AgCl}$ (V)*
$E_{Ag/AgCl}$	*potential with respect to Ag/AgCl reference electrode (V)*
E^{0}_{ox}	*standard oxidation potential*
E^{0}_{red}	*standard reduction potential*
Mw_{CO_2}	*molecular weight of the carbon dioxide*
$Mw_{W(CO)_6}$	*molecular weight of the tungsten hexacarbonyl*
n_{CO_2}	*moles of the carbon dioxide*
$n_{W(CO)_6}$	*moles of the tungsten hexacarbonyl*
B	*full width at half maximum (radians)*
CV	*cyclic voltammetry*
E	*potential (V)*
$E_{(RHE)}$	*potential with respect to reversible hydrogen electrode (V)*
EDX	*energy dispersive x-ray spectroscopy*
Eg	*band gap energy (eV)*
F	*faraday's constant (C/mol)*
$F(R_\infty)$	*Kubelka-Munk function*
GIXRD	*grazing incidence X-ray diffraction*
h	*Planck's constant*
HER	*hydrogen evolution reaction*
K	*Scherrer's constant*
L	*crystalline size (nm)*
M	*constant (depends on optical transition)*
n	*moles of electrons*
NHE	*normal hydrogen electrode*
OER	*oxygen evolution reaction*
P	*pressure*
P_c	*critical pressure*
PEC	*photoelectrochemical cell*
PS	*particulate system*

R_∞	*ratio of the reflectance of a sample to the reflectance of the standard*
RHE	*reversible Hydrogen Electrode*
$scCO_2$	*supercritical carbon dioxide*
SCD	*supercritical deposition*
SCFD	*supercritical fluid deposition*
SEM	*scanning electron microscopy*
T	*temperature*
T_c	*critical temperature*
Tstage	*temperature of the heating stage*
Tvessel	*temperature of the cold-wall reactor*
V_{vessel}	*volume of the hot-wall reactor*
y	*solubility of the tungsten hexacarbonyl (mol/mol)*

Greek Letters

ρ_{CO_2}	*density of the carbon dioxide*
α	*absorption coefficient*
ΔG	*change of Gibbs (free) energy*
θ	*Bragg's angle*
λ	*wavelength of the X-ray (nm)*
ν	*frequency*

Chapter 1

INTRODUCTION

Energy demand of the world is increasing, and we still largely rely on fossil fuels. BP Statistical Review of World Energy (2017) reported that crude oil is the dominant fuel for the energy supply although it is decaying due to increasing trend of natural gas as seen in Figure 1.1 [1].

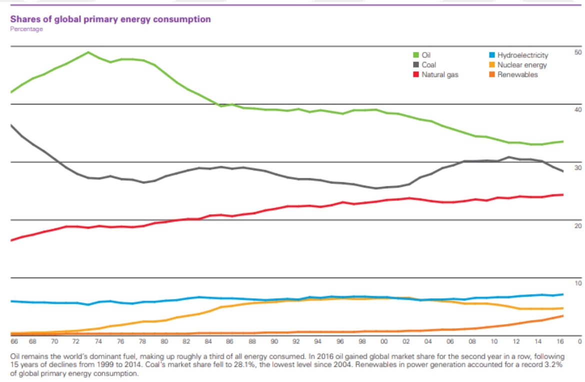

Oil remains the world's dominant fuel, making up roughly a third of all energy consumed. In 2016 oil gained global market share for the second year in a row, following 15 years of declines from 1999 to 2014. Coal's market share fell to 28.1%, the lowest level since 2004. Renewables in power generation accounted for a record 3.2% of global primary energy consumption.

Figure 1.1 Global Energy Consumption Shares [1].

The growth in energy consumption, limited source of fossil fuels, harmful impact of traditional energy production methods on environment which yields to increase in CO_2 level in the atmosphere and economic considerations are forcing us to find new renewable, clean and sustainable energy sources.

The sun, the main energy source of our planet, is considered as a renewable and sustainable energy source for decades. However, the utilization of the energy of the sun has some challenges in terms of conversion and storage of its energy. Although we have commercial solar technologies such as solar photovoltaics, concentrating solar power plants, and solar thermal systems, daily and seasonal availability of sunlight forces us to store solar energy [2,3].

A solution can be to mimic a process in the nature which is photosynthesis. Using sunlight as plants do in the photosynthesis cycle, we can split water into hydrogen and oxygen photoelectrochemically. Thus, solar energy can be captured in the chemical bond of hydrogen. This process, called as solar water splitting, has become the 'Holy Grail' of chemistry. In this way, hydrogen can be produced from a clean route since the reactant (water) and by-product (oxygen) are non-toxic for the environment [3].

From a thermodynamic aspect, solar water splitting consists of two half reactions: oxygen evolution reaction (OER) and hydrogen evolution reaction (HER).

In alkaline solutions, these reactions are as follows [4]:

$$4H_2O + 4e^- \leftrightarrow 2H_2 + 4OH^- \qquad E^0_{red} = -0.828\,V\ vs.NHE \qquad (1.1)$$

$$4OH^- + 4h^+ \leftrightarrow 2H_2O + O_2 \qquad E^0_{ox} = -0.401\,V\ vs.NHE \qquad (1.2)$$

For acidic solutions the reactions are as follows [4].

$$4H^+ + 4e^- \leftrightarrow 2H_2 \qquad E^0_{red} = +0.000\,V\ vs.NHE \qquad (1.3)$$

$$2H_2O + 4h^+ \leftrightarrow 4H^+ + O_2 \qquad E^0_{ox} = -1.229\,V\ vs.NHE \qquad (1.4)$$

From the standard cell potential, standard Gibbs free energy change of the system can be determined by using the equation below [4]:

$$\Delta G = -nFE^0 \qquad (1.5)$$

For water splitting, $\mathrm{E}^0 = -1.229\,\mathrm{V}$ and change of Gibbs free energy is found as +237 kJ/mole H_2 from Eqn. (1.5). Gibbs energy shows us this reaction is nonspontaneous thermodynamically.

Photoelectrochemical cell (PEC) configurations are developed for the photo-electrolysis of water within a photoelectrode which is used both absorb the light and catalyst for water splitting reaction. The main advantage of this device is that evolution of hydrogen and oxygen occur on different electrodes, so there is no need for an extra step to separate these gases. Secondly, hydrogen reactions occur at room temperature which demolishes the need for large solar concentrator and limitation of space for it [4].

In the photoelectrochemical cell, the reaction takes place on the interface of the photoelectrode surface and electrolyte. Three major steps are necessary for the reaction to happen which are [5]:

(i) Absorption of photons from sunlight to generate electrons and holes
(ii) Disintegration and migration of the excited charges to the surface reaction sites (these charges can migrate to the surface or recombine on the surface or in the bulk)
(iii) OER and HER reactions occur on the reaction sites

In this process, electrons get excited from valence band (VB) to the conduction band (CB) and in that state, they leave the holes behind as illustrated in Figure 1.2. For the HER reaction, CB must have more negative potential level than the hydrogen reduction potential. For the OER reaction, VB must have a less positive potential than the redox potential of oxidation reaction of water [6].

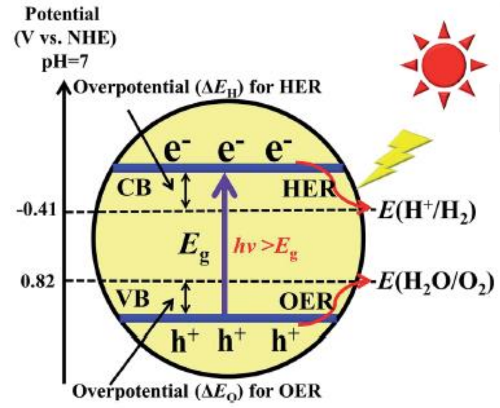

Figure 1.2 Photocatalytic water splitting process on the surface of a catalyst [6].

In general, semiconductors are suitable to use as photoelectrodes due to their band gap structure. In the relationship between semiconductor band structure and reduction potentials of water, some of the materials are suitable for water oxidation and are classified as photoanode.

For the photoanode activity, the reaction mechanism of OER is important since it effects the reaction kinetics. The exact OER mechanism is not known, but some mechanisms were proposed, and it shows different pathways in alkaline and acid solutions.

The most widely accepted pathway of the OER reaction on metals and oxides was a four-step reaction mechanism which was proposed by Man *et al.* (2011) and it is as follows:

$$H_2O_{(l)} + * \leftrightarrow HO^* + H^+ + e^- \qquad (1.6)$$

$$HO^* \leftrightarrow \; O^* + H^+ + e^- \qquad (1.7)$$

$$O^* + H_2O_{(l)} \leftrightarrow HOO^* + H^+ + e^- \qquad (1.8)$$

$$HOO^* \leftrightarrow * + O_{2_{(g)}} H^+ + e^- \qquad (1.9)$$

HO*, O*, HOO* are the reaction intermediates and * is the active site of the surface. For an ideal case, Gibbs' free energy of each steps are same having a same potential of 1.23 eV theoretically at zero potential at standard conditions. The ideal oxygen evolution catalyst conducts the OER over this potential. In real case, differences in binding energies of HO*, O*, HOO* on the surface of a catalyst creates variances in Gibb's free energy of each steps which are causing the limitations for the OER activity [7].

Photoelectrochemical water splitting was first accomplished by Honda and Fujishima using TiO_2 as a photoelectrode [8]. After this achievement, scientists have developed new materials as both photoanode and photocathode. New developed electrodes should have a suitable band gap to absorb sunlight in visible region, specific band-edge position for the reaction of water splitting, high stability and durability to photo-corrosion, high efficiency, and low production cost to meet requirements of engineering [9]. TiO_2, $SrTiO_3$, WO_3, Fe_2O_3 metal oxides and ZnO are suitable for oxygen evolution [3].

For the oxidation of water, WO_3, Fe_2O_3, and $BiVO_4$ are good candidates since they exhibit high activities and stabilities [6]. WO_3 is a promising material due to its competence of absorbing light in the visible region owing to its band gap (2.7 eV). Also, it shows high stability in acidic aqueous solutions [10]. In 1976, Hodes, Cahen and Manassen reported WO_3 as a photoanode [11]. From that day on, people have focused on the production of WO_3, since the morphology and the crystal structure are decidedly effective for a better incident photon to electron conversion efficiency (IPCE). Scientist developed methods mostly to make nanostructured WO_3 materials (e.g. nanotubes, nanowired, nanoplatelets), since they have higher interfacial contact area [10]. There are several conventional coating techniques to prepare nanostructured WO_3 film on a conductive substrate (e.g. fluorine doped tin oxide (FTO)indium tin oxide (ITO)) such as sol–gel[12–19], anodization [20–23], solvothermal[24,25], hydrothermal [9,26–31], electrodeposition [32,33], atomic layer deposition (ALD) [34], spray pyrolysis (C-doped WO_3) [35], flame vapor deposition (FVD) [36], chemical vapor deposition (CVD) [37,38].

Hydrothermal synthesis method is a very common coating method used to make photoelectrodes. Low equipment and precursor cost are the advantages of hydrothermal growth. One of the most important reasons for using this method to make photoelectrodes is that the possibility of producing films with high surface area which leads to high activity. In literature, there are two different ways to produce WO_3 photoelectrodes using hydrothermal synthesis. First one is the direct growth of WO_3 film on the conductive glass (ITO or FTO) [9,39] or on WO_3 seed layered conductive glass [29] and direct growth of WO_3 from tungsten sheet inside an autoclave [27]. Second method is the production of nanoparticles by hydrothermal technique and preparation of the films from the colloidal solution of the obtained powder with a binding agent [26,30].

Besides the methods mentioned above, supercritical fluid deposition is an alternative process to prepare thin metal films [40–43], metal oxides [44–46] and semiconductor materials [47] with high purity. The advantage and most interesting aspect of the supercritical fluid is that it shows mixed thermophysical properties belong to liquids and gases. Liquid-like density of SCF leads to high concentrations of precursors and its gas-like viscosity provides high diffusion rate [48]. Supercritical fluids provide higher mass transfer rates with low surface tension which allow SCF to penetrate and wet of substrate’s pores better [49].

To the best of our knowledge, no studies exist on production of WO_3 film by supercritical fluid deposition and usage of FTO as a substrate for this deposition. According to the film growth mechanism of supercritical fluid deposition [49], the first condition is to use a W-metallic precursor soluble in $scCO_2$. Secondly, when the solution is contacted with the FTO substrate, it should adsorb on the surface. Then, surface reaction occurs and bonds between the W-precursor and its ligands should be broken by heat. Finally, film nucleation and growth occur while the volatile products are desorbed from the surface.

In this study, we demonstrated the development of a new supercritical fluid deposition technique in a cold-wall reactor for WO_3 thin film production on a conductive glass (FTO). For comparison purposes, hydrothermal synthesis technique as a conventional method was also studied to produce WO_3 films on FTO. Hydrothermal synthesis of WO_3 film directly on FTO and WO_3 film preparation from colloidal solution of hydrothermally synthesized WO_3 nanoparticles were performed.

Characterization methods for the prepared samples were UV–visible spectroscopy, Raman spectroscopy, Grazing incidence X-ray diffraction (GIXRD), scanning electron microscopy (SEM), energy dispersive x-ray spectroscopy (EDX), and cyclic voltammetry (CV).

The studies for produced WO_3 films via hydrothermal synthesis method for water splitting and their activities were covered in Chapter 2. For the production of WO_3 film via SCD technique, solubility measurements of the compounds in $scCO_2$, cold-wall reactor designs for $scCO_2$ deposition and metal oxide films prepared by supercritical fluid deposition were investigated in this chapter.

Chapter 3 gives information about the materials and methods. Preparation of WO_3 film for both hydrothermal and supercritical deposition methods were explained in detail.

Chapter 4 clarifies material and photoelectrochemical characterization result and discussion of the prepared WO_3 films.

Conclusions obtained from this study and future work that might be done for the development of the $scCO_2$ production method for the WO_3 film is examined in detail in Chapter 5.

Chapter 2

LITERATURE REVIEW

2.1 Tungsten (VI) Oxide (WO_3)

WO_3 structure is octahedral with a centre atom tungsten sharing six oxygen atoms on the corners. Five different phases have been reported for the crystallography of the WO3 from 0 K to its melting point temperature, 1700 K. From low temperature to high temperature, its structure changes as following: ε -WO_3 (monoclinic, 0-230 K), δ -WO_3 (triclinic, 230-290 K), γ -WO_3 (monoclinic, 290-600 K), β -WO_3 (orthorhombic, 600-1170 K), α -WO_3 (tetragonal, 1010-1170 K) [50]. β -WO_3 and α -WO_3 forms are not stable when they are cooled to room temperature whereas γ -WO_3 and δ -WO_3 keep their crystal structure [51].

Nanostructured WO_3 can be synthesized from solution-based methods using generally ammonium metatungstate ($(NH_4)6H_2W_{12}O_{40} \cdot xH_2O$) [26,52] , tungstic acid [13] as tungsten sources and also from the tungsten metal foil or sheets (W) [27] via hydrothermal, sol-gel and anodization methods. WF_6, WCl_6 and $W(CO)_6$ have been used as precursors for the chemical vapor deposition of WO_3 [53]. Stoichiometry of the deposited materials can generally be determined from the color of the films. If the oxygen content is low, black color is observed. When the x=2.7±0.2 in WO_x, translucent dark blue films are obtained. WO_3 films appear as pale green-yellow color [51].

WO_3 is a n-type semiconductor having a wide band gap. The band gap of the WO_3 lies between the valance band which is essentially composed of O 2p orbitals fully filled and conduction band which is formed mostly from the empty orbitals of W 5d. The Fermi level is positioned within the middle of the band gap [54]. The electronic band gap (Eg) varies between 2.60 eV to 3.25 eV. The band gap of the nanostructured WO_3 typically increases when the grain size reduces [51].

WO3 films are widely used to make smart windows, electrochromic displays and gas sensors [51]. In recent years, they have been very attractive to make dye-sensitized solar cell (DSSC) and photoelectrodes for the photocatalytic purposes.

2.2 Hydrothermal Method

Hydrothermal process is one of the most commonly used techniques to prepare nanostructured materials. As K. Byrappa (2007) defined the hydrothermal process as '…any heterogeneous reaction in the presence of aqueous solvents or mineralizers under high pressure and temperature conditions to dissolve and recrystallize (recover) materials that are relatively insoluble under ordinary conditions (p.118).

Hydrothermal technique provides high rates of reaction, better nucleation and shape control while operating at low temperatures in aqueous solutions. Metals, metal oxides, semiconductors, metal sulphides and carbon nanotubes can be synthesized using this technique . Capping agents, surfactants and other organic molecules are usually used for the surface alteration. Reactions are carried out in a reactor also known as autoclave, pressure vessel or high-pressure bomb, which must provide high resistance to the corrosive solvents. For the protection of vessel from the corrosive region, a Teflon lining is usually employed [55].

As the interest in the nanostructured materials increased, the hydrothermal method was improved. Hydrothermal synthesis of semiconducting metal oxide, WO_3 has also attracted great attention since it has a wide application range such as electrochromic, gas detecting and photocatalytic.

2.2.1 Hydrothermal synthesis of WO_3 Film and Utilization of Methods for PEC systems

Many studies have been revealed about the impact of the parameters such as temperature, experimental period, pH of the solution, particle size on hydrothermal synthesis of WO_3 films for PEC systems since production method is very effective for control of the morphology of the photoelectrodes in terms of structure, crystallinity, and particle size. These properties influence the absorption of the light, charge separation, and transportation-concisely efficiency of the solar-energy conversion [9].

Studies showed that there is a relationship between crystal size and the photoelectrochemical activity [26,52]. Hong *et al*. investigated particle size effect of the hydrothermally prepared WO_3 powders and photoelectrodes by calcination at temperature range of 500 °C to 800 °C for 10 h. They obtained nanocrystals of WO_3 from suspension of ammonium metatungstate in a mixture of distilled water and cetyltrimethylammonium ammonium bromide used as a surfactant. Then, NH_4OH solution was added to adjust pH value around ~8-9. Reaction was performed at 140 °C for 1 day in an autoclave. They used the obtained particles in particulate system (PS), but for the PEC system WO_3 photoanode was prepared on FTO glass by doctor blade method from the mixture of polyethylene glycol (PEG) binder and annealed WO_3 particles. According to their results, increase in crystalline size of the WO_3 electrode in the PEC system leads higher activity up to a point. Figure 2.1 demonstrates 60 nm particle sized WO_3 film had higher activity than the 30 nm one while particle sizes larger than 60 nm showed lower activity. The reason is for that the hole diffusion length is less in small size particles. On the other hand, when the particle size is too small, it favours the recombination [26].

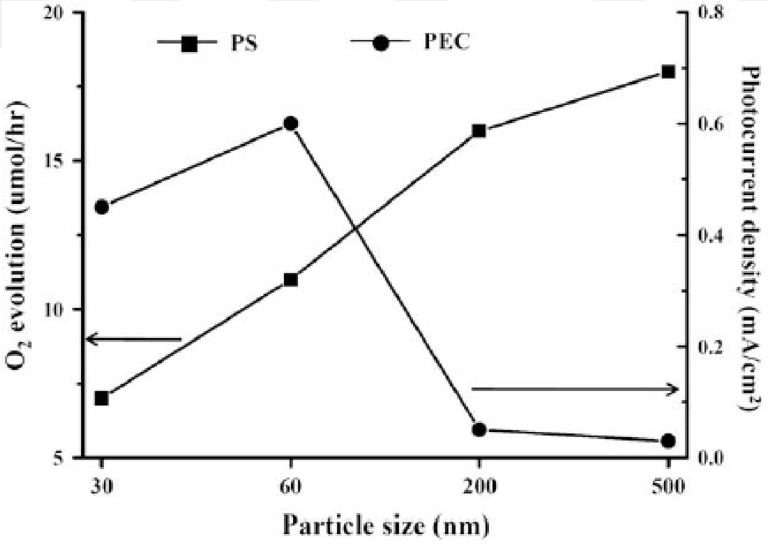

Figure 2.1 Particle size effect of photoactivity in PS and PEC systems [26].

They measured the best activity from the sample having 60 nm spherical nanoparticle (calcinated at 600 °C) as 0.6 mA/cm2 (at 1.2 V vs. NHE) from the back-side illumination with an on-set potential of 0.47 V (vs. RHE) in 0.5 M H_2SO_4 [26]

The studies showed that nanostructured arrays oriented vertically exhibit higher activity compared to the nanoparticle structured materials since they provide better transportation for charges [9,24,28,39]. Furthermore, WO_3 photoelectrodes having 1-D nanostructures will have a higher interfacial contact area than bulk WO_3 [9]. As illustrated in Figure 2.2, the electron pathways of vertically aligned film is direct which provides higher electron transport than the nanoparticle film [28,39].

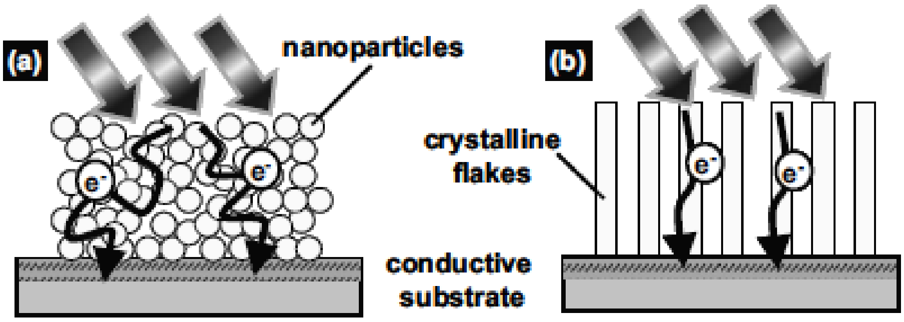

Figure 2.2 The illustration of generated electron transport via illumination along (a) nanoparticle film (b) vertically oriented film [28].

Su *et al*. reported nanowire and nanoflake WO_3 structures vertically aligned on FTO substrate via solvothermal deposition. They used spin coated WO_3 (200 nm) on FTO as a seed layer to initiate the growth. They prepared a solution adding 1.25 g of tungstic acid (H_2WO_4) into 30 ml of distilled water. Then, the solution was heated on a hot plate at 95 °C and stirred at the same time. Subsequently, 10 ml of 50 wt % hydrogen peroxide (H_2O_2) was introduced into the solution. As a final step, solution diluted with 100 ml distilled water to a 0.05 M of molar concentration. For the synthesis of nanowires, 3 ml of the prepared solution was mixed with 0.5 ml of hydrochloric acid (6M), 2.5 ml of distilled water and 10 ml of acetonitrile. FTO coated with WO_3 seed layer was placed inside the autoclave and the prepared solution was introduced into the vessel to carry out the reaction at 180 °C for 6 h [24].

They produced two types of nanoflakes, by adjusting the amounts of water and oxalic acid. To produce first type nanoflakes, they took 3 ml of 0.05 M H_2WO_4 solution and then added to the 12.5 ml of acetonitrile along with the 0.02 g of urea, 0.02 g of oxalic acid, and 0.5 mL of HCl. The reaction was performed at 180 °C for 6 h in a Teflon-lined autoclave. The produced film was calcined at 500 °C for 1 h. For the synthesis of other type nanoflake 3 ml of 0.25 M H_2WO_4 solution (more concentrated), higher amount of oxalic acid (0.2 g), little amount of water (2.5 ml), and the same amounts of HCl (0.5 ml) and acetonitrile (10 ml) were mixed. The reaction was conducted, and film was annealed as same as previous nanoflake growth. Field emission scanning electron microscope (FESEM) images belongs to the nanowire and nanoflakes film of WO_3 are as given in Figure 2.3 [24].

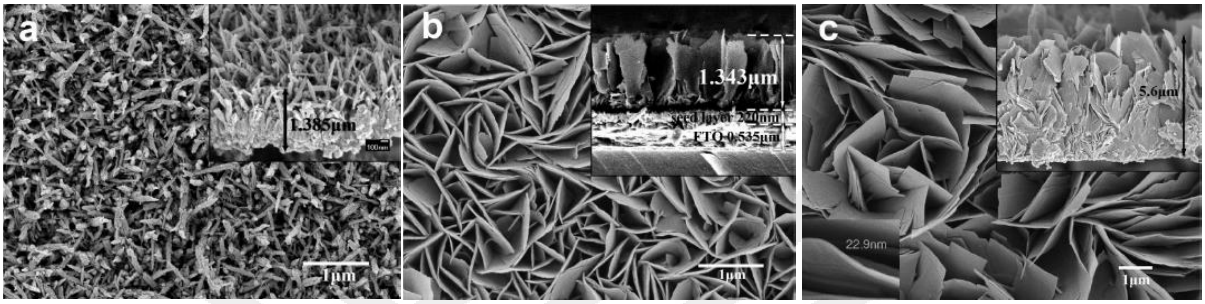

Figure 2.3 FESEM images of as-prepared WO3 films (a) nanowire (b)first type-nanoflake (c)second type-nanoflake [24].

They reported the impacts of the reactant concentrations on geometry of the nanostructures. For example, increasing the amount of oxalic acid up to 0.1 g in the mixture led to a film which consisted of both nanowires and nanoflakes. By increasing oxalic acid amount further to 0.2 g, second type-nanoflake was observed. When the introduced amount of urea was higher than 0.02 gram, the nanowire structure was not observed. Particles and 'sea urchin-like wires' were obtained, when no urea was added in the production of first type-nanoflake films. The crystal structures of the WO_3 films were reported as monoclinic and hexagonal for the nanoflakes and nanowire films, respectively. Band gaps for the nanowire, first type-nanoflake and second type-nanoflake were found as following: 2.92 eV, 2.61 eV and 2.51 eV. The highest photoactivity was recorded from the second type-nanoflake films as 1.43 mA/cm^2 in 0.1 M Na_2SO_4 under AM 1.5 G irradiation [24].

Studies revealed that large amounts of grain boundaries have negative effects on photoelectrochemical performance. Resistance of the grain boundaries reduces the rate of electron transport to the back-contacted substrate and grain boundaries favour the recombination of the charges [28,56]. Amano's group investigated the impact of grain boundaries on photoactivity. For this purpose, they compare two different types of WO_3

films: flake-wall films (vertical arrays) and flake-laminate films (horizontally laminated flakes). Flake wall films were produced from tungsten hexachloride via solvothermal method on FTO substrate covered with WO_3 nanocrystalline film. Flake-laminate films were prepared by using paste-squeegee method. The solution used for the film includes powder obtained from the solvothermal reaction, distilled water, acetylacetone, and surfactant Toriton X-100. Figure 2.4 shows the SEM images of flake-laminate and flake-wall films [28].

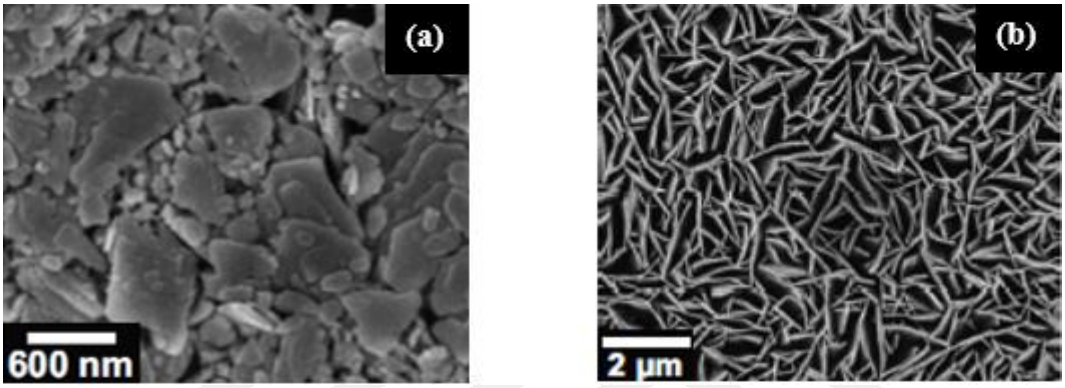

Figure 2.4 SEM image of WO3 films (a) flake-laminate (b) flake-wall films [28].

They reported the photocurrent density of the flake-wall WO_3 film as approximately 2.0 mA/ cm^2 while the flake-laminate WO_3 photoanode photocurrent density was 0.5 mA/ cm^2 from the back-side measurement in a 0.1 M Na_2SO_4 solution. The photocurrent density of a flake-wall WO_3 film was approximately 4.0 mA/cm^2, the flake-laminate WO3 photoanode was 2.5 mA/cm^2 from the back-side measurement in a 0.1 M Na_2SO_4 with 10% vol methanol solution. From front side measurement, current densities were obtained as 2.5 mA/ cm^2 and 0.5 mA/cm^2 from the flake-wall and flake-laminated respectively. Based on their photoelectrochemical measurements, they suggested that flake-laminate films showed less activity since they contained grain boundaries with higher density [28].

After the investigation of effects of large amounts of grain boundaries arising from the crystalline seed layer, vertically oriented WO_3 film growth via hydrothermal synthesis without seed layer has become a promising method to produce working photoanodes with high efficiency. When the seed layer was not used, nonhomogeneous coverage with empty sides was observed in the WO_3 deposition on bare substrate since the adhesion to FTO was weak [9]. Yang and his co-workers developed a hydrothermal method to produce WO_3 arrays in vertical orientation without a seed layer. They prepare solution from the mixture of tungsten dehydrate ($Na_2WO_4.2H_2O$) as a source of tungsten, ammonium oxalate ($(NH_4)_2C_2O_4$) as capping agent, HCl and distilled water. As a different application, they placed FTO substrate inside the autoclave as the conductive side of it remaining below instead of facing up. They claimed that it is better than putting face up since particles could rinsed from the surface easily with water. They investigated structure and morphology of the films produced by hydrothermal reaction at various temperatures (80-180 °C) and at different deposition times (0.5 h - 20 h). After films were cleaned and dried, they were annealed at 450 °C for 1h. Figure 2.5 demonstrates the impact of deposition temperature on film structure [39].

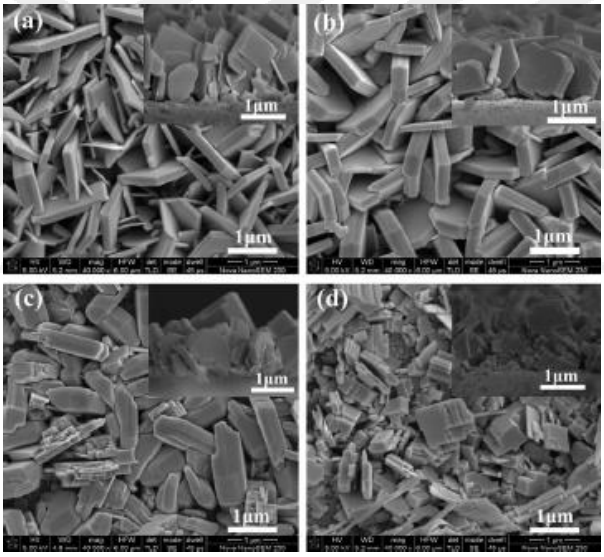

Figure 2.5 SEM images of hydrothermally prepared WO3 films at various temperatures for 12 h (a) 80 °C, (b) 120 °C, (c) 150°C and (d) 180 °C [39].

They suggested that at 80 °C the surface was covered, and at 120 °C plate-like arrays become uniform having a porous structure which provides higher interfacial area between the film and substrate. Structure was transformed into 'irregular block-like' plates at 180 °C. Calcinated films comprised of monoclinic structure. They showed that the morphology of the films led to highly effective on solar to photocurrent efficiency. Photoelectrochemical activities were measured in 0.5 M H_2SO_4 under light irradiation. Figure 2.6 shows the obtained photocurrent densities of these films [39].

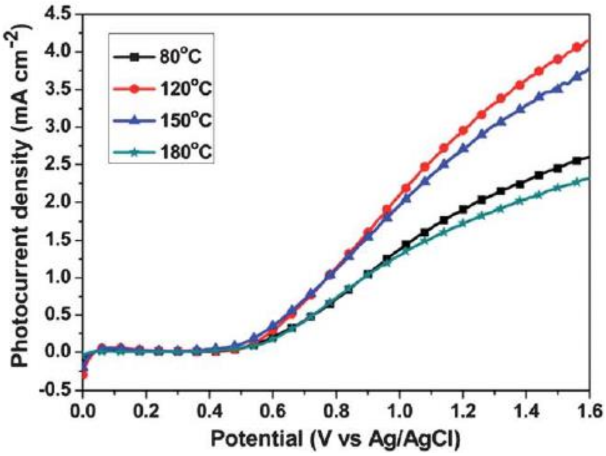

Figure 2.6 Cyclic voltammetry results obtained in light from the films deposited at various temperatures [39].

They suggested the reasons obtaining the best activity from the 120 °C deposited sample are as following:

1- It has higher crystallinity than deposited film at 80 °C (size effect)
2- The film produced at 150 °C has lower surface area and less porous since the platelets were thicker and more adjoining
3- The film coated at 180 C has the lowest surface area which leads to poor transportation of charges

The recorded data at 1.6 V vs. Ag/AgCl were as 2.60, 4.13, 3.80 and 2.32 mA/cm^2 for the films produced at 80,120,150 and 180 °C respectively [39].

They investigated time effect by performing experiments at 120 °C for 15 min, 1 h, 6 h and 20 h. Figure 2.7 shows the effect of deposition period on film morphology. They found that 15 min deposition time was enough to cover FTO surface and morphologies of the films were highly distinguishable.

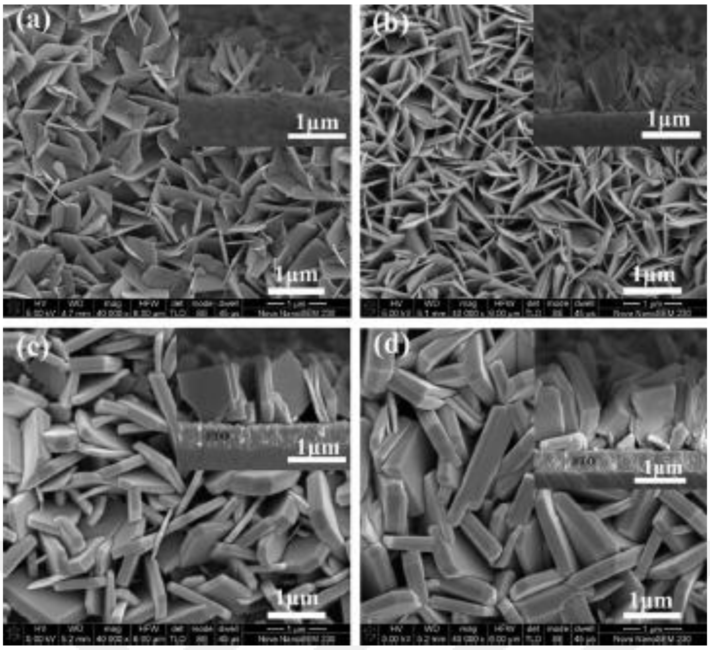

Figure 2.7 SEM images of hydrothermally prepared WO3 films at different deposition periods at 120 °C (a) 15 min, (b) 1 h, (c) 6 h and (d) 20 h [39].

The highest photocurrent activity from the produced WO_3 photoanodes at 120 °C was obtained from the film deposited for 12 h with a current density of 4.12 mA/cm^2 at 1.6 V vs. Ag/AgCl. For the 20 h period it was 3.3 mA/cm^2 while it was 1.81 mA/cm^2 for the 0.5 h one [39] .

Kalanur *et al.* achieved hydrothermal growth of WO_3 nanorods on bare FTO (without using a seed layer). They also discussed the impacts of variables such as reaction time, solution contents and post annealing temperature. They used ammonium paratungstate $\{(NH_4)_{10}(H_2W_{12}O_{42}).4H_2O\}$ as a tungsten source and prepared a solution mixing it with distilled water, certain amounts of HCl and H_2O_2. They also placed FTO as the conductive side facing down in the autoclave. Hydrothermal synthesis was carried out at 120–200 °C for 1–14 h. They reported increasing in the post annealing temperature changed the nanorod structure. For example, at calcination temperature 500 °C, single nanorods were replaced by twin nanorods and further temperature increase (to 600 °C and 700 °C) caused disappearance of the nanorods. They observed nanorods and similar features at all reaction temperatures of 120 °C, 160 °C and 200 °C except the films deposited 120 °C had thicker nanorods due to slower growth [9]. They also showed the effect of the solution pH on film morphology. For this purpose, films were produced at different amounts of HCl. Figure 2.8 shows the top-view

SEM images of WO_3 nanorods synthesized hydrothermally at 160 °C for 4 h with different HCl concentrations [9].

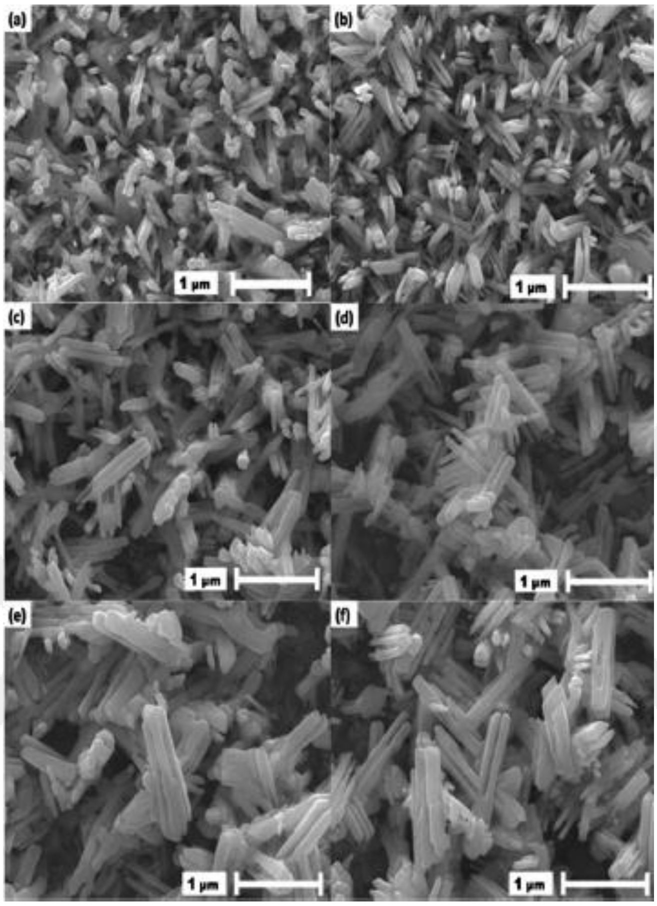

Figure 2.8 SEM images of WO3 nanorods synthesized via hydrothermal method with HCl amounts of (a) 1 ml (b) 3 ml (c) 4 ml (d) 6 ml (e) 8 ml and (f) 10 ml [9].

As seen in Fig. 2.8 nanorods prepared with less amount of HCl have smaller diameters so that using large amount of HCl favours crystal growth more than nucleation. Adding 3 ml of HCl resulted in fine perpendicular nanorods (Fig. 2.8 (b)) while random growth was observed when 4 ml HCl was used. Further increase in the amount leads to low adhesion of the nanorods and formation of larger empty spaces. They reported the best photoactivity from the WO_3 nanorod arrays produced at 160 °C for 4 h with 3 ml of HCl and post calcination at 500 °C for 1 h. It showed a photocurrent of 2.26 mA/cm^2 at 1.23 V vs. RHE in 0.5 M Na_2SO_4 electrolyte [9].

Amano *et al.* also examined the effects of temperature and time of the reaction on photoelectrochemical performance. They produced plate-like WO_3 films from the hydrothermal synthesis of tungsten sheets in nitric acid at 100-180 °C for 0.5-12 h. Produced films were calcined at 450 °C for 3h. Fig. 2.9 shows the morphology of the films taken by SEM produced at different deposition temperature and period [27].

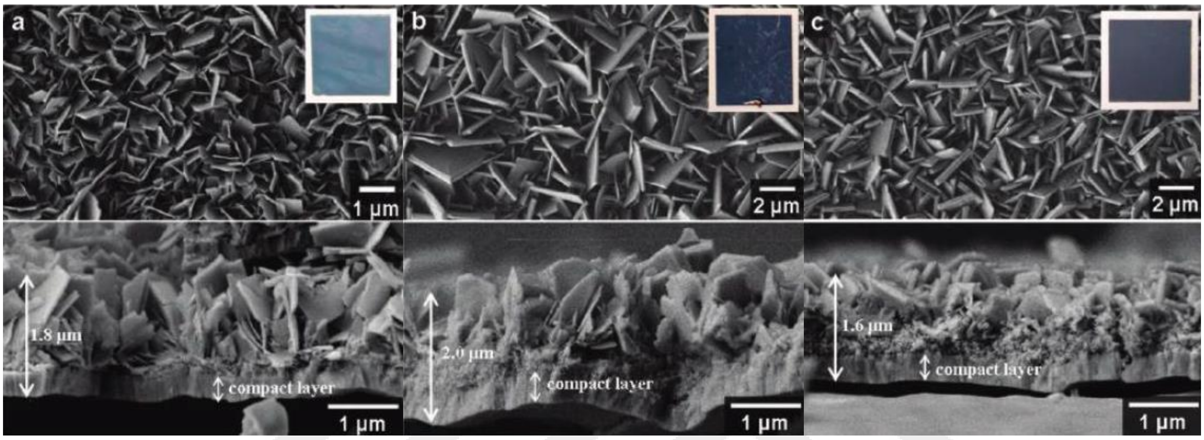

Figure 2.9 SEM images of annealed at 450 °C for 3 h plate-like WO3 films produced at (a) 100 °C for 3 h (b) 140 °C for 2 h and (c) 180 °C for 1 h from the top and side views [27].

As shown in Fig. 2.9, WO_3 film growth is in vertical orientation and morphology of the films were depends on temperature and time. Before calcination, higher lateral dimension and thickness were observed from the film deposited at 140 °C for 2h followed by at 1h 180 °C deposition one. After calcination, reported thicknesses were 1.8, 2.0 and 1.6 μm as seen in Fig.x. (a), Fig.x (b) and Figx(c) respectively. All the films had the monoclinic structures. Band gaps of the annealed films were 2.89, 2.79 and 2.82 eV for deposition at 100 °C for 1 h, proceed at 140 °C for 2 h and coated at 180 °C for 1 h respectively. Photoelectrochemical tests were performed in a 0.1 M H_2SO_4 electrolyte. Figure 2.10 demonstrates the photochemical activity of the film deposited at 180C for various periods (0.5,1,2,3 and 12 h). The highest photocurrent was reported as 4 mA/cm^2 at 1.2 V vs. Ag/AgCl and the on-set potential measured from the film was found as +0.48 V vs. RHE [27] .

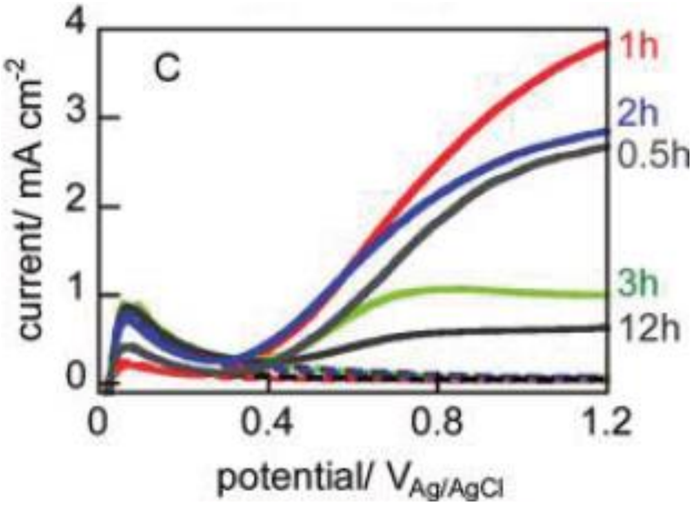

Figure 2.10 CV of the hydrothermally deposited WO3 films at 180 °C for different time periods performed in 0.5 M H2SO4 under dark (dashed lines) and under illumination [27].

2.3 Supercritical Fluid Deposition (SCFD) Method for Thin Film Production

Interest in processes with supercritical fluids has been growing since 1990s as being an alternative way to overcome the limitations of conventional methods [57]. One of the most common methods for production of high purity metallic films is chemical vapor deposition (CVD), but it has disadvantages such as precursors with low vapor pressure which lead to mass transfer limitations and formation of thermomechanical stresses. Solution based techniques mostly have drawbacks such as formation of the excess waste water and insufficient growth control of the films. Films can be deposited at higher rates with full coverage and also with high aspect ratio by SCFD method [49]. Figure 2.11 demonstrates the differences in deposition of the Copper films on etched Si wafer by CVD and SCFD. ScCO2 deposited Cu film shows better coverage as seen in (Fig 2.11 (b)).

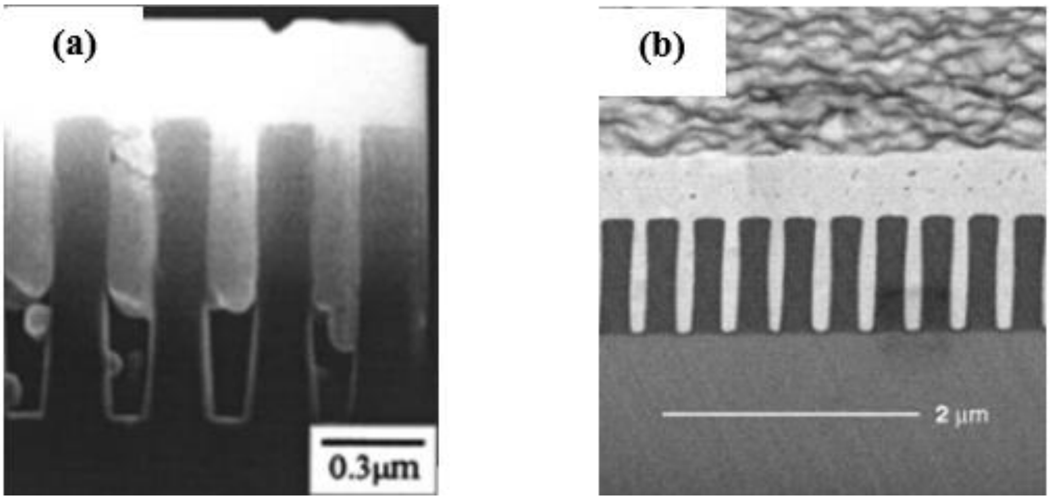

Figure 2.11 Deposition of Cu films for gap-filling (a) CVD [57] (b) ScCO2 deposition [58].

SCFD technique for the metallic film deposition can be summarized in three major steps [48]:

i) Complete dissolution of the precursor
ii) Precursor adsorption on to the substrate
iii) Conversion of precursor to its metallic film

Many studies exist about the solubility of the metallic precursors (inorganic or organometallic) in $scCO_2$. Solubility of more than 780 solutes in $scCO_2$ can be found in the book titled “Solubility in Supercritical Carbon Dioxide which was compiled” by Ram B. Gupta and Jae-Jin Shim [58]. However, there is still unexamined solubilities of the precursors in $scCO_2$. For example, $W(CO)_6$ solubility data does not exist in the literature.

For the film growth, adsorption of the precursor on the substrate plays an important role. In supercritical fluids, adsorption largely depends on the external mass transfer resistance. Thus, concentration of the precursor in the fluid phase effects its adsorption on surface of a substrate [48].

Information about the film formation step of the SCFD is very limited in literature. Zong and Watkins generated a model for the hydrogen assisted copper film formation based on their research on the kinetic and reaction mechanism. They assumed that first, hydrogen and dissolved precursor diffuse to substrate and adsorb on the surface of a substrate. As a second step, surface reaction occurs and resulted in liberation of copper. At last, desorption and diffusion to the supercritical fluid of the hydrogenated ligands takes place by leaving the pure metal layers [40].

2.3.1 Supercritical Fluids

Fluids are called as supercritical when they exceed their critical temperature and critical pressure. Carbon dioxide, ammonia, acetone and water are mostly used in supercritical fluid deposition. Also, it is possible to introduce additional reagent such as H_2, O_2 and H_2O_2 in supercritical deposition technique [57]. Figure 2.12. shows the temperature-pressure phase diagram of the CO_2 [59].

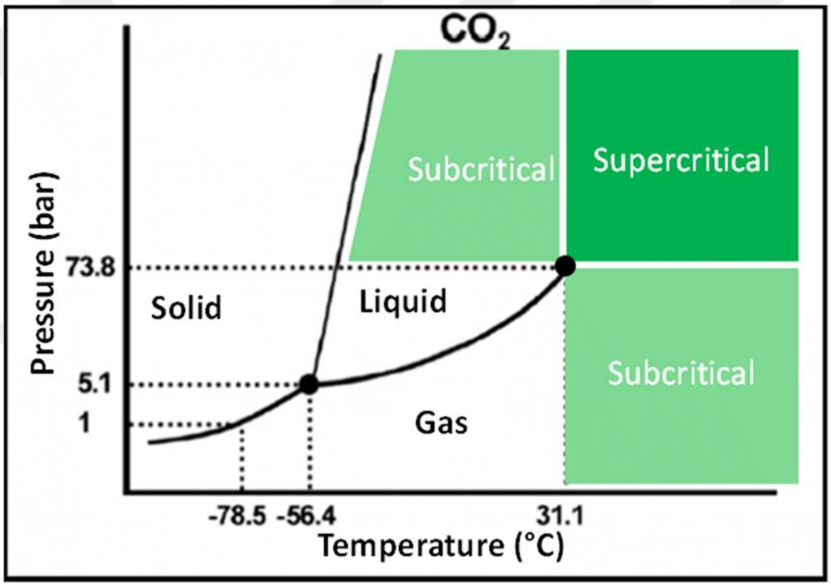

Figure 2.12 T-P diagram of a pure CO_2.

As seen in Figure 2.12 single homogenous phase exist since there are no boundaries in supercritical fluids. A substance can transform from its liquid state to gas state without a phase change if it goes through the supercritical region due to no boundary feature. Supercritical fluids have nonconventional thermophysical properties which is largely depend on its density so that pressure and temperature. They exhibit liquid-like densities and gas-like viscosities[49]. Among the supercritical fluids, CO_2 is the most commonly used one. Its critical pressure (7.39 MPa) and its critical temperature (31 °C) are achievable without difficulty. Also, people prefer CO_2 because it is non-toxic, inexpensive, non-flammable and it leaves no residue on the substrate [48].

2.3.2 Organometallic Compounds as Precursors in SCFD

Organometallic compounds contain a metal-carbon bond. Most of the organometallic complexes can be source for supported nanoparticles synthesis, metal and metal oxide film deposition since they are highly soluble in supercritical fluid [60,61]. $Ni(CO)_4$, $Fe(C_5H_5)_2$ and $HRhCO(PPh_3)_3$[49], dimethyl(1,5-cyclooctadiene)platinum(II) ($Pt(cod)(me)_2$), $Mo(CO)_6$, $NiCp_2$, $CoCp_2$ are some of the organometallic complexes soluble in $scCO_2$.

For the film production from the organometallic precursor via supercritical fluid deposition, study of J. Watkins and T. Hunde can be given as example. They produced cobalt and nickel films on various substrates (Si, TaN/Si and TiN/Si) by using $CoCp_2$ and $NiCp_2$ in $scCO_2$ as a source and by reducing them with H_2 for the film formation [41].

Platinum (Pt) nanoparticle deposition on supports by supercritical method can be done by using $Pt(cod)(me)_2$. For instance, Y. Zhang and C. Erkey have studies with $Pt(cod)me_2$ for the nanoparticle deposition on different supports such as silica (SiO_2), silica aerogel (SA), carbon black, carbon aerogel (CA), aluminium oxide (Al_2O_3) and Nafion [62]. James J. Watkins, Jason M. Blackburn, and Thomas J. McCarthy reported conformal Pt film deposition on Si wafer from $Pt(cod)(me)_2$ via a supercritical fluid technique with the assistance of H_2 [63].

2.3.2.1 Tungsten Hexacarbonyl ($W(CO)_6$)

Tungsten hexacarbonyl ($W(CO)_6$), tungsten hexafluoride (WF_6), tungsten hexachloride, (WCl_6), tungsten ethoxides ($W(OEt)_x$, x = 5, 6) and tetra(allyl)tungsten ($W(\eta^3\text{-}C_3H_5)_4$) are some of the precursors used in CVD method for the deposition of WO_3 film [53,64]. Among these precursors, $W(CO)_6$ is the most studied one [53]. The precursor that is able to dissolve in the supercritical fluid is the appropriate material for the deposition. Although, no data exist about the $W(CO)_6$, we know that $W(CO)_6$ is soluble in $scCO_2$ from the previous studies of our research group.

$W(CO)_6$ has high volatility (1.2 mmHg at 67 °C) [65]. Its toxicity is less than most of the transition metal carbonyls. Tungsten oxides can be obtained easily since it consists of tungsten (0). At 200 °C and above temperatures, $W(CO)_6$ can form films on glass [53].

2.3.3 The Solubility Measurement of the Compounds in SCFs

Two types of techniques have been used to measure the solute solubility in SCFs: static technique and dynamic technique.

Figure 2.13 demonstrates an experimental set-up for the dynamic technique.

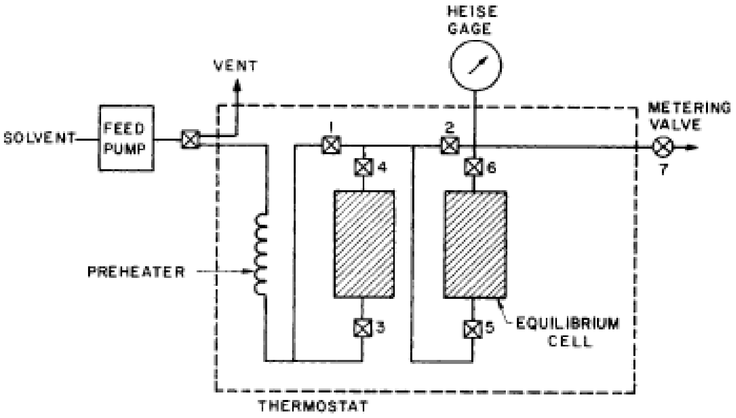

Figure 2.13 The experimental dynamic method set-up of the Van Leer and Paulaitis (1980) to measure solubility in supercritical fluid [67].

In dynamic technique flow is continuous. The vessel is packed and filled with a solute. Packed column is to ensure the enough contact with a fluid. The vessels are placed in a constant temperature bath. First, fluid is pumped and pass through preheater before entering the column to reach the bath temperature. Then, the solute is dissolved in the supercritical fluid as it passes through the vessels. At the exit of a second column, saturated SCF-rich phase is expanded to low pressure (atmospheric pressure) which causes a precipitation of solute. Amount of the obtained solute can be determined by gravimetrical method [66].

In the static method, experiment is conducted in a batch mode. As illustrated in Figure 2.14 the experimental set-up consists of a vessel having a moving piston inside, a view-cell and a camera.

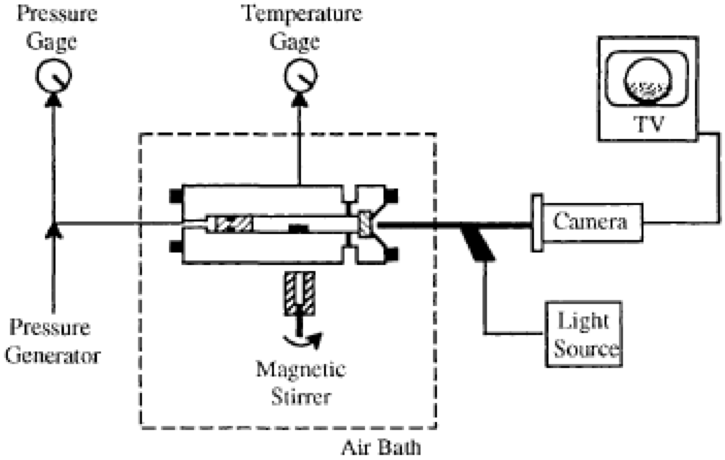

Figure 2.14 The experimental set-up for the static method to measure solubility in supercritical fluid [67].

Precursor is loaded inside a vessel and magnetic stirrer is used to have homogenous medium. The vessel is pressurized until a single phase is obtained. By changing the placement of the piston, pressure is reduced very slowly. Inside of the vessel is monitored via placed camera through the view cell-sapphire window. While decreasing the pressure, solute is separated from the fluid (also called as cloud formation) at a point. At this moment the data is reported. Then solubility can be determined from the known amount of the used precursor and the recorded pressure, volume and temperature [66].

2.3.4 Cold-Wall Reactor Designs for Thin Film Deposition in Supercritical CO_2

Hot-wall and cold-wall reactors are two different reactor models used in the production of films by SCFD. The illustration for the designs is given as in Figure 2.15. Hot-wall reactors are more suitable for preparation of supported nanoparticles since the deposition occur all over the vessel. In such cases, nucleation can occur not only on the substrate but also on the surface of the vessel walls. To overcome this problem, cold-wall reactors were developed. In a cold-wall reactor, only a selective part is heated (e.g. a stage) via electrically or via halogen lamp. In this way, rest of the vessel remains cold or colder. By placing substrate onto this selectively heated part, it is ensured that the film deposition proceeds only on the substrate while the walls of the vessel remains uncoated.

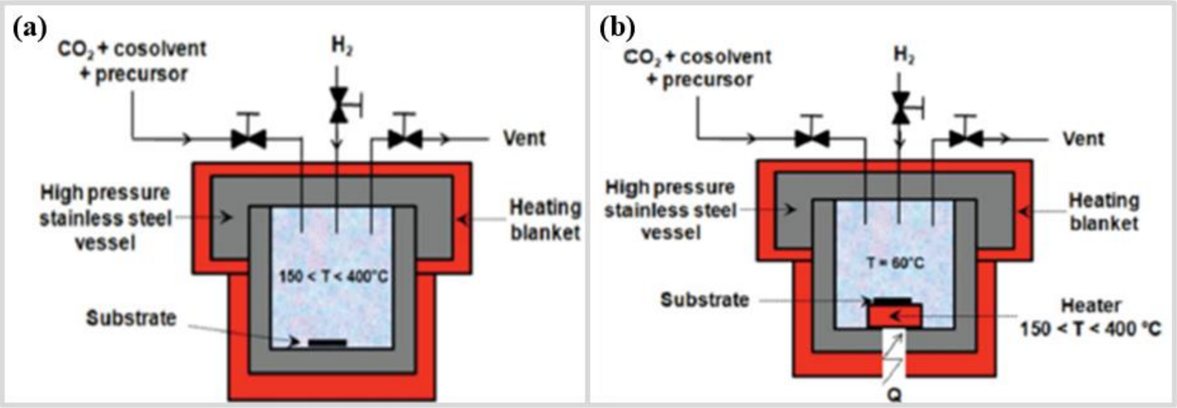

Figure 2.15 Schematic designs of SFCD high pressure vessels (a) hot-wall and (b) cold-wall.

Prior to design a cold-wall reactor, one must consider the style of the heated stage, types of the heating sources, mounting of the substrate on a stage, sealing, and possible natural convection of SCF. Couple of studies exist in literature about the design of the cold-wall reactor in detail. Q. Peng and co-workers reported deposition of metal oxide films by pyrolysis of metal diketonates in a reactor with heating stage although the reactor is not specified as cold-wall reactor. The schematic diagram of their constructed experimental set-up having a 110 ml high pressure cold-wall reactor is given as in Figure 2.16.

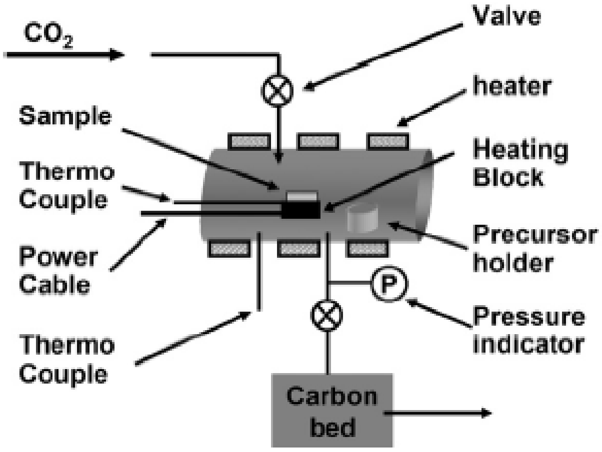

Figure 2.16 Experimental set up of the metal oxide deposition in scCO2 with cold-wall reactor (belongs to study of Q. Peng, D. Hojo, K. J. Park, G. N. Parsons) [68].

Heating of the stage was carried out by three cartridge heaters (Tempco) which were placed inside the stage. A thermocouple to control the stage temperature was fixed to the stage. Fitting of the thermocouple and the stage were fixed up with a gland fitting (Conax Buffalo Corp.). The experiments were performed in a batch mode by putting the stage heater and precursor prior to seal [67].

Another design was given in detail by Karanikas in his doctoral dissertation. A reactor with a volume of 70 ml was constructed from 2 stainless steel flanges. Heating stage consisted of a coil resistive heater (450W, Belilove Company Engineers). Representative construction of the heating stage is given as Figure 2.17. In our point of view, dark grey twist represents the coil of the resistive heater (Fig. 2.17). The stage was fitted by a split gland fitting (Conax Buffalo Corp.). Thermocouples were introduced to the stage and the vessel wall with a controller to set desired temperature. Heating of the vessel walls was done by using cartridge heaters [68].

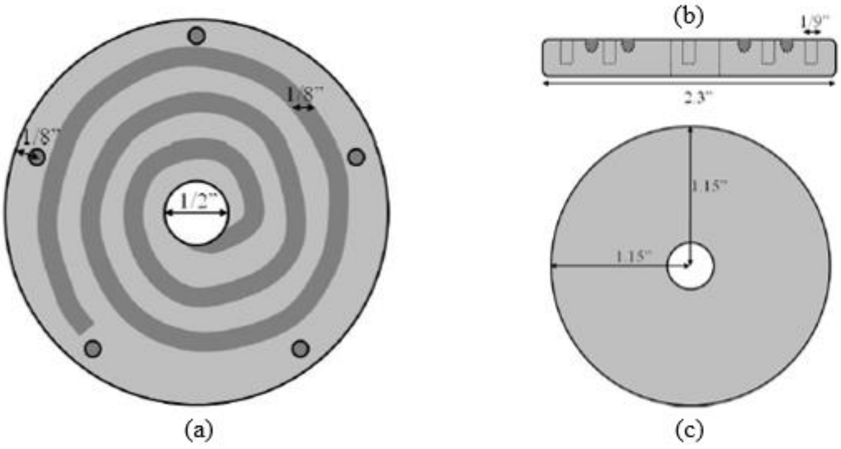

Figure 2.17 The bottom component of the heating pedestal (a) top view (b) side view (c)bottom view [68].

Zhao and co-workers designed the cold-wall reactor with a different idea. They desired to reduce natural convection of scCO2 by mounting the heating stage facedown as shown in Figure 2.18 Ceramic heater was used as a stage inside the 15 ml stainless-steel chamber reactor. The substrate was fixed to the back side of the heater which is standing facedown [47].

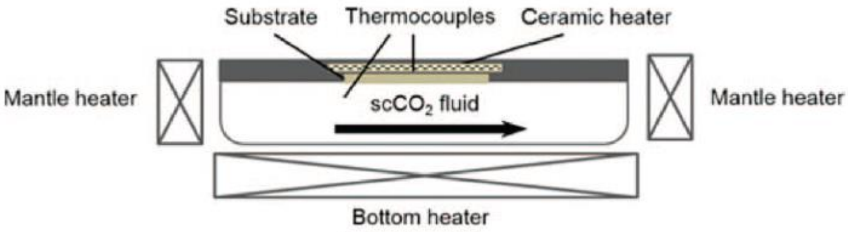

Figure 2.18 Schematic illustration of the facedown cold-wall reactor [47].

In a cold wall reactor, natural convection is occurred due to the density inequality of the supercritical fluid due to the temperature difference between the heating stage where the temperature is higher and the reactor wall. Watkins' group also studied fluid dynamics of the cold wall reactor to understand the effect of the natural convection. They performed simulations by CFD Fluent program for two different cold-wall reactors similar to each other. A cold-wall reactor schematic diagram is given in Figure 2.19.

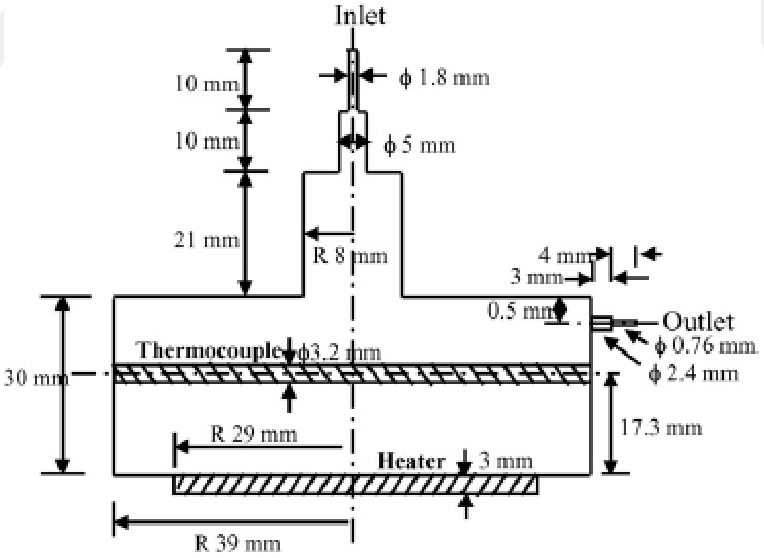

Figure 2.19 Cold-wall reactor set-up from the cross-section.

A thermocouple was inserted into a thermowell from the side wall and moved to the middle of the vessel to measure the temperature from different locations along the length of the reactor. They examined the temperature differences 0.2 and 0.4 mm above the stage for two different cold-wall reactors. First one had higher clearance than the second one (51 mm and

12.7 mm). The initial temperature of the stage was 400 K and then it was set to 498 K. Temperature distributions were shown as Figures 2.20 and 2.21 for the vessel with high clearance and for the vessel with low clearance, respectively. They observed that in the reactor having a larger clearance, temperature gradient is highly uniform unlike the other reactor. Changes in the temperature gradient is not the desired condition for the conformal film deposition. Hence, they reported the cold-wall vessel with low clearance is not suitable design for thin film deposition [69].

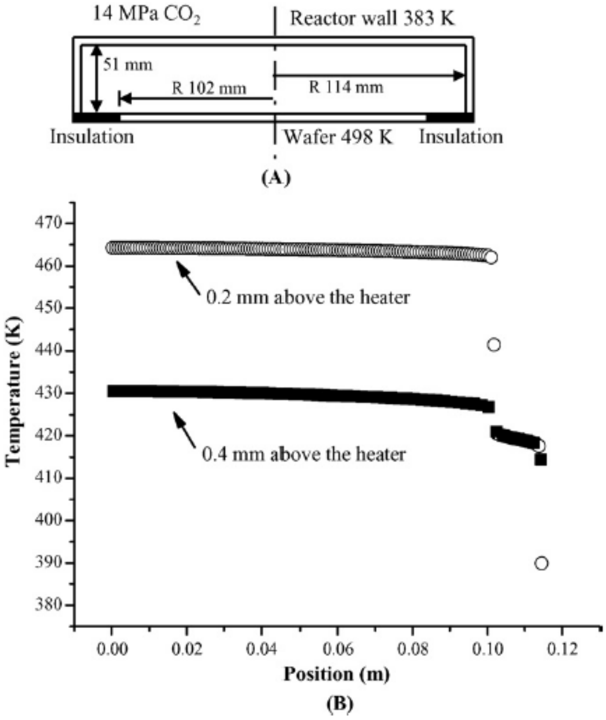

Figure 2.20 Simulation result for a reactor with high clearance (51 mm) (A) Schematic diagram of the dimensions and boundaries (B) Temperature distributions of 0.2 mm and 0.4 mm above the heating stage from centre (x=0) to wall [69].

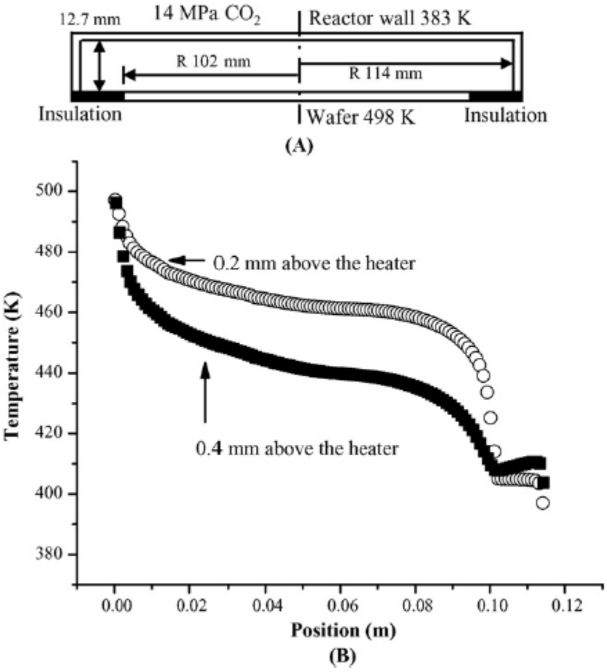

Figure 2.21 Simulation result performed in a reactor with low clearance (12.7mm) (A) Schematic diagram of the dimensions and boundaries (B) Temperature distributions of 0.2 mm and 0.4 mm above the heating stage from centre (x=0) to wall [69].

They also simulated the temperature difference between the surface of the heater and the $scCO_2$ in the region. Simulation was performed in a batch mode with CO_2 at 18.5MPa and stage temperature at 498K. Wall temperature was measured as 393 K which indicates the 100 K difference between the heater and the wall temperature. They reported that it is the common condition during film deposition to prevent the coating on wall. Figure 2.22 shows the temperature change with the distance from the heating pedestal [69].

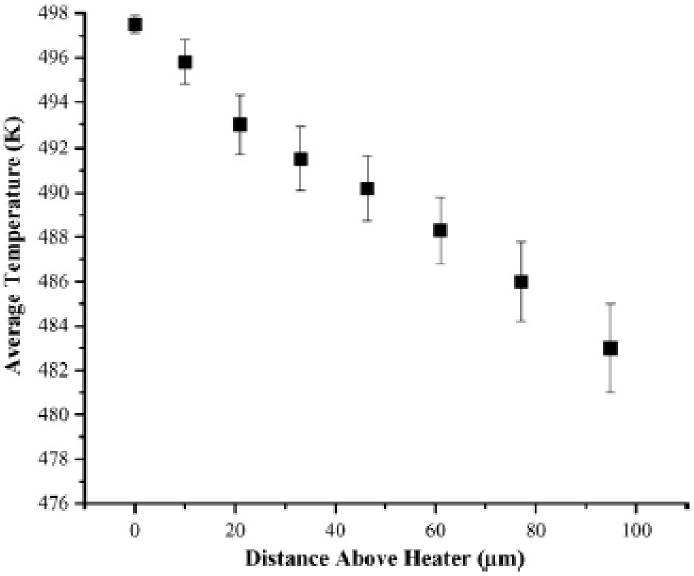

Figure 2.22 Temperature change with the distance above the heated stage at 18.5MPa with substrate temperature at 498 K and wall temperature at 393 K [69].

2.3.5 Thin Films Prepared in Cold-wall Reactor

In supercritical fluid deposition technique, the cold-wall reactors are more suitable for the thin film production. Although most studies have been on metallic films, there were also a few reported studies on metal oxide films. WO_3 film coating via supercritical fluid method has not been studied but understanding the experimental procedure of the produced films is important to develop a new technique.

Y. Zong and J. J. Watkins studied the reaction mechanism and kinetics of a Cu film deposition on TiN-coated Si with the assistance of H_2 in a cold wall reactor. They conducted the experiments in batch mode. First, the substrate (12 mm x 12 mm TiN/Si) was fixed on the heating stage and precursor bis(2,2,7-trimethyloctane-3,5-dionato) copper (II), [Cu(tmod)$_2$] was loaded before sealing the reactor. Then, reactor was purged with CO_2 and heated to desired temperature (60 °C). CO_2 was introduced to the vessel at various pressures (100-138 bar). After waiting for the dissolution of the precursor, H_2 was loaded to the vessel at different amounts. Deposition was started by turning the heating stage. Desired stage temperature (220-270 °C) was obtained in 40 s. Coating of the copper film took 5 min.

When the stage was turned off and the stage temperature decreased to 200 °C in 10 s, reaction stopped. The growth rate was reported between 5 to 35 nm/min within the temperature range of 220 to 270 °C[40].

Cabañas et al. deposited gold (Au) films on different substrates such as metal, ceramic, and polymeric with seeding Ni, Pd, or Pt clusters via H_2 assisted supercritical fluid deposition in a cold-wall high pressure reactor. They performed experiments in a batch mode with a low deposition temperature of 125 °C. Steps that they followed are same as H_2 assisted Cu film deposition except the deposition time. The deposition was carried out 3-4 h. Thickness of the deposited films varied between 90 to 400 nm for 4h deposition time depending on the substrate type and precursor loading. Examples of Au films are illustrated in Figure 2.23 (a) on a bare Si at 125 °C and 150 bar and (b) on etched Si wafer with 0.08 wt% loading 125 °C and 150 bar [43].

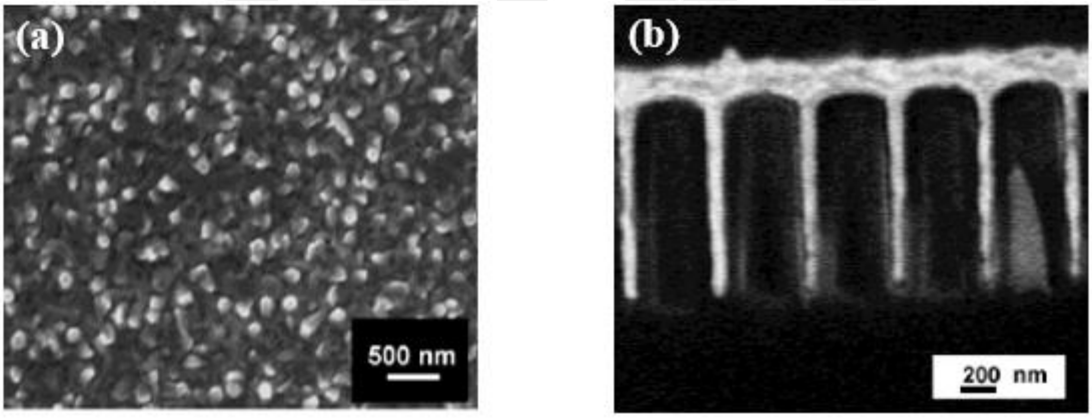

Figure 2.23 Au film coated on Si and etched Si wafer at 150 bar and 125 °C in cold-wall reactor [43].

Hunde and Watkins reported fine cobalt and nickel film growth on bare SiO_2 and TaN or TiN coated SiO_2 in supercritical CO_2 with the assistance of reducing agent, H_2 using cold-wall reactor. The experiments were performed in batch mode, so that substrates were mounted on a stage and precursors (~0.2-0.5 wt%) were placed into the reactor as a first step. CO_2 was introduced (at 220-260 bar for Co deposition and 190-230 bar for Ni deposition) inside the vessel after the reactor was heated to 70 °C. Different from previous methods, H_2 was loaded after the stage was heated to specified temperature (285-320 °C for Co deposition and 175-

200 °C for Ni deposition). While pedestal heating was running, the heating of the walls was stopped. Due to the unique nature of the cold-wall reactor, the wall temperatures of the reactor remained in a range of 90 to 120 °C and the film growth occurred only on the substrate. Deposition times were typically 30-45 min. They observed that even a little increase in temperature leads much higher growth of the Co films. For instance, the thickness was 150 nm at 285 °C whereas it was 680 nm at 300 °C at 0.23 wt. % precursor loading and 80:1 hydrogen to precursor ratio [41].

O'Neil and Watkins studied ruthenium film growth process with H_2 assisted supercritical deposition in a cold-wall reactor. Film deposition were performed at different pressures (20-25 MPa) with substrate temperatures of 175 to 300 °C on SiO_2 and tantalum coated Si wafer. The experimental procedure was the same as the Cu film deposition. They reported that heating rate of the pedestal changed with the set temperature of the stage. For example, it took 150 °C in 2 min whereas 300 °C was reached in 3.5 min. Films were deposited for 30 min and even shorter time range at high temperatures. Film thickness were varied from 7 nm to 110 nm depending on the type of the precursor and substrate, precursor loading, substrate temperature, hydrogen amount and deposition time. They also indicated that obtained film thickness did not give enough information to attain reaction kinetics. For instance, at the same temperature, reported thickness for the 5 min. deposited film is almost half of the 30 min. deposited one. Hence, it was more likely the deposition was completed earlier than 30 min [70].

O'Neil and Watkins also reported metal oxide film on Si and etched Si deposition in supercritical CO_2 using cold-wall reactor. Typically, substrate temperature was varied between 250 and 300 °C for the deposition of cerium (CeO_2), hafnium (HfO_2), titanium (TiO_2), niobium (Nb_2O_5), tantalum (Ta_2O_5), zirconium (ZrO_2), and bismuth oxides (Bi_2O_3). Few amounts of H_2O were introduced for some depositions as oxidizing agent. They obtained films having a thickness in the range of 21 nm to 263 nm. The batch mode experiments were conducted in 80 ml cold-wall high pressure vessel. First, substrates were fixed to the stage and known amounts of precursors (0.14-2.8 wt. %) were loaded. In the use of precursors of Ce, Hf, Zr and Bi, the vessel was purged with N_2 at 150 °C otherwise it was 60 °C. After pressurizing the vessel with CO_2 (11-20 MPa) or dried CO_2, it was waited to dissolve the material for 1 hour. In the experiments conducted with H_2O, certain amount of water (2, 5, 10, or 15 µl) was introduced to the flow of the CO_2. Film growth took 30 min.

Annealing films at 400 °C for 1 h was enough to remove carbon, but to get rid of mixed oxide state of the films, calcination was performed at 800 °C for 1 h (to obtain TiO_2 and Bi_2O_3) or 6h (for other metal oxide films). They examined the effect of moisture content of the CO_2. For instance, when dried CO_2 was introduced, film thickness of the CeO_2 was reported as 21 nm while the film that was deposited with the as delivered CO_2 was 58 nm. They also reported the impact of the addition of water to dry CO_2 on film thickness. In the deposition of CeO_2, adding 2 µl water (concentration of 0.11 mmol in CO_2) yields 216 nm thick film and introducing 5 µl water (concentration of 0.275 mmol in CO_2) resulted in a 247 nm film thickness. Further addition of water causes reduction in the film thickness. Successfully deposited films are shown in Figure 2.24 [45].

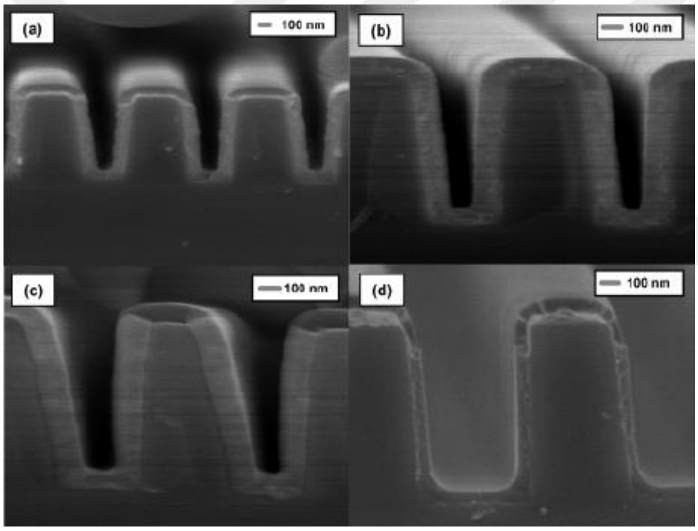

Figure 2.24 SEM images of the metal oxides films on etched Si wafer (a) HfO_2 (b) CeO_2 (c) ZrO_2 (d) TiO_2 [45].

Zhao and co-workers revealed a study of metal oxide film coatings in a cold-wall reactor via continuous flow supercritical fluid deposition. They examined deposition of titanium oxide (TiO_2), bismuth oxide (Bi_2O_3), bismuth titanate (BIT, $Bi_4Ti_3O_{12}$) films on SiO_2 coated Si wafers at various stage temperatures (250-350°C). Titanium di(i-propoxide)bis(2,2,6,6-tetramethyl-3,5-heptanedionato) ($Ti(O\text{-}i\text{-}Pr)_2(tmhd)_2$) and triphenylbismuth ($Bi(ph)_3$) were Ti source and Bi source respectively. Unlike the previous deposition method, they used different hot wall reactors to dissolve precursors. The illustration of the experimental set-up is given as in Figure 2.25 [44].

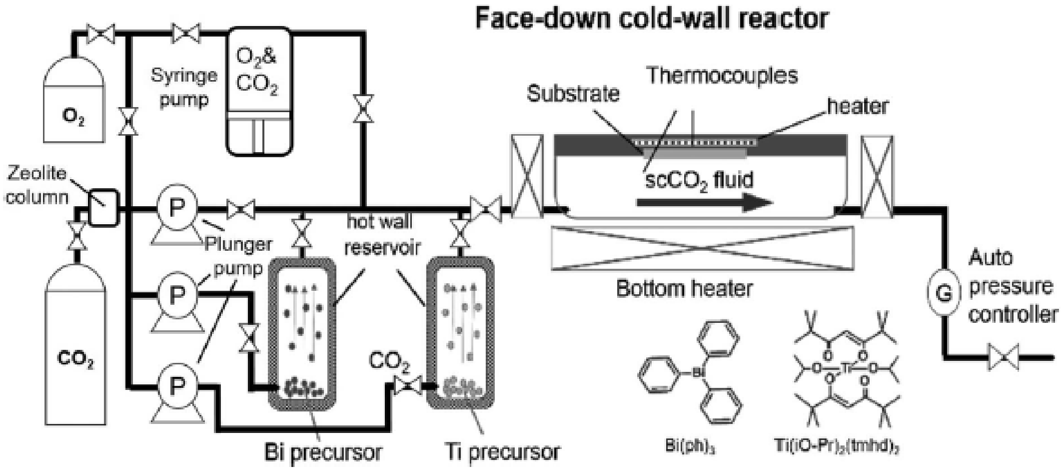

Figure 2.25 Diagram of the continuous flow supercritical deposition experimental set-up for the deposition of bismuth titanate film [44].

First, excess amounts of precursors were loaded to the hot-wall vessels. Then, all the reactors were heated to 50°C and filled with CO_2 at 10MPa. Dissolved precursors in a $scCO_2$ was diluted with different CO_2 flow before sending to the cold-wall reactor. Pedestal heater in the cold-wall vessel was heated to desired temperature [44]. They observed particle generation inside the fluid when the flow rate was higher than 150 ml/min and residence time less than 10 s [47].

For the film growth of Bi_2O_3, Bi precursor was dissolved in $scCO_2$ in the presence of oxygen (0.05 mol/L) since Bi precursor does not contain any oxygen. However, this procedure was not applied in the deposition of BIT, because Ti and Bi precursors were delivered together to the cold-wall reactor and Ti precursor contains oxygen. Ti:Bi ratio was controlled by adjusting the flow rates from the corresponding hot wall reactors. They reported that the suitable deposition temperature was 300 °C for TiO_2 and Bi_2O_3 films. Hence, they conducted BIT deposition at 300 °C by trying different Ti:Bi ratios to find the optimum value. Figure 2.26 shows the BIT coatings with different Ti:Bi ratios and TiO_2 film coating [44].

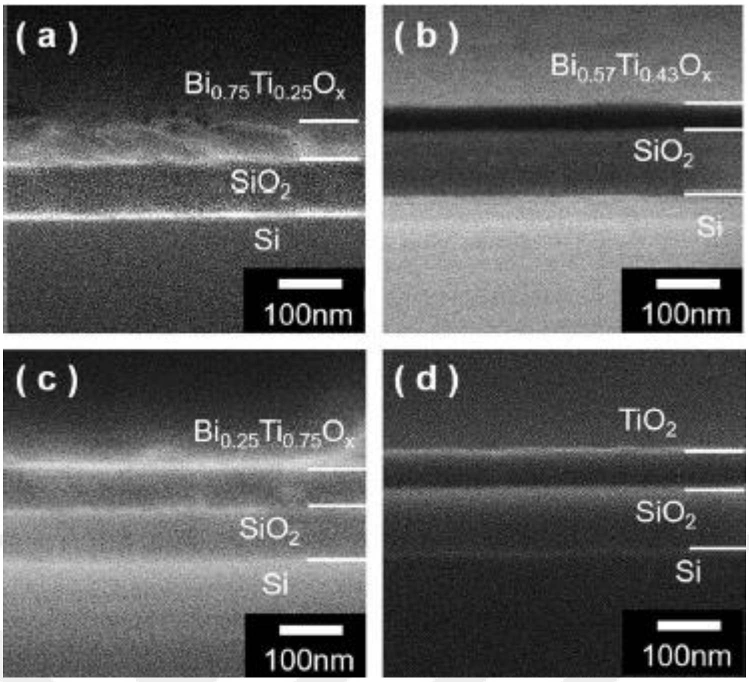

Figure 2.26 SEM images of deposited bismuth titanate with different compositions films and titanium oxide film in cross-sectional view (a) $Bi_{0.75}Ti_{0.25}O_x$, (b) $Bi_{0.57}Ti_{0.43}O_x$, (c) $Bi_{0.25}Ti_{0.75}O_x$ and (d) TiO_2 [44].

Chapter 3

EXPERIMENTAL METHODS AND CHARACTERIZATION TECHNIQUES

3.1 Materials

Ammonium metatungstate hydrate (99.99% trace metals basis), tungsten hexacarbonyl (99.99% trace metals basis (excluding Mo), purified by sublimation), hydrochloric acid (37%), sulfuric acid (95-98%), and methanol (≥99.0%) were purchased from Sigma-Aldrich. Ethylene glycol (≥ 99.0 %) was purchased from Merck. Distillation and deionization of water was done. Carbon dioxide (99.998 %) and oxygen (99.99%) were purchased from Air Liquide. We used the chemicals as they purchased.

3.2 Hydrothermal Synthesis of WO_3 film

Method of WO_3 hydrothermal synthesis was modified from the Székely et al. (2016) recipe [71]. The solution prepared by dissolving 0.77 gram of ammonium metatungstate ($(NH_4)6H_2W_{12}O_{40} \cdot xH_2O$) salt in 12.5 mL of distilled water and 0.53 mL HCl. Hydrothermal reaction was carried out in 80 ml stainless steel autoclave lined with Teflon. This recipe was used for both direct growth on FTO (see section 3.2.1) and synthesis of WO_3 powder (see section 3.2.2).

3.2.1 Direct growth of WO_3 Film on FTO

Two pieces of FTO glasses (1cm x 2 cm area) were ultrasonically cleaned inacetone, ethanol, and distilled water solutions for 15 min and then dried by nitrogen flow.

After that, FTO glasses were placed inside the autoclave with the conducting side facing up. Prepared ammonium metatungstate salt solution was slowly added and the vessel was sealed. The thermal treatment was performed at 180 °C for various times (1 h-10 h). After the reaction completed, vessel was taken out from the oven and let it cool down at room temperature to cool it down. Substrates were taken and left for drying for 1 day.

3.2.2 WO_3 Film Preparation from Hydrothermally Synthesized Powder

WO_3 films obtained from colloidal solutions of WO_3 powder with ethylene glycol on bare FTO substrate (1cm x 2 cm area). For this purpose, WO_3 powder was synthesized in the same autoclave from the ammonium metatungstate salt solution. Reaction was carried out in the oven at 180 °C for 6 h and after completion, the reactor was left to cool down. To get the powder, the solution was centrifuged at 1600 rpm for 15 min. Then it was washed with distilled water and centrifuged at 1600 rpm 15 min. one more time. Collected powder was dried out at 70 °C for 19 h and finally white WO_3 powder obtained. Particle suspension solution was obtained from the mixture of 0.02 gram as prepared WO_3 powder and 0.2 ml ethylene glycol. Solution was sonicated for 30 min and coating was done via drop casting on the surface of FTO. Samples dried at 100 °C for 4.5 h. Post calcination was performed at 500 °C 1 h.

3.3 Solubility Experiments of Tungsten Hexacarbonyl ($W(CO)_6$)

Since no data were available for the solubility of the $W(CO)_6$, to make sure complete dissolution of the precursor in supercritical CO_2, solubility experiments conducted in different high-pressure stainless steel 54 ml custom designed vessel. The vessel has two sapphire windows with diameter of 3.2 cm (Sapphire Engineering, Inc., Pocasset; MA.) which allows us to see inside. First, two different solubility experiments were performed in order to measure the solubility of the $W(CO)_6$ in supercritical CO_2. Known amount of

$W(CO)_6$ (0.5 and 1 gram) and a magnetic stirrer were placed inside the hot-wall reactor and the reactor was sealed with two polyetheretherketone O-rings.

The vessel was heated to selected temperature (35 °C and 45 °C) with circulating heater/cooler (Cole Parmer, Model 12108-15). CO_2 was loaded inside the vessel using a syringe pump (ISCO, 260D). Magnetic stirrer was turned on for the fast and homogenous mixing. The pressure was increased so slowly and then we wait for equilibration and dissolution of the precursor. If all the precursor did not dissolve, more CO_2 was added and was waited for a long time to observe dissolution. While CO_2 were adding, inside of the vessel was monitored in case of the complete dissolution of precursor during the pressure increase. The pressure was recorded when the complete dissolution of the $W(CO)_6$ was observed. By knowing the temperature and the pressure of the $scCO_2$, density of it was found from the NIST Thermophysical Properties database. Then, the solubility (mol/mol) was determined from the set of equations (Eqn. 3.3.1-3.3.3) which are as follow:

$$n_{CO_2} = \frac{\rho_{CO_2} \times V_{vessel}}{Mw_{CO_2}} \qquad (3.1)$$

$$n_{W(CO)_6} = \frac{m_{W(CO)_6}}{Mw_{W(CO)_6}} \qquad (3.2)$$

$$y\ (mol/mol) = \frac{n_{W(CO)_6}}{n_{W(CO)_6} + n_{CO_2}} \qquad (3.3)$$

where; n and Mw represent the number of moles and molecular weight of the species. Vvessel is the volume of the hot-wall reactor. y stands for the solubility of $W(CO)_6$ in molar ratio.

Secondly, alternative experiments were performed to check the solubility of the $W(CO)_6$ at film deposition conditions. For this purpose, certain amount of $W(CO)_6$ (~0.4% weight) was placed inside the same hot-wall reactor. Desired temperature (80 °C and 135 °C) was achieved by using circulating heater/cooler. Controlling of the vessel temperature was done with assembled T-type thermocouple. After reaching the chosen temperature, the vessel was pressurized with CO_2 to 1200 psi using a syringe pump. The inside of the reactor was monitored to measure the time needed to solve all the tungsten precursor.

3.4 Film Deposition Procedure in The Cold-wall Reactor

In this study, a method was developed to synthesize WO_3 film on conductive FTO glass. Experiments were conducted in a custom-designed 100 ml stainless steel high pressure cold-wall reactor (Erdes Teknoloji Kimya) as given in Figure 3.1. The vessel is equipped with custom-made heating stage (Erdes Teknoloji Kimya) (the blue part in Fig. 3.1), J-type thermocouple (Omega Engineering), pressure transducer (Omega Engineering), and sealing enabled with two polyetheretherketone O-rings. J-type thermocouple is placed ~15 cm above the heating stage and centered between the reactor walls. Heating of the pedestal is done with inserted ~100W resistive heater (BERU). Stage temperature is adjusted with the controller (DELTA, D4848) which was coupled with K-type thermocouple. To arrange the vessel temperature, channels were constructed around the vessel as a reactor jacket.

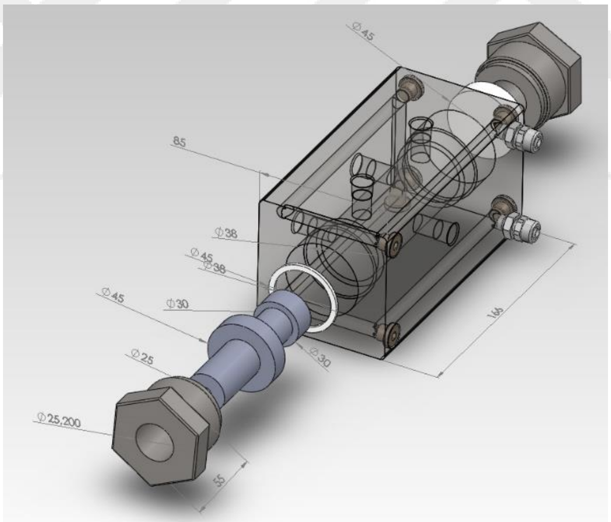

Figure 3.1 Design of the custom-made cold-wall reactor.

Four different deposition methods were tried in a cold-wall reactor. All experiments were conducted in a batch mode. The surrounding of the stage heater was covered with ceramic fiber paper and strapped with PTFE tape for the insulation. Prior to the sealing of the vessel, a substrate with 1 cm x 2 cm FTO glass was fixed on a heating pedestal with PTFE tape and specified amount of $W(CO)_6$ (~0.4% wt.) was introduced into the cold-wall reactor. These steps were the same for all experimental procedures. Temperatures of the vessel and heating stage were the same in every method. Also, the amount of the precursor and CO_2 were identical for each experiment. The stage reached to the desired temperature ~60-70 min and cooled below to 200 °C in 4 min. in every technique.

In the first deposition method, WO_3 was coated in the presence of air that was already in the vessel naturally at 1 atm. Thus, the air was used as an oxygen source. First the vessel walls were heated to the desired temperature (80 °C) by introducing hot water to the channels of the vessel via circulating heater/cooler (Cole Parmer, Model 12108-15). To pressurize the vessel, CO_2 (8.27 MPa) was introduced using a syringe pump (ISCO, 260D). Typically, dissolution of the precursor was conducted within the natural supercritical CO_2 (T=80 °C, P=8.27 MPa) region for 3 h as determined in previous experiment. After that, circulator was closed, and heating stage was turned on for the deposition of a film on a selective area. Deposition temperature was chosen as 300 °C. The stage temperature was kept at same temperature for a certain of time (3 h). To end the experiment, stage was turned off and then the vessel was depressurized slowly by venting the effluent into the distilled water.

In the second procedure, unlike the first method, O_2 was introduced to the vessel (2 bar) after sealing the vessel and then the vessel was heated to the 80 °C by using circulating heater. The rest of the steps were followed as in the first procedure.

Oxygen injection method was used in the third technique. In this application, after filling the precursor and sealing the vessel, circulator heater was started. Heating stage was turned on after waiting the complete dissolution of the precursor in $scCO_2$ (T=80 °C, P=8.27 MPa). The deposition was conducted for 1 h before adding the oxygen. To inject oxygen to the cold-wall reactor, a small high-pressure vessel (30 ml) was used (see Fig. x). Small vessel at room temperature was filled with O_2 (8 bar) and then pressurized with CO_2 (16.55 MPa). After waiting 1 h for the deposition, O_2 injection was performed by opening the valve between the small vessel and cold-wall reactor for a few minutes. When the pressure become equilibration, the valve was closed. The deposition was carried out for 3 more hours in the presence of oxygen. In total, the stage was run for 4 h. To end the experiment, stage was closed, and vessel was depressurized.

In the last method, we used WO_3 coated FTO as a seed layer. Film deposition and seed layer deposition was performed by following the same procedure: the fourth method. The last procedure was very similar to the third method. We applied O_2 injection in this method, but unlike the third procedure, O_2 was introduced without waiting the 1 h deposition. In other words, O_2 was injected when the stage temperature reached to the desired value (300 °C). The reaction was carried out for 4 h. The obtained film was calcined at 500 °C for 1 h and then used as a seed layer for the WO_3 film deposition. WO_3 film deposition was conducted by following the last procedure, but in this time the substrate was the WO_3 coated FTO via supercritical deposition. In short, one can say that the experiment was conducted as if it was two cycles of the film deposition.

Figure 3.2 demonstrates the experimental setup for the supercritical CO2 deposition. Films were annealed at 500 °C for 1 h to get rid of carbon contaminant and oxidize as-prepared films to tungsten (VI) oxide.

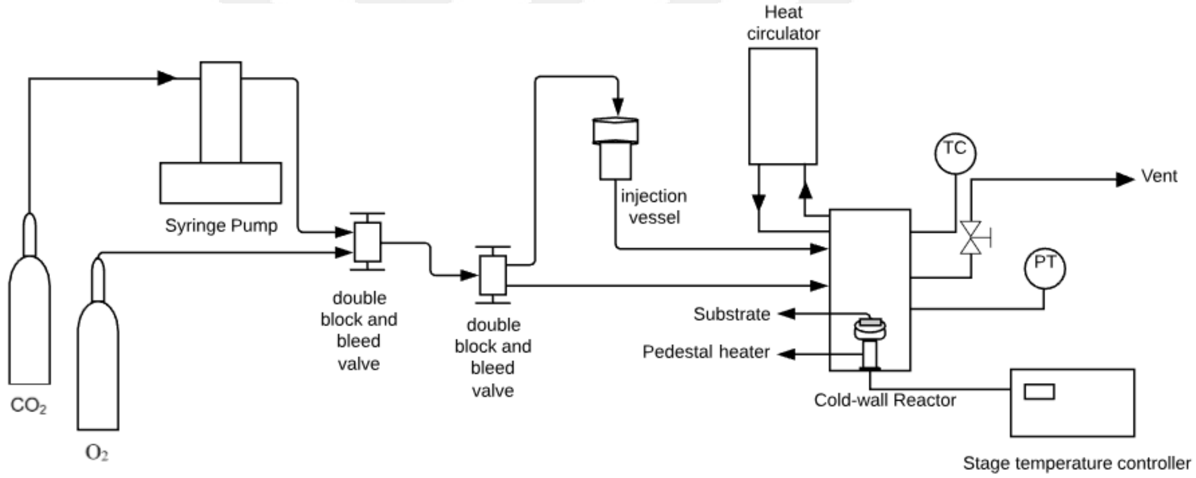

Figure 3.2 Experimental set-up of supercritical CO_2 deposition with cold-wall reactor.

3.5 Material Characterization

Uv-visible absorption and reflection data were recorded for synthesized WO_3 samples with UV-VIS-NIR Spectrophotometer (UV-3600, Shimadzu). X-ray diffraction patterns were verified by Bruker D8 Advance Diffractometer to determine the crystal structure of the WO_3 samples. GiXRD was examined in Cu Kα radiation between 10°-60° 2θ degree with a grazing angle of 1°. Raman spectra were attained using Renishaw inVia Raman Microscope with an

Argon laser (532 nm). SEM images were obtained Zeiss Ultra Plus Field Emission Scanning Electron Microscope with an accelerating voltage of 3-5 kV. EDX data were also obtained from the same SEM equipment with Xflash 5010 EDX detector.

3.5.1 Crystalline Size Determination

XRD spectra data was used to estimate the size of the crystalline particle. For this purpose, Scherrer equation was used which is as follows [72]:

$$B(2\theta) = \frac{K\lambda}{L\cos(\theta)} \qquad (3.4)$$

B(2θ) represents the breadth of the peak measured at half its maximum intensity, which is determined from the data processing program Origin in radians. λ is the wavelength of the X-ray which is 1.5406 Å for the Cu-Kα irradiation. θ is the Bragg's angle which corresponds to the sharpest peak used to calculate particle size. K is the shape factor which is usually taken as 0.9 for the Gaussian fit [73]. Lastly, L represents the size of the particle.

3.5.2 Bang-Gap Determination

Band gap of the semiconductor can be estimated from the diffusive reflectance data. Absorption coefficient relation with the Eg is given as below:

$$\alpha = \frac{A(h\nu - E_g)^m}{h\nu} \qquad (3.5)$$

To estimate the indirect band gap, plot of $(\alpha h\nu)^{1/2}$ with respect to hν is used which is known as Tauc plot [74].

However, to determine Eg from the diffuse reflectance data Kubelka-Munk function $F(R_\infty)$ was assumed as it is directly proportional to the absorption coefficient [75]. $F(R_\infty)$ is the is found as follows [76]:

$$F(R_\infty) = \frac{(1 - R_\infty)^2}{2R_\infty} \qquad (3.6)$$

R_∞ is the ratio of the reflectance of a sample to the reflectance of the standard. Standard reflectance was taken as 100%. Then, plot of $(F(R_\infty)\text{-}h\nu)^{1/2}$ versus hν was constructed. By extrapolating the linear part of the plot, band gap energy was determined.

3.6 Photoelectrochemical Characterization

Cyclic voltammetry tests were conducted in the quartz single chamber photoelectrochemical cell (Pine Research Instrumentation) given in the Figure 3.3 by applying potential using VSP-300 Biologic potentiostat. CV analysis were performed in the dark and in visible light using three-electrode configuration. Illumination was supplied by LCS-100 solar simulator (Newport Co.) at 1.0 sun AM 1.5 G. Copper clip was used to the pin FTO substrate part of the film which is a working electrode for the connection. As a counter electrode, Pt wire was connected. As the reference electrode, Ag/AgCl saturated with KCl electrode was assembled. Characterization performed at room temperature in electrolyte solution 1 M sulfuric acid (H_2SO_4) with and without hole scavenger. 10%vol. methanol (CH_3OH) was preferred as hole scavenger. In acidic media, potential range was from 0 to 1.6 V (vs. Ag/AgCl) at a scan rate of 20mV/s. By using equation below (Eqn. 3.7) measured potentials were converted to the reversible hydrogen electrode (RHE) [77].

$$E_{(RHE)} = E_{Ag/AgCl} + 0.059\,pH + E^{o}_{Ag/AgCl} \tag{3.7}$$

where E_{RHE} is the converted potential, $E_{Ag/AgCl}$ is the recorded potential and $E^{\circ}_{Ag/AgCl}$ is the standard potential of $E_{Ag/AgCl}$ and is taken as 0.1976 V at room temperature (T=25 °C).

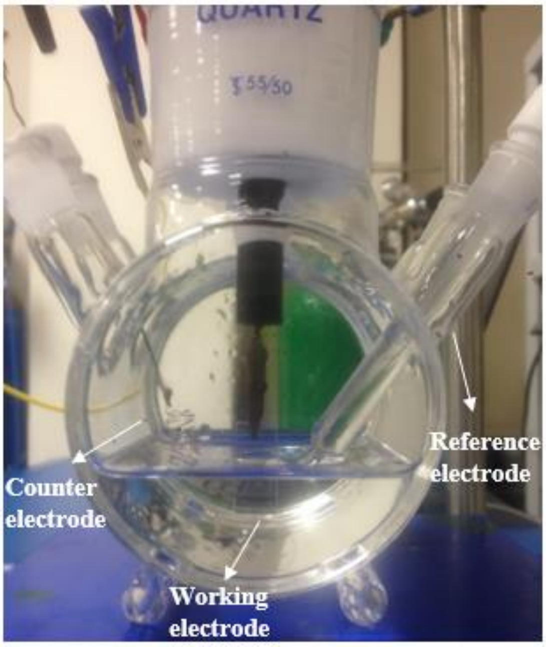

Figure 3.3 Experimental setup of the single quartz chamber photoelectrochemical cell for the photoelectrochemical characterization.

Chapter 4

RESULTS AND DISCUSSION

4.1 The Effect of Post Annealing Condition

Post calcination treatment was performed for the hydrothermally deposited WO_3 films at different temperatures (450 °C-500 °C) for a certain time range (1 h-2 h) to understand the temperature effect on the structure of the WO_3. Figure 4.1 exhibits the XRD results of prepared WO_3 films, which were prepared with a deposition time of 6 h, unannealed and post annealed (450 °C for 1 h, 450°C for 2 h and 500 °C for 1 h).

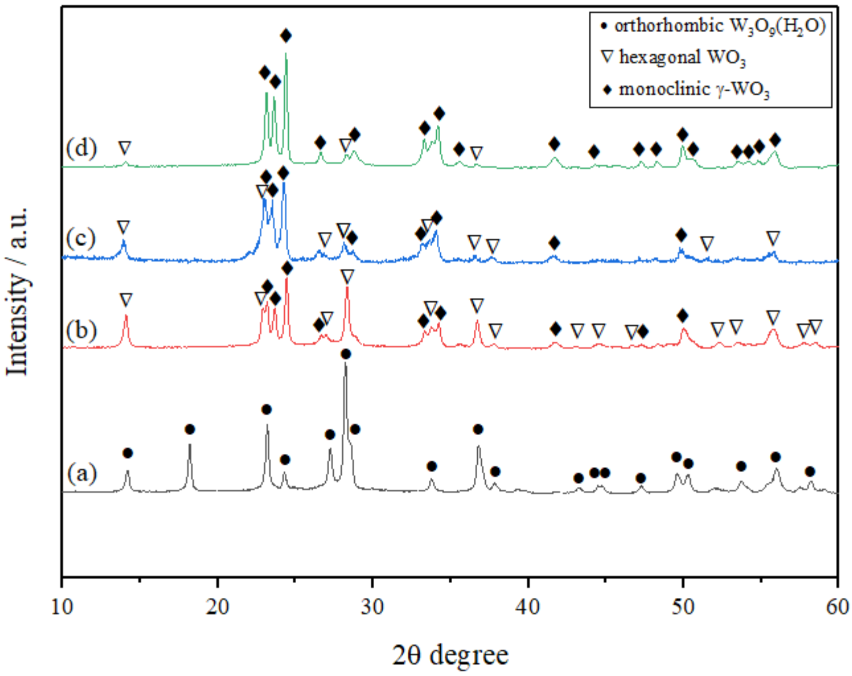

Figure 4.1 X-ray diffraction patterns of WO_3 films (a) as-prepared and annealed at (b) 450 °C for 1 h, (c) 450 °C for 2 h (d) 500 °C for 1 h. Intensities were rescaled for clearer representation.

WO_3 films prepared by hydrothermal method exhibits an orthorhombic tungsten oxide hydrate $WO_3(H_2O)_{0.33}$ structure (PDF card no. 04-011-1708). Annealed films at 450 °C for 1 h and for 2 h have both hexagonal and monoclinic structures (PDF card no. 00-033-1387 and 00-043-1035). Peak around 14° (Fig.4.1 (b) and (c)) which is an orientation of (100) face is the indicator of hexagonal structure. On the other hand, peaks between 23-25° with the orientation faces (200), (020), and (002) are strong representative of the monoclinic crystal phase [53]. Figure 4.1 (d) shows that increasing calcination temperature to 500 °C results in development of the stable monoclinic structure of WO_3.

Crystalline size of the samples was calculated using the sharpest peak at ~24 ° of the XRD spectra from the Scherrer equation. Table 4.1 shows the crystalline sizes of the WO_3 films calcined at three different conditions. Name of the sample was coded as following: HT_WO3_x_y_z. HT stands for direct hydrothermal growth, x,y and z represent the reaction deposition period, post calcination temperature and post calcination time respectively.

Table 4.1 Crystalline size of the samples HT_WO3_x_y_z

Powder Sample	Crystalline size (nm)
HT_6h_450C_1h	0.55
HT_6h_450C_2h	0.58
HT_6h_500C_1h	0.73

Increasing the annealing temperature from 450 to 500 °C resulted in increased crystalline size (0.55 nm to 0.73 nm). Hong *et al.* reported the size of the WO_3 sphere-like nanoparticles, which were produced via hydrothermal route, as 30 nm and 60 nm when the calcination performed at 500 °C and 600 °C for 10 h respectively [26]. Also, Li *et al.* reported the nanoparticle size which exhibited sphere-like features as 38 nm, 40 nm and 49 nm after the heat treatment at 450, 500 and 550 °C and for 1 h [52] . Thus, our samples displayed higher crystallite sizes compared to literature.

Raman spectra of the WO_3 films deposited for 6 h by direct growth on FTO and calcined in different conditions are consistent with the powder XRD as shown in Figure 4.2.

Strong peaks at of 715 and 807 cm^{-1} are the symmetric stretching frequencies of monoclinic O-W-O bonds and they were observed in all the samples [78,79].

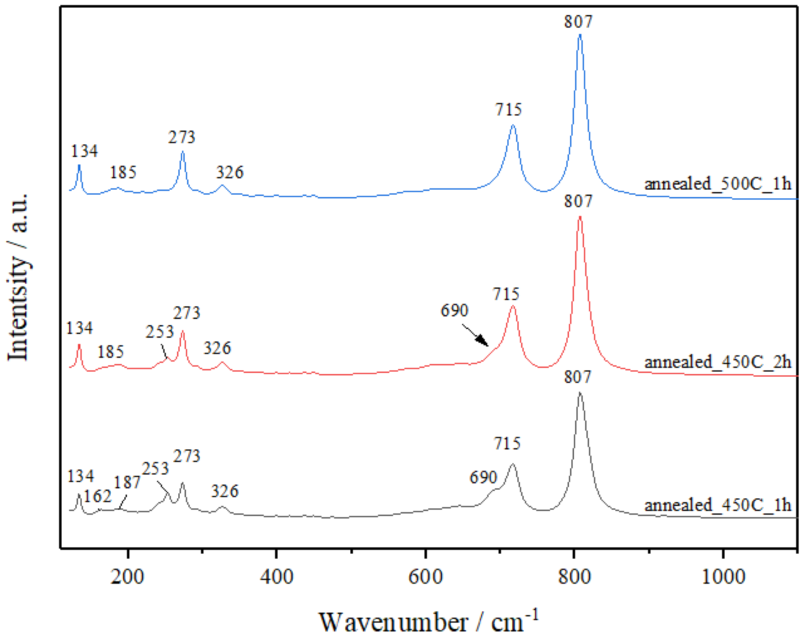

Figure 4.2 Raman spectroscopy of the films (deposited for 6 h via direct hydrothermal growth) calcined at three different conditions: at 450 °C for 1 h (black line), 450 °C for 2 h (red line) and 500 °C for 1 h (blue line).

WO_3 films annealed at 450 °C for 1 h and for 2 h have peaks which belong to both hexagonal and monoclinic structures as indicated in the results of WO_3 film XRD. Stretching bond of O-W-O at 690 cm^{-1} which belongs to hexagonal WO_3 indicate that these two samples do not have fully developed monoclinic structures. Moreover, Raman bands at 162 and 253 cm^{-1} are also indicative of the hexagonal structure of WO_3. These bands disappear with the increase in post calcination temperature and lead the monoclinic structure formation which is consistent with the XRD spectra. Bands at 134 and 187 cm^{-1} represent the lattice modes of monoclinic WO_3. Peaks around 273 and 326 cm^{-1} are assigned to bending modes of bridging oxygen belong to the monoclinic phase of WO_3.

Figure 4.3 shows the diffusive reflectance spectra and the Tauc plot of the WO_3 photoelectrodes produced at 180 °C for 6 h and calcined at various conditions (450 °C for 1 h, 450 °C for 2 h and 500 °C for 1 h).

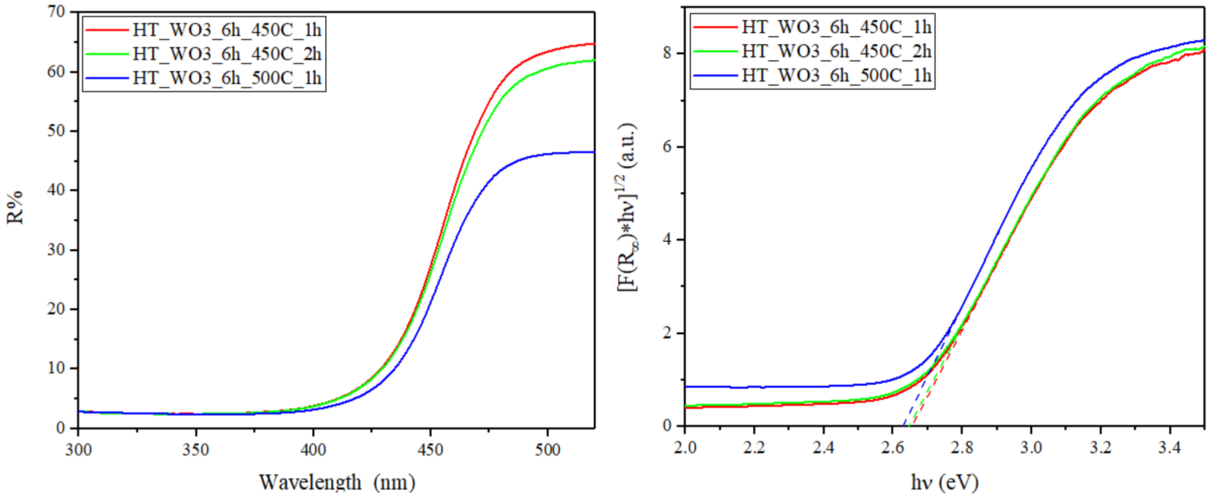

(a) (b)

Figure 4.3 (a) Uv-visible spectra and (b) Tauc plot of the WO_3 photoanodes calcined at 450 °C for 1 h (green line), 450 °C for 2 h (red line) and 500 °C for 1 h (blue line).

Band-gap energies of the hydrothermally synthesized and calcined WO_3 films were determined from the plot (Fig. 4.3) and summarized in Table 4.2.

Table 4.2 Band-gap of the samples HT_WO3_x_y_z

Sample	Eg (eV)
HT_6h_450C_1h	~2.66
HT_6h_450C_2h	~2.65
HT_6h_500C_1h	2.63

Calcination conditions have effect on crystalline size and structure as well as the band gap energy. Energy of the band-gap was shifted a little bit from the 2.66 to 2.63 eV due to the crystalline size increase [52].

Fig 4.4 shows the results of the cyclic voltammetry front-side measurements which were obtained under illumination in 1 M H_2SO_4 from the WO_3 films deposited at constant temperature and time with annealing at different conditions. Films were named as HT_WO3_x_y_z as described previously.

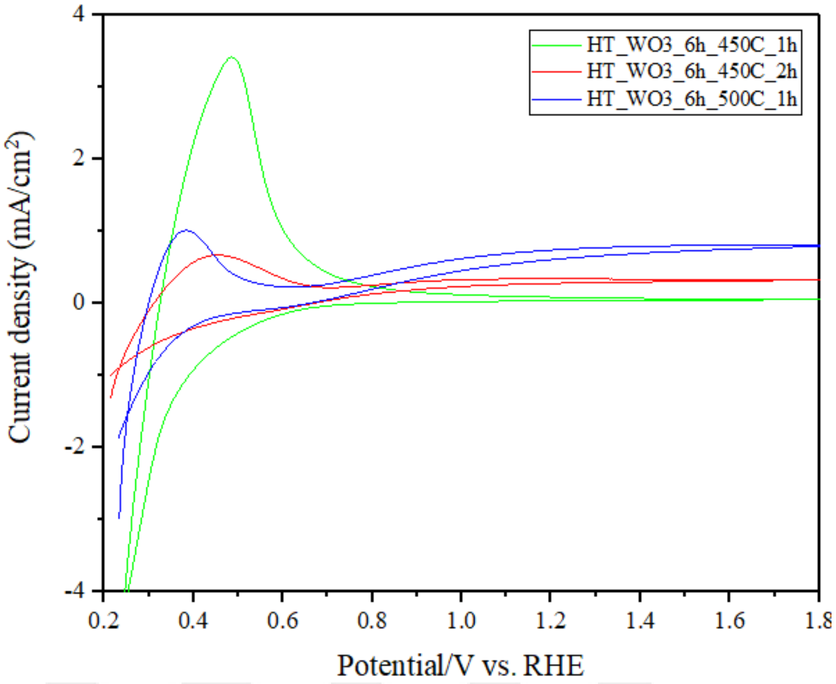

Figure 4.4 Cyclic voltammetry of the WO_3 films from the front-side illumination in 1 M H_2SO_4 electrolyte. Films were calcined at 450 °C for 1 h (green line), 450 °C for 2 h (red line) and 500 °C for 1 h (blue line).

The observed peak from the sample annealed at 500 °C for 1 h which was located between the potentials 0.0 V to 0.2 vs. SCE (0.28 V to 0.48 V vs. RHE in our measurements) was attributed to the reversible tungsten oxidation-reduction between its W^{5+} state and W^{+6} state during the photoelectrochemical measurement [80]. The large peak appeared in the sample annealed at 450 °C for 1 h indicated that the reduced tungsten state is more in this film compared to other samples.

The highest photocurrent was obtained from the film calcined at 500 °C for one hour with a value of 0.75 mA/cm^2 at 1.23 V vs. RHE. The on-set potential was recorded as 0.62 V vs. RHE. Li *et al.* also reported the on-set potential as 0.6 V vs. RHE for the photoelectrochemical measurement of WO_3 in 0.5 M H_2SO_4 but lower on-set potentials are also exist in the literature[9,52]. No significant activity was observed for the film anneal at 450 °C for 1 h. The on-set potential and current density of the WO_3 film calcined at 450 °C for 2 h were measured as 0.69 V vs. RHE and 0.34 mA/cm^2 at 1.23 V vs. RHE respectively. Hence, the post heat treatment for all hydrothermally deposited films was decided as temperature of 500 °C and 1 h. As a result, increase in crystalline size and development of a monoclinic structure have led to higher activity and lower on-set potential.

4.2 The Effect of Deposition Time

To understand the hydrothermal film growth of WO_3 on FTO, influence of the deposition period was investigated at constant temperature. For this purpose, hydrothermal reactions of were carried out at 180 °C for 1 h, 3 h, 4 h, 5 h, 6 h and 10 h. All deposited WO_3 films were subsequently calcined at 500 °C for 1 h.

Figure 4.5 shows the band-gaps of the coated WO_3 films determined from the constructed Tauc plot using reflectance data. In the figure samples were coded as HT_WO3_x_y_zwhere HT stands for direct hydrothermal growth, x,y and z represent the reaction deposition period, post calcination temperature and post calcination time, respectively.

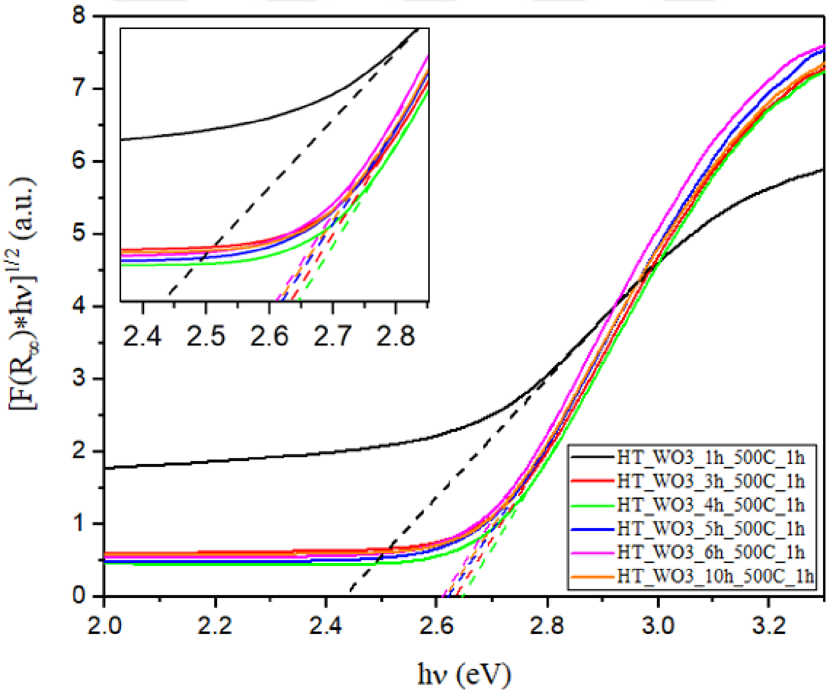

Figure 4.5 Tauc plots of WO_3 photoanodes deposited at constant temperature for different time periods and calcined at 500 °C for 1h. Deposition times are as following: 1 h (black line), 3 h (red line), 4 h (green line), 5 h (blue line), 6 h (pink line), 10 h (orange line). The inset shows the enlarged part of the corresponding band-gaps.

The indirect band gap of the annealed films was located around 2.6 eV ± 0.5 which is in good agreement with the literature [10] except for the film deposited for 1h. The corresponding bandgap energy of this film was found as 2.44 eV which was slightly lower .

XRD results of the prepared WO_3 films at various times via hydrothermal technique on FTO and annealed at 500 °C for 1 h were shown in Figure 4.6. All the films exhibited the monoclinic structure of WO_3 (PDF card no. 00-043-1035) as expected.

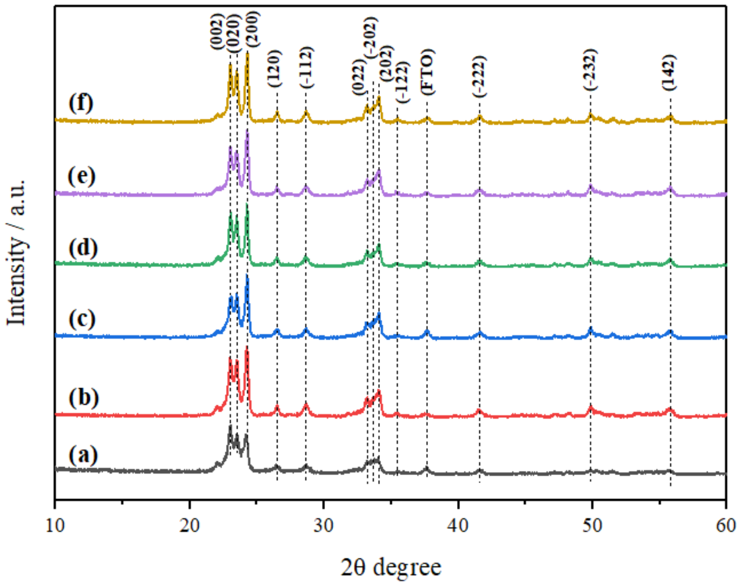

Figure 4.6 XRD spectra of the hydrothermally deposited WO_3 films on FTO at different time periods (a) 1 h, (b) 3 h, (c) 4 h, (d) 5 h, (e) 6 h and (f) 10 h. Calcination were performed at 500 °C for 1 h for all films. Face orientations and the peak assigned to the FTO were specified in brackets.

Even though the XRD measurement were done in the grazing incidence mode, the strongest peak of the substrate FTO was observed at 37.7° (PDF card no. 00-046-1088). The film deposited for 1 h has a very broad peak when the three strongest peaks of monoclinic phase which are the in the range of 23-25° were compared to others. We observed that the peaks became sharper and narrower after a 1-hour period. This indicates that crystalline sizes increased with increasing the deposition time from 1 h to a longer reaction time. More detailed morphology was examined for 1 h, 4 h, 6 h and 10 h deposited films by SEM. Figure 4.7 demonstrates the SEM images of the WO_3 films growth directly on FTO by hydrothermal method.

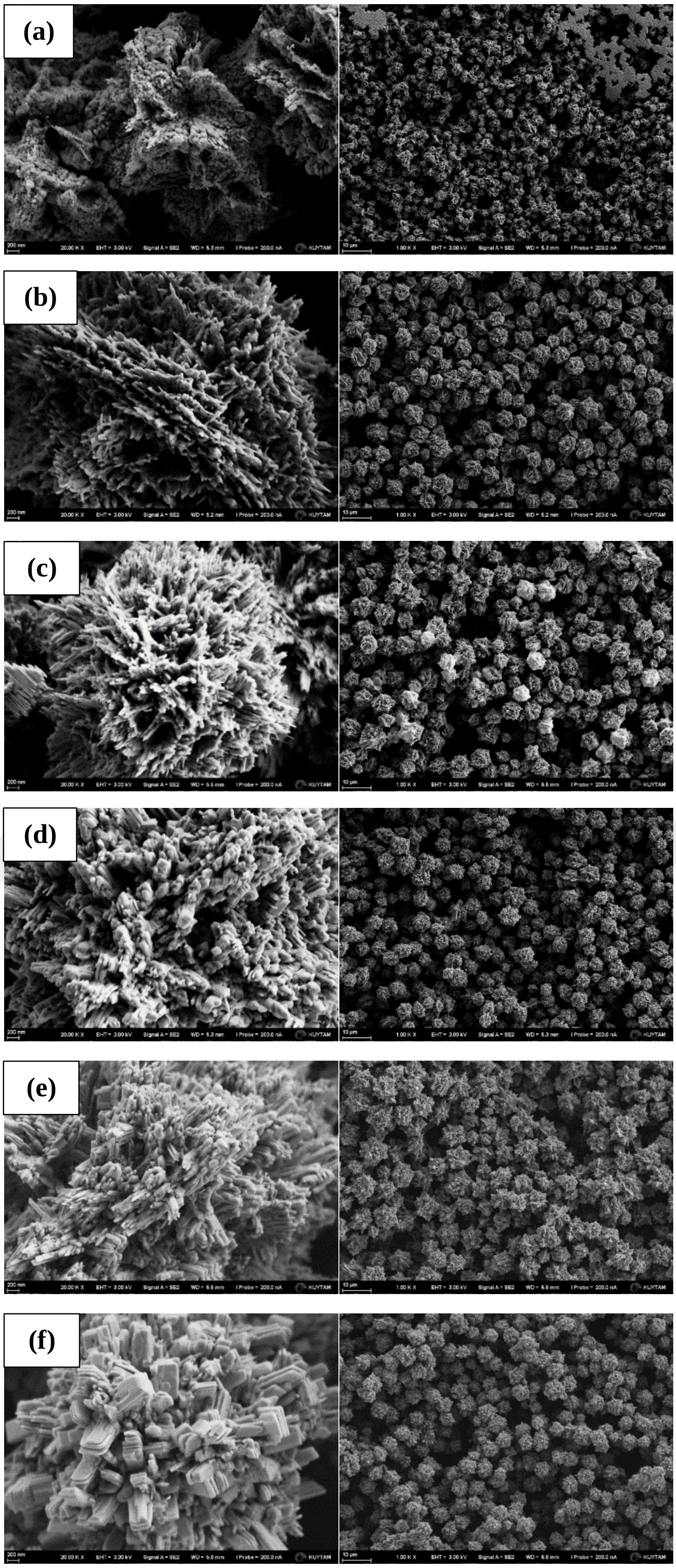

Figure 4.7 SEM images at 20 K X (on left) and 1 K X (on right) of the hydrothermally deposited WO3 films for (a) 1 h (b) 3 h, (c) 4 h and (d) 5 h (e) 6 h and (f) 10 h. All films were annealed at 500 °C for 1 h.

1-hour reaction time is not enough for the fully developed structure. However, in 3 h period, we observed the settled porous nanoparticles. With increasing reaction time, thorny structure of a nanoparticle got thicker.

Figure 4.8 demonstrates the SEM images of the WO_3 films in cross-sectional view which were produced via hydrothermal method.

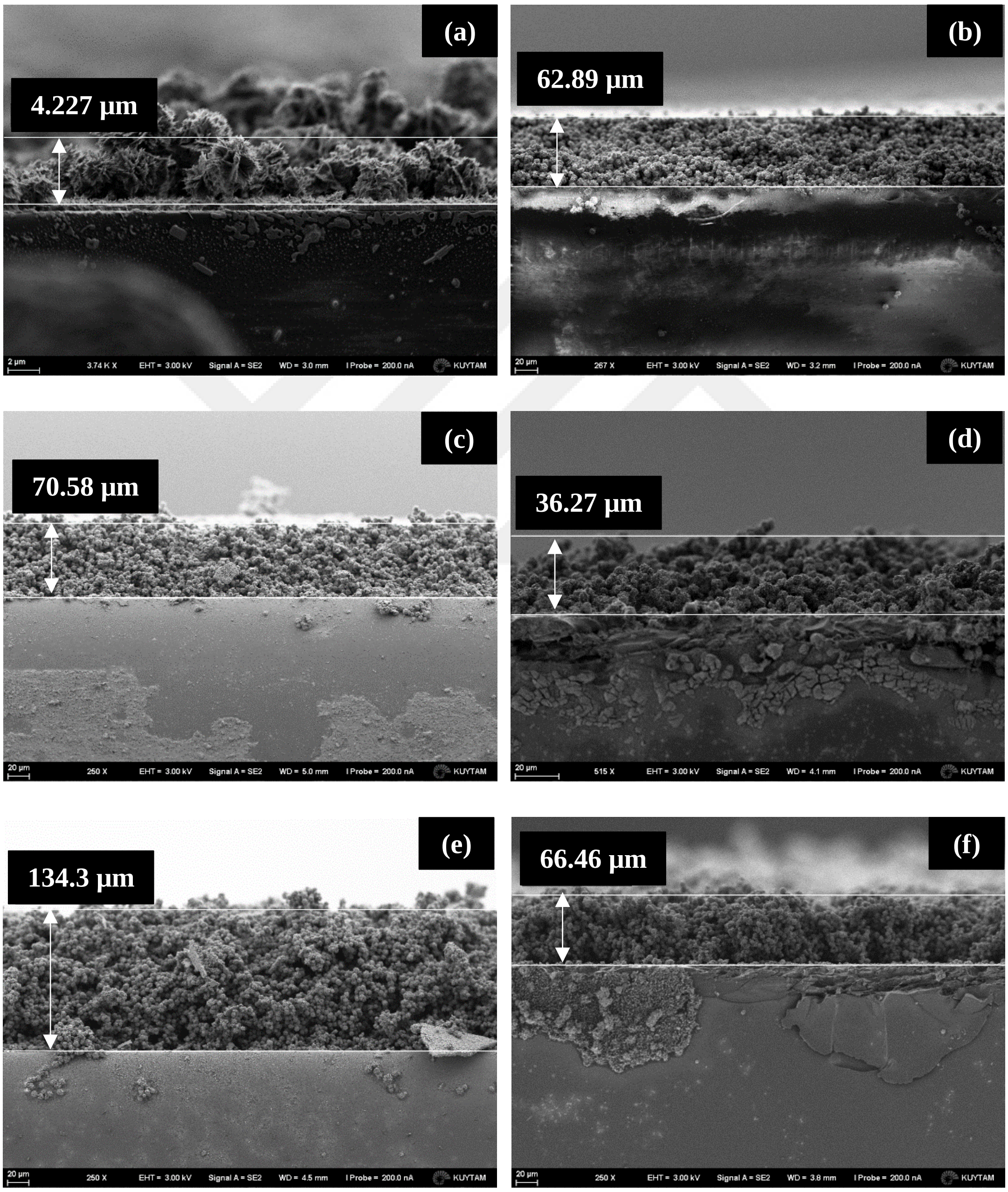

Figure 4.8 SEM images in cross-sectional view of WO_3 film produced directly on FTO glass deposited for (a) 1 h (b) 3 h (c) 4 h (d) 5 h (e) 6 h and (f) 10 h. All films calcined at 500 °C for 1 h.

The measured film thicknesses were 2.29, 70.58, 134.3 and 66.46 µm for the films deposited at 1 h, 4 h, 6 h, and 10 h respectively. Increasing reaction time from 1 h to 6 h lead to a thicker film, but further increase to 10 h caused to weak adhesion on FTO and peeling of the film from the surface.

Figure 4.9. shows the results of the cyclic voltammetry under illumination in 1 M H_2SO_4 obtained from the WO_3 films deposited at constant temperature with various deposition periods. Films were named as HT_WO3_x_y_z as previous.

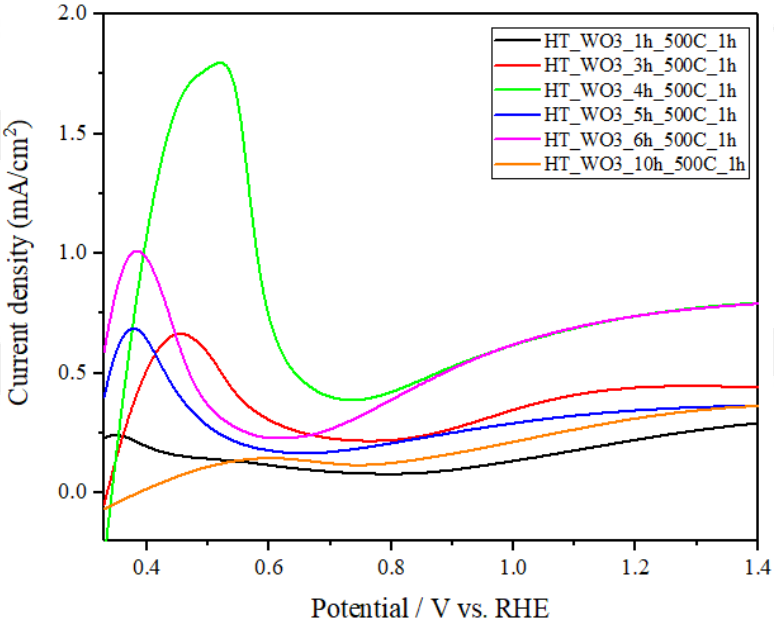

Figure 4.9 Cyclic voltammetry of the WO_3 films from the front-side illumination in 1 M H_2SO_4 electrolyte.

The peak between 0.28 to 0.48 V was the indicator of the reversible reaction was occurred between the tungsten states of +5 and +6. This peak was observed as shifted from the samples deposited for 1 h, 3 h, 4 h and 10 h. The reason of the peak was observed in the varied potential range could be the reduction of tungsten to another oxidation states different from W^{+5}.

The recorded on-set potentials and current densities at 1.23 V are given in Table 4.3.

Table 4. 3 Results of the CV measurements under illumination for the films deposited at various time

Sample name	On-set potential [V vs. RHE]	Current density at 1.23 V vs. RHE [mA/cm^2]
HT_WO3_1h_500C_1h	0.81	0.23
HT_WO3_3h_500C_1h	0.80	0.44
HT_WO3_4h_500C_1h	0.74	0.75
HT_WO3_5h_500C_1h	0.71	0.35
HT_WO3_6h_500C_1h	0.62	0.75
HT_WO3_10h_500C_1h	0.77	0.32

The highest photocurrents were obtained from samples deposited for 4 h and 6 h as 0.75 mA/cm^2. However, by coating FTO for 6 h hydrothermally, the onset potential was decreased by 19.35 % compared to deposition period of 4 h.

Further photoelectrochemical measurements were done from the WO_3 film produced at 180 °C for 6 h with a post heat treatment in air at 500 °C for 1 h. Illumination with AM 1.5 G solar simulator was applied on the front side and back side of the WO_3 films deposited on FTO conductive substrate in 1 M H_2SO_4 and in 1 M H_2SO_4 with 10 vol.% CH_3OH aqueous solution. Figure 4.10 illustrates the plot of the photocurrent versus applied voltage with respect to RHE under dark and under illumination from front and back in 1 M H_2SO_4 with and without methanol.

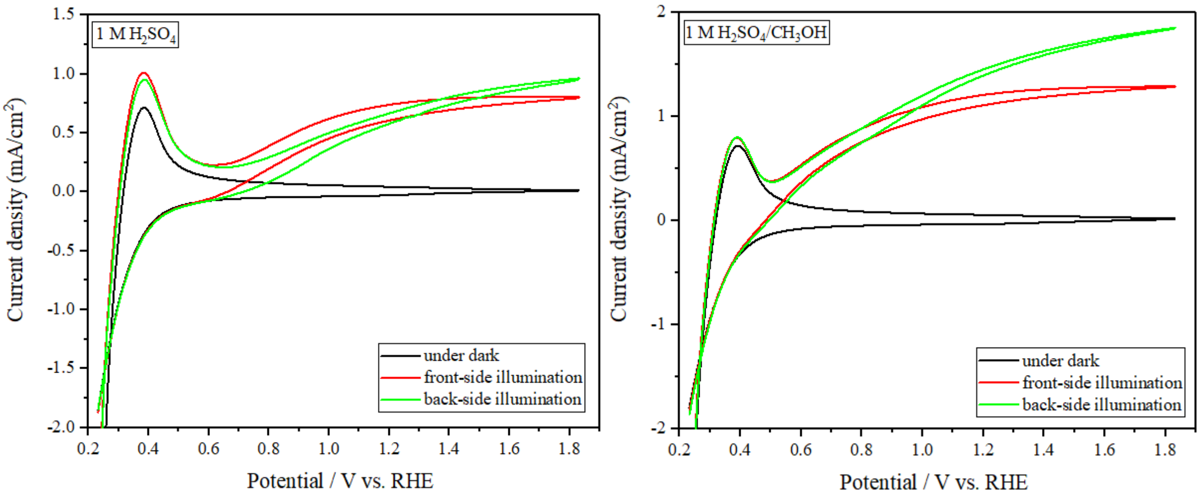

(a) (b)

Figure 4.10 Current density versus applied potential plot of the WO_3 film under dark (black line), front illumination (red line) and back illumination (green line) (a) in 1 M H_2SO_4 aqueous solution (b) in 1 M H_2SO_4/CH_3OH aqueous solution.

In an ideal case, same activity should be observed from the front and back side measurements. The sharper increase was observed in the back-side measurement in the 1 M H_2SO_4 solution . Even though a little difference were obtained up to 1.3 V in 1 M H_2SO_4 electrolyte (Fig. 4.10 (a)), there was a significant difference between the side illuminations in solution with hole scavenger (Fig. 4.10 (b)). In back-side illuminations, electrons travel less distance than the front illumination to the conductive side since the light is absorbed near the FTO in the back-side measurements. Thus, a higher photocurrent density shows that there is a problem in electron transport. The light cannot penetrate to deep side of the samples during front irradiation and it causes only the excitement of the outer surface electrons. These electrons have longer path to reach conductive side. In an extended path, possibility of recombination is higher, or electron mean free path is not long enough to travel to conductive side. This situation is commonly observed in thick films [26]. Therefore, thinner films were desirable. However, trials with direct hydrothermal method were not satisfactory so that an alternative approach to make WO_3 film was tried. WO_3 powder was produced via hydrothermal method and a solution was prepared a suspension of these particles in ethylene glycol. Then, WO_3 electrode was produced by drop casting this solution onto FTO.

4.3 Characterization and Photoactivity Of the Thin WO_3 Film Produced from The Colloidal Solution

WO_3 films were produced by using ethylene glycol as binder and as-synthesized WO_3 powder prepared at 180 °C for 6 h. Post calcination was performed at 500 °C for 1 h. Figure 4.11 demonstrates the SEM images of the thinner film.

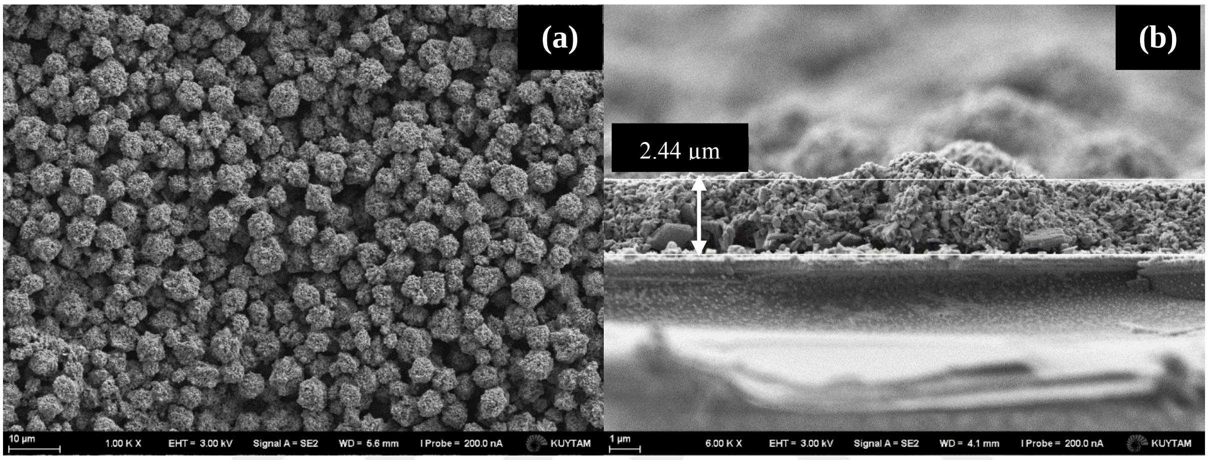

Figure 4.11 SEM images of the WO_3 film prepared from the colloidal solution (a) top view (b) cross-sectional view.

Morphology of the film was very similar to the 6 h deposited WO_3 film via direct growth on FTO. 2.44 µm film thickness was obtained which is very thin compared to the films grown directly on the substrate.

To obtain monoclinic structure, calcination was performed. By this treatment, also all the ethylene glycol was removed and bonding of the film to the FTO surface was improved and the bandgap energy. Figure 4.12 illustrates the band gap energies of the unannealed/as-prepared and annealed films. Films prepared from the suspended powder solution were named as HTP_WO3.

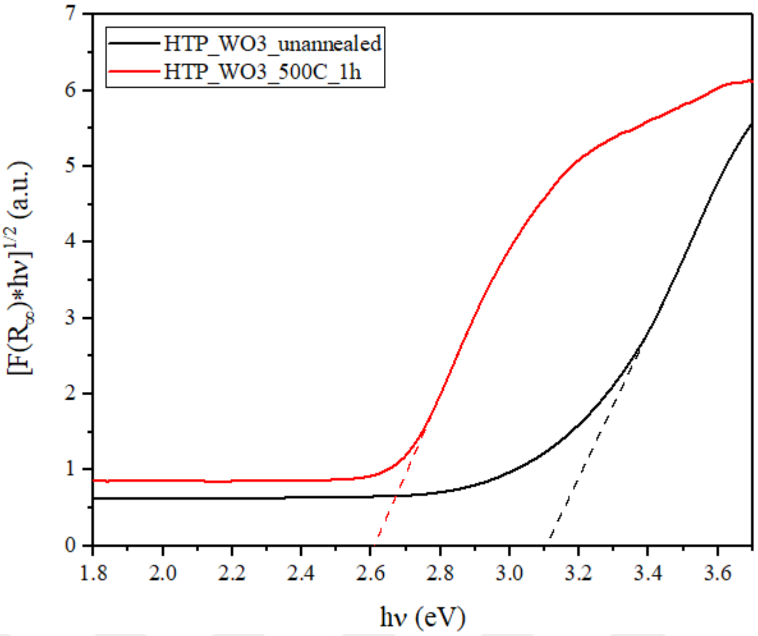

Figure 4.12 Tauc plot of the WO_3 film produced from the suspended solution as-prepared (black line) and annealed at 500 °C for 1 h (red line).

Indirect band gap of the film was decreased from 3.1 eV to 2.6 eV by annealing. Band gap energy of this film was obtained as same as the films which were produced via direct growth on FTO. Also, by heat treatment, color change from white to yellow was observed. Figure 4.13 shows the photographs of HTP_WO3 films before and after annealing.

(a) (b)

Figure 4.13 HTP_WO3 films (a) as-prepared/unannealed and (b) annealed at 500 °C for 1 h.

Figure 4.14 shows the photoelectrochemical test results performed in the dark and in the light from the both sides of the WO_3 thin electrode in 1 M H_2SO_4 acidic region.

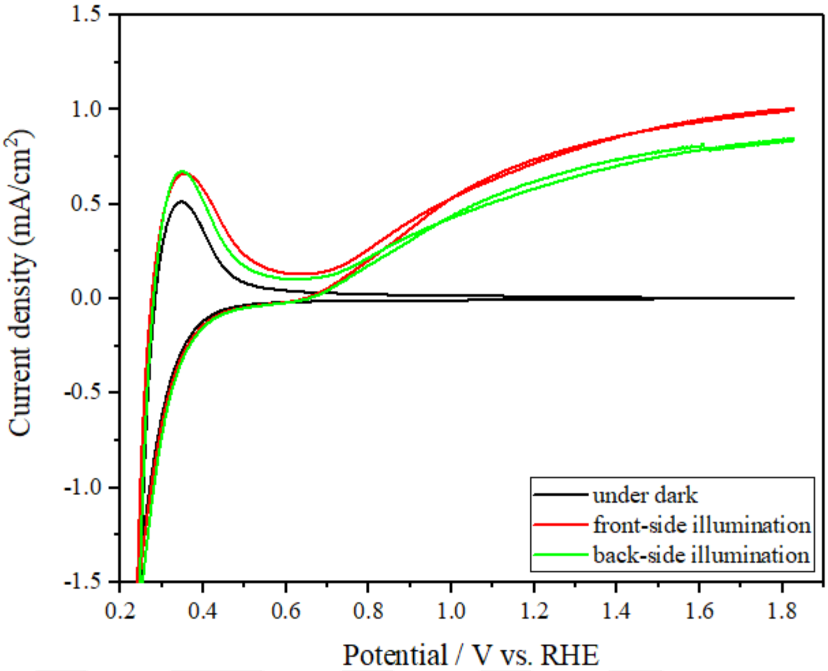

Figure 4.14 Cyclic voltammetry of WO_3 thin film under dark (black line) under illumination from front-side (red line) and back-side (green line) in 1 M H_2SO_4.

The on-set potential was recorded as 0.63 V vs. RHE and the maximum current at 1.23 V was found as 0.76 mA/cm^2 from the front-side measurement. Photocurrent at 1.23 V from the back-side illumination was 0.64 mA/cm^2. In this film, lower photocurrent with back side illumination was observed unlike the previous film. This means that electrons transport is easier than the hole transport since the hole travels longer path which increases the possibility of recombination. [4].

Figure 4.15 demonstrates the photoelectrochemical test results performed in the dark and in the light from the both sides of the WO_3 thin electrode in 1 M H_2SO_4 with hole scavenger.

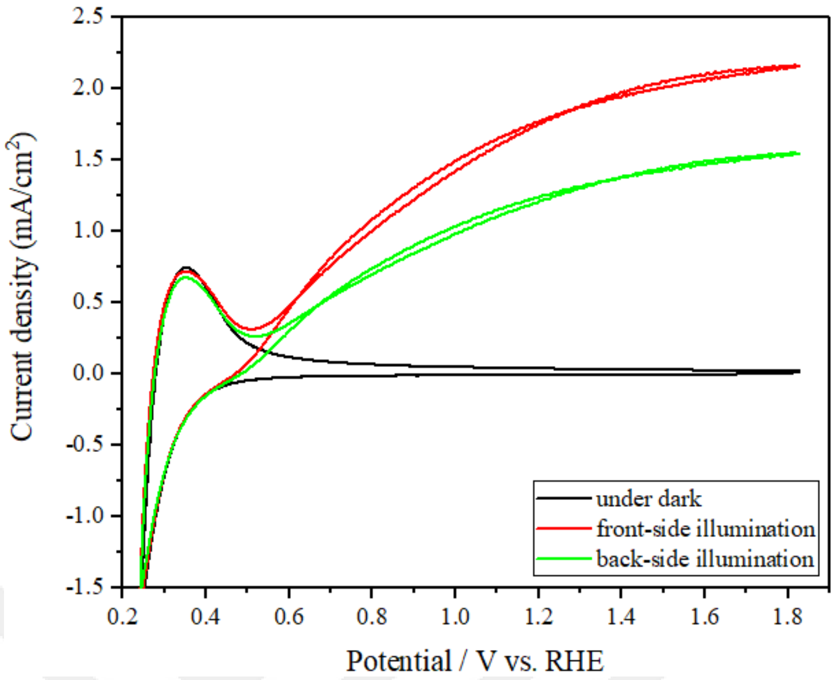

Figure 4.15 Cyclic voltammetry of WO_3 thin film under dark (black line) under illumination from front-side (red line) and back-side (green line) in 1 M H_2SO_4/CH_3OH solution.

Introducing methanol as a hole scavenger into the acidic medium enhances the photoactivity by 81.58% (measured value is 1.81 mA/cm^2 from front irradiation at 1.23 V) from the front side and lowers the on-set potential from 0.63 V to 0.51 V as expected. Photocurrent density from the back side was found as 1.26 mA/cm^2 at 1.23 V.

To make a comparison between the WO_3 photoelectrodes, the photocurrent densities obtained under front-side illumination from the WO_3 film growth directly on FTO at 180 °C for 6 h and WO_3 thin film produced from the colloidal solution via drop-casting on FTO were illustrated in Figure 4.16.

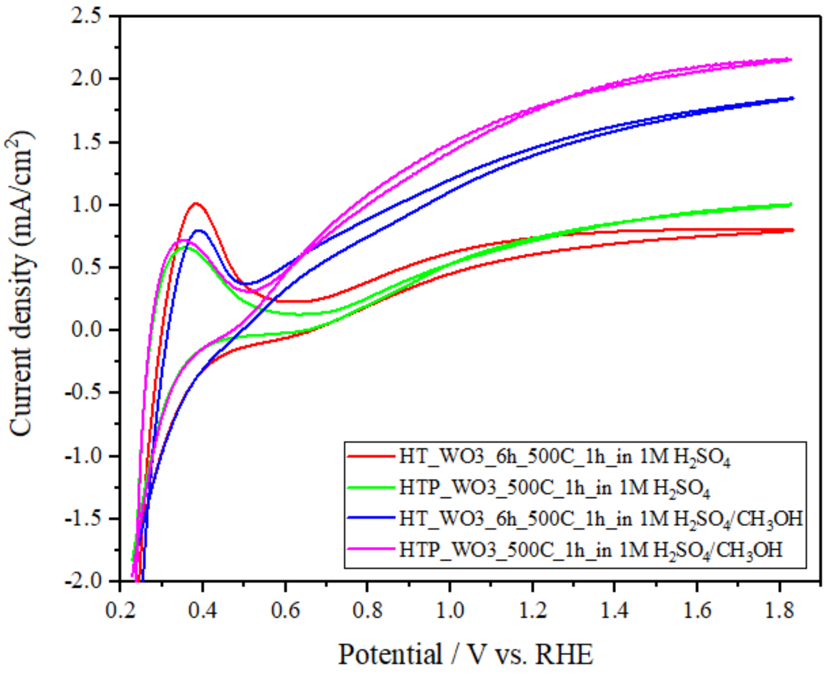

Figure 4.16 Comparison of the photoelectrochemical measurements of the WO_3 films growth directly and coated via drop casting performed under front side illumination with and without methanol.

Corresponding lines to the measurements are as following: red line- photocurrent density of the film directly grown in 1 M H_2SO_4, green line- photocurrent density of the thin film via drop-cast in 1 M H_2SO_4, blue line- photocurrent density of the film directly grown in 1 M H_2SO_4/CH_3OH and pink line- photocurrent density of the thin film via drop-cast in 1 M H_2SO_4/CH_3OH

The photocurrent densities at 1.23 V obtained with front side illumination in 1 M H_2SO_4 of the samples coated from the colloidal solution and WO_3 film produced hydrothermally at 180 °C for 6 h by direct growth were very similar. Higher activity was obtained with the WO_3 film produced by drop casting with the further increase in applied potential. More enhancement of the photoactivity was observed in the measurements performed in the solution with hole scavenger. For instance, we observed 48.36 % increase (from 1.22 mA/cm^2 to 1.81 mA/cm^2) in the photo density measured at 1.23 V.

To understand the material synthesis steps and effect of the photoelectrochemical measurement on a sample, Raman spectroscopy of the films as-prepared, annealed and after photoelectrochemical characterization was investigated. Figure 4.17 shows the results of the Raman spectra.

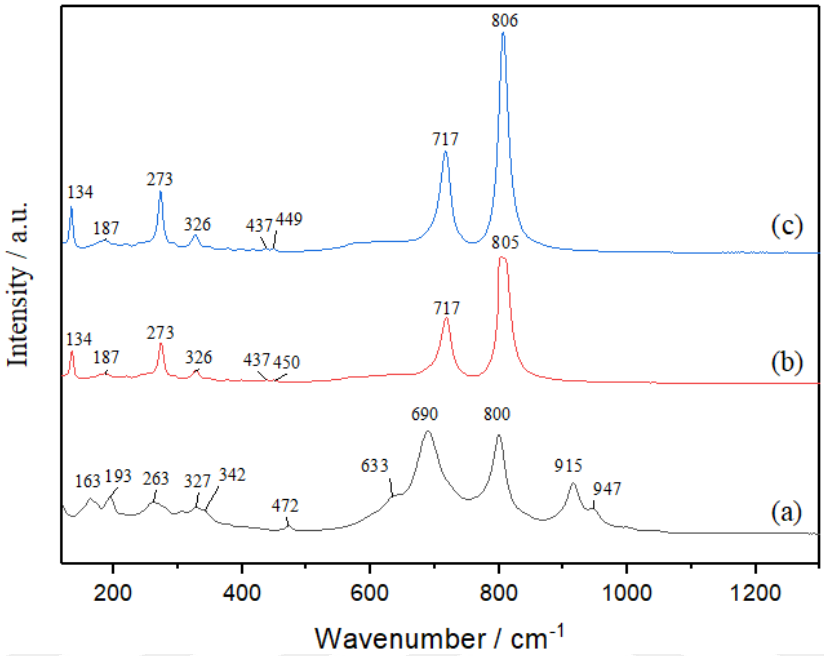

Figure 4.17 Raman spectroscopy of the WO_3 sample produced from the colloidal solution (a) as prepared (b) calcined at 500 °C for 1 h (c) after photoelectrochemical test in 1 M H_2SO_4 aqueous solution.

We observed bands which belong to the hydrated form of WO_3 in the Raman spectra of the as prepared sample (Fig.17 (a)). Bands at 947 and 915 cm^{-1} can be ascribed as the split band of the stretching O=W bond of the $WO_3.H_2O$ at 960 cm^{-1}. These hydrate peaks disappeared with the annealing. A sharp peak at 800 cm^{-1} was observed due to the vibrations of bridging oxygen [81]. The other sharp peak at 690 cm^{-1} corresponds the stretching O-W-O bond of the hexagonal WO_3. Shoulder at 633 cm^{-1} can be assigned as the *v*(O-W-O) bond of the hydrate form of the tungsten oxide ($WO_3.H_2O$) [78]. The small peak formed at 472 cm^{-1} can be ascribed as the vibrational mode of the O-W-O bond belonging to the monoclinic structure at 434 cm^{-1}. After calcination this peak shifted to the 437 cm^{-1}. Also, the peak at 342 cm^{-1} can be attained as the *v*(W-OH_2) which was reported as peak at 377 cm^{-1}. This distinction can be clarified by contrasts within the coordination conditions of H_2O molecules [81]. Peak at 327 cm^{-1} corresponds to the *v*(O-W-O) bond of the monoclinic WO_3 [78].

Appeared band at 263 cm^{-1} can be attributed as the δ(O-W-O) of the $WO_3.H_2O$ form. This peak was actually reported at wavenumber at 270 cm^{-1}. The reason of this differences might be bonding coordination of the H_2O molecules. Another bond peak belongs to the hydrate form ($WO_3.H_2O$) appeared at 193 cm^{-1} which corresponds to the stretching bond of W-O-W. Last peak appeared at 162 cm^{-1} shows the lattice bond of hexagonal WO_3. We observed no peaks belonging to ethylene glycol. This means that removal all ethylene glycol was achieved by drying the sample at 100 °C for 4.5 h. On the other, any change in the structural phase was not observed by drying at 100 °C as Santato *et al.* reported [13]. As in the unannealed WO_3 film directly growth on FTO via hydrothermal method (see Fig. 4.1 (a)), hydrate form of tungsten oxide was observed from the as-prepared WO_3 film.

After photoelectrochemical measurement, no specific changes observed compared to the WO_3 film calcined at 500 °C for 1 h. Obtained peaks at 805, 717, 450, 437, 326,273, 187 and 134 cm^{-1} correspond to monoclinic structure of WO_3 as the calcined film at 500 °C for 1 h produced via direct growth on FTO (see Fig. 4.2) [78].

4.4 New Developed Supercritical CO_2 Method for WO_3 film Deposition

4.4.1 Determination of $W(CO)_6$ solubility in $scCO_2$

Solubility of the $W(CO)_6$ was determined. Pressures, which all the $W(CO)_6$ was dissolved in the supercritical phase was measured as 1211 psi and 1525 psi at 35 °C and at 45 °C respectively. The density of the CO_2 was found from the NIST Chemistry Webbook at each condition. By knowing the mass of the $W(CO)_6$ placed inside the vessel, mole fraction solubility values were determined as $1.97x10^{-3}$ at 35 °C and 1211 psia and $4.1x10^{-3}$ at 45 °C. and 1525 psia. Even at low temperatures, solubility is quite high. This might be the reason of not observing cloud point while depressurizing the vessel.

Additional solubility experiment was performed for the film deposition conditions (T=80 °C and P=1200 psi, without stirring) in a cold-wall reactor to determine the time of the precursor dissolution in $scCO_2$. Complete dissolution of the $W(CO)_6$ at film deposition conditions were observed after 2.5 hour later without using the magnetic stirrer.

4.4.2 Temperature and Pressure Profiles During Film Deposition

Temperature and pressure values were recorded every minute until reaching the set temperature (300 °C). After this point, data were collected every hour. Figure 4.18 shows the temperature profile during the cold-wall operation. Tstage and Tvessel represent the temperature of the stage and the vessel, respectively. Heating stage reached the desired temperature in ~60-70 minutes. The reason why it takes so long is that the rate of removal of heat from the stage is quite high due to high heat capacity and thermal conductivity of the sc-CO_2. It was found that wrapping insulating cloth around the side of the stage reduce the rate of heat loss. We observed that depositing at higher initial pressure values caused the larger rates of heat removal from the heating pedestal since the heat capacity of the supercritical CO_2 increased due to its increasing density. In these cases, it was not possible for the stage to reach 300 °C.

Increase in temperature caused an increase in the temperature of the fluid inside the vessel as expected. ~170 °C temperature difference between the stage and the sc-CO_2 fluid phase could be obtained as seen in Figure 4.18.

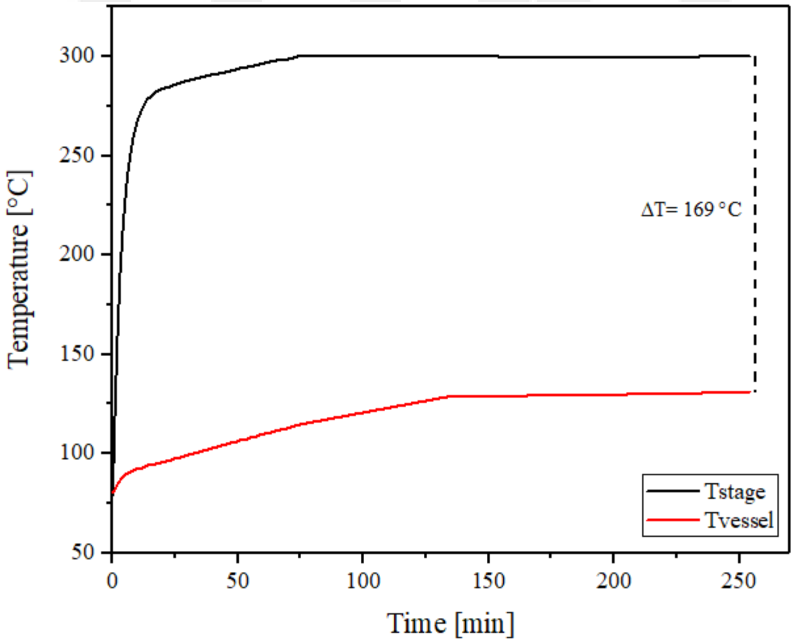

Figure 4.18 Temperature profile of the stage and vessel during film deposition.

Figure 4.19 shows the increase of the sc-CO_2 pressure since the temperature was increasing the vessel while the stage heater was running.

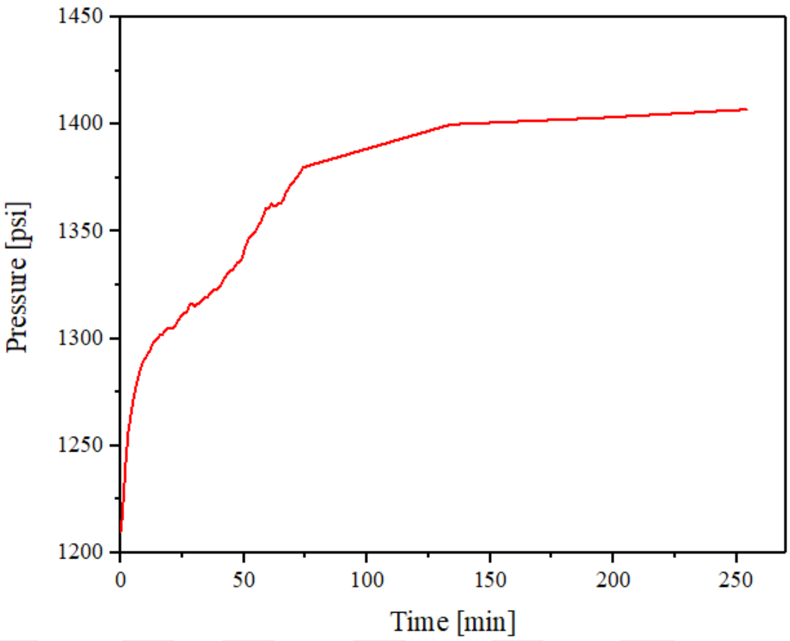

Figure 4.19 Pressure profile of the sc-CO_2 during film deposition.

4.4.3 Material properties of WO_3 films

WO_3 films were deposited on FTO in a cold-wall reactor in 4 different ways. In the production of WO_3 from $W(CO)_6$, needed oxygen ratio was 4.5 mol for 1 mol $W(CO)_6$ from the stoichiometry. The least amount of O_2 required for our experiments was found as 8.95×10^{-4} moles. The first WO_3 film was deposited in the presence of air for 3 h was named as scCO2_WO3_3h. From the presence of air at 1 atm, amount of the O_2 was determined as 9.38×10^{-4} moles which slightly higher than needed. The second film was produced by filling O_2 at first and dissolving precursor in the mixture of sc-CO_2 and oxygen. The film was deposited for 3 h and was called as scCO2_WO3_O2_3h. The amount of 8.07×10^{-3} moles was found from oxygen placed in the vessel at 2 bars. The next film deposited by O_2 injection. During deposition 1 h was waited without oxygen and 3 h was waited after introducing O_2- in total 4 h was recorded as deposition time. The WO_3 film was coded as scCO2_WO3_O2inj_4h. The last type of the WO_3 film was deposited for 4 h after injection of the O_2 gas to the vessel when the stage reached to desired temperature. After annealing film at 500 °C for 1h, it was used as seed layer and film growth was performed as the same method of the seed layer production. This film was named as scCO2_WO3_O2inj_4h_2layer. Amount of the injected oxygen from small vessel to the cold-wall reactor was determined from mass balance as 1.3×10^{-3} moles. In this section, given names were used for simplicity. Figure 4.20 illustrates the images of the deposited films scCO2_WO3_O2_3h and scCO2_WO3_O2inj_4h.

Figure 4.20 The images of the WO_3 films deposited via SCD in a cold-wall reactor (a) scCO2_WO3_O2_3h (b) scCO2_WO3_O2inj_4h.

4.4.3.1 Material Properties of Film Deposited with No Additional Oxygen

Raman spectra of the prepared films were examined to understand the film formation. The Raman spectroscopy of the as prepared and annealed WO_3 films deposited in the presence of air are shown in Figure 4.21. Peaks which belongs to the FTO substrate are specified with the dashed line.

In the Raman spectra of unannealed WO_3 film, peaks at 1360 cm^{-1} and 1590 cm^{-1} can be as attributed to D and G band of the disordered carbon [82]. Both peaks disappeared with the calcination of the film as expected. Band at 910 cm^{-1} can be attributed to the stretching modes of nonstoichiometric WO_{3-x}. Frey *et al.* reported that hexagonal channelled- W_5O_{14} material contains peak at 900 cm^{-1} which corresponds to the W-O-W stretching mode [83]. Also, wavenumber range between 960 cm^{-1} and 800 cm^{-1} corresponds to the stretching mode [78]. Band at 794 cm^{-1} can be assigned as the W-O stretching vibration [84]. Small peaks in the range of 200 to 400 cm^{-1} (397, 354, 332 and 201 cm^{-1}) can be attributed to the bridging mode of tungsten oxide [78]. From these results, no structural phase of WO_3 can be assigned to the as-prepared scCO2_WO3_3h.

From the sample calcined at 500 °C for 1 h, stretching modes of O-W-O monoclinic WO_3 was observed which is represented by the peak at 809 cm^{-1} and 706 cm^{-1}. O-W-O bending mode of the bridging oxygen corresponds the peaks around 270 cm^{-1} and 326 cm^{-1} [78]. Lattice modes of monoclinic phase is also specified by peaks at 187 and 133 cm^{-1}.

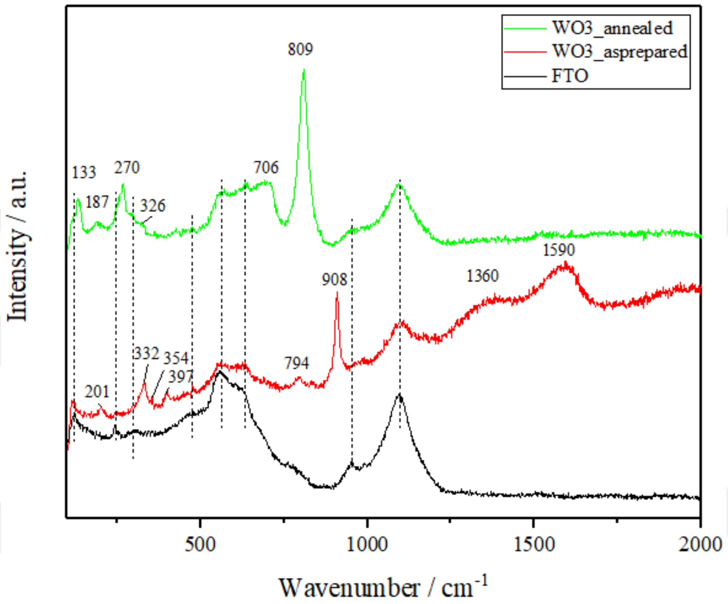

Figure 4. 21 Raman spectra of FTO (black line), scCO2_WO3_3h film as prepared (red line), scCO2_WO3_3h film annealed at 500 °C for 1 h (green line). Intensities were rescaled for clearer representation.

Morphology of the annealed scCO2_WO3_3h film was investigated via SEM. Figure 4.22 illustrates the top view SEM images of the WO_3 films and bare FTO substrate in different magnifications.

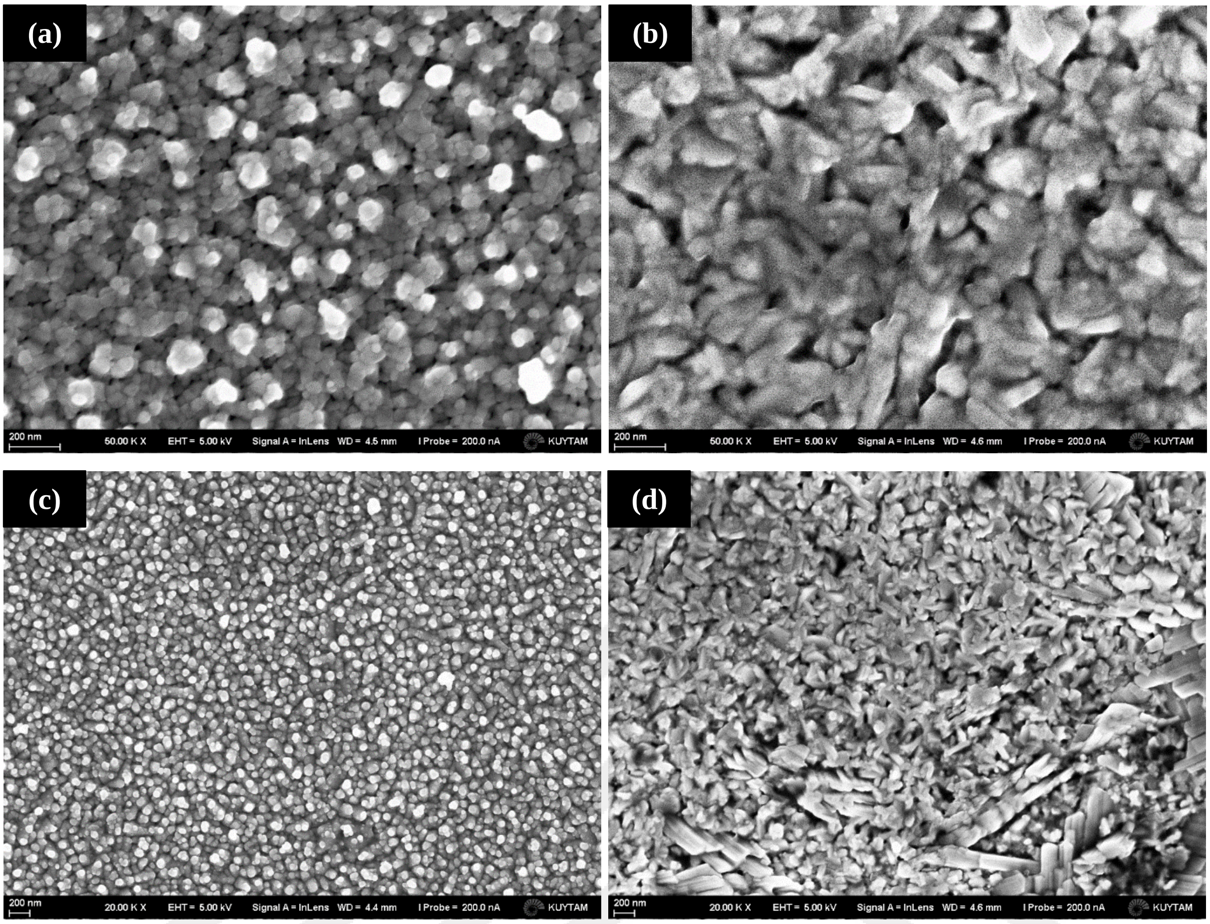

Figure 4.22 SEM images of calcined scCO2_WO3_3h films (a,c) and bare FTO substrate (b,d) in different magnifications.

EDX data obtained from the annealed WO_3 film on FTO is given in Figure 4.23. Tungsten and oxygen were detected by the EDX along with Sn which belongs to the FTO substrate.

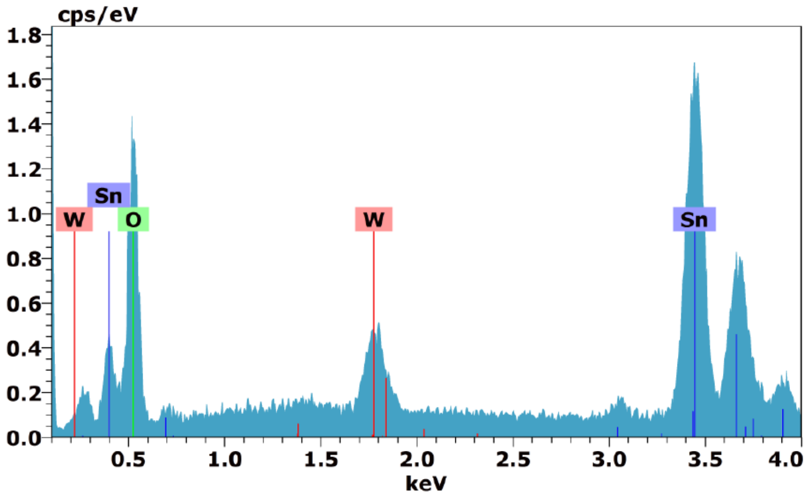

Figure 4. 23 EDX spectra of scCO2_WO3_3h film calcined at 500 °C for 1 h.

SEM images showed that surface of the FTO is coated and EDX data confirmed the presence of tungsten. It was hard to determine the coating on FTO was corresponded to the tungsten oxide film or not from the EDX data since the oxygen signals were also obtained from the FTO glass. However, the tungsten oxide film deposition was confirmed via Raman analysis. Also, from the EDX signals, the film coating was very thin since the tungsten to tin ratio was very low.

4.4.3.2 Material Properties of Film Deposited with Addition of Oxygen

Raman spectra of the WO_3 films coated on FTO by adding oxygen before filling the vessel with CO_2 was taken. Figure 4.24 shows the Raman spectroscopy of the scCO2_WO3_O2_3h films as prepared and annealed. Peaks belongs to the FTO substrate are specified with the dashed line.

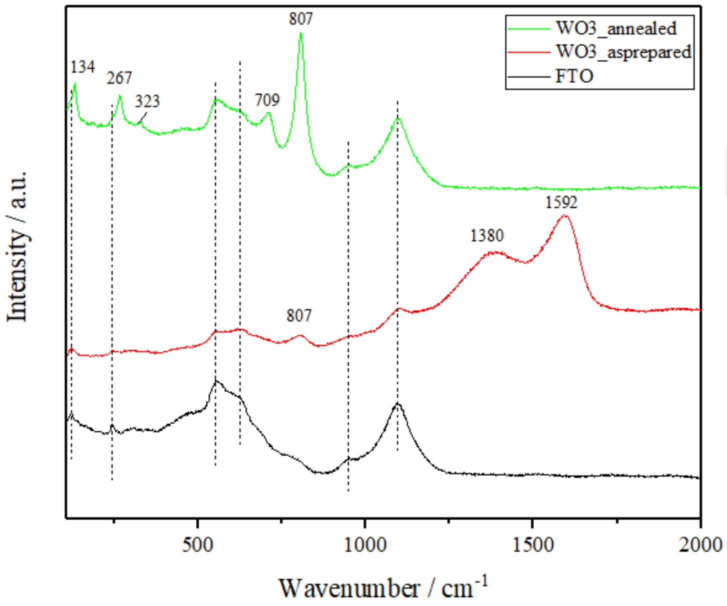

Figure 4. 24 Raman spectra of FTO (black line), scCO2_WO3_O2_3h films as prepared (red line) and annealed at 500 °C for 1 h (green line). Intensities were rescaled for clearer representation.

The spectra from as prepared film contains disordered carbon peaks at 1380 and 1592 cm^{-1}. Also, at wavenumber of 807 cm^{-1} stretching bonds of O-W-O which belongs to the monoclinic WO_3 were observed. After calcination, carbon peaks disappeared, and new peaks arose at 134, 267, 323 and 709 cm^{-1}. 134 cm^{-1} corresponds to the lattice bond of monoclinic WO_3. Bands at 267 and 323 cm^{-1} are very close to the vibrational mode of O-W-O bond.

Peaks at 709 cm^{-1} is also assigned to the O-W-O stretching modes of WO_3 monoclinic phase [78].

SEM images were taken to analyse surface morphology of the coated FTO. Figure 4.25 shows SEM images of the WO_3 films and bare FTO substrate from the top view in various magnifications.

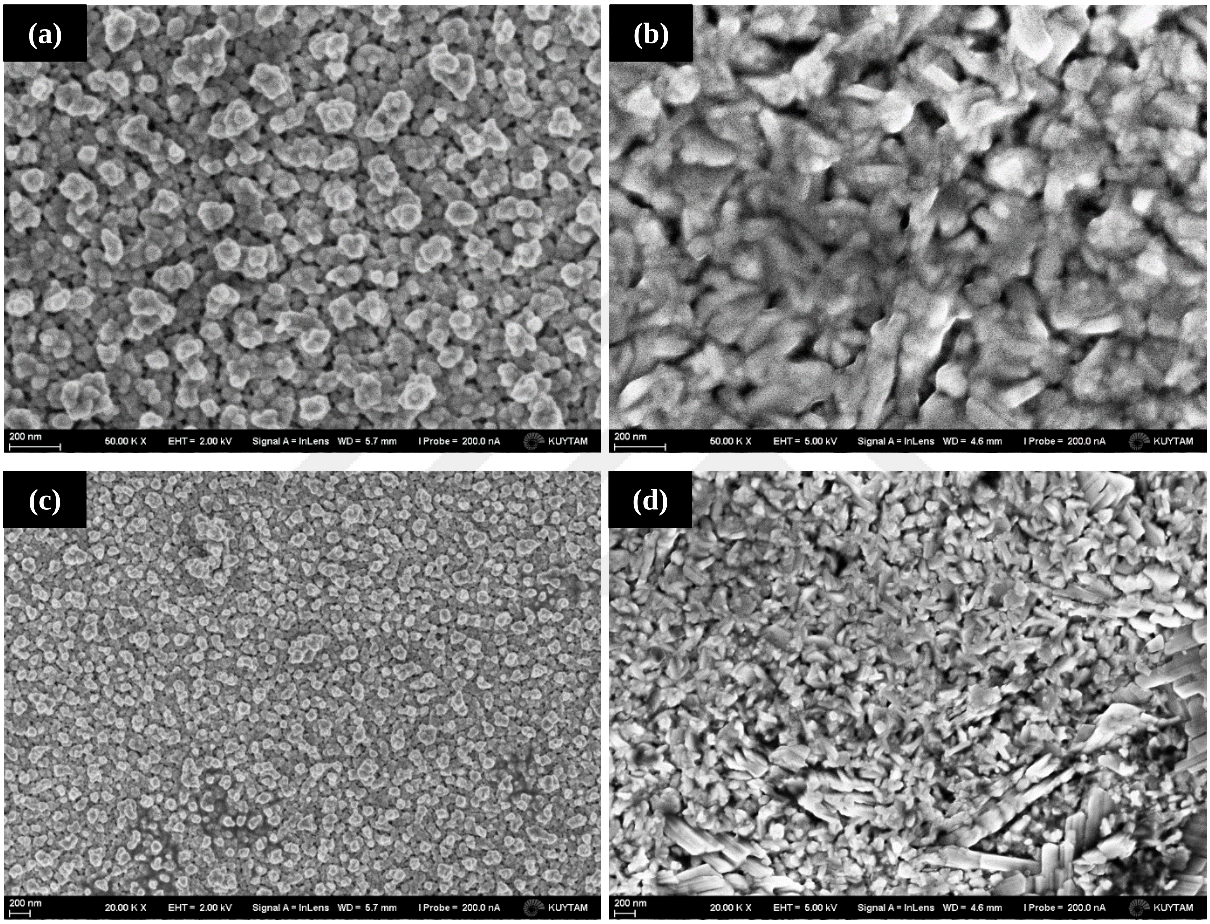

Figure 4.25 SEM images of calcined scCO2_WO3_O2_3h films (a, c) and bare FTO substrate (b, d) in different magnifications.

Difference between the SEM images of the film deposited FTO substrate and bare FTO was significant. Further analysis was done via EDX. Figure 4.26 illustrates the EDX data of the calcined scCO2_WO3_O2_3h film. In this film, ratio of W/Sn was observed to be higher than the film deposited without additional oxygen (scCO2_WO3_3h). Thus, it can be said that, a thicker film can be obtained by adding oxygen.

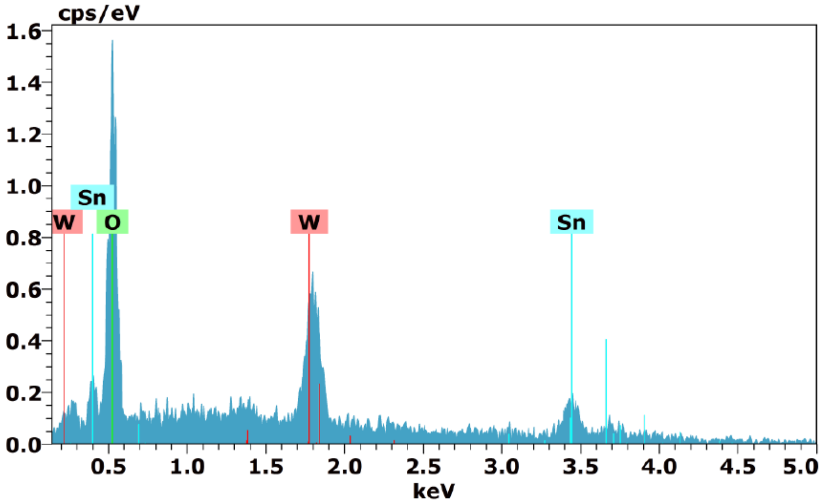

Figure 4.26 EDX spectra of scCO2_WO3_O2_3h film calcined at 500 °C for 1 h.

Thickness measurement from the cross-sectional view via SEM was difficult since the deposited film was highly thin (most probably they were less than 100 nm). However, a cross-sectional view was obtained from the scCO2_WO3_O2_3h film deposited in the presence of O_2 gas. Figure 4.27 demonstrates the SEM images of the WO_3 films from the cross-section.

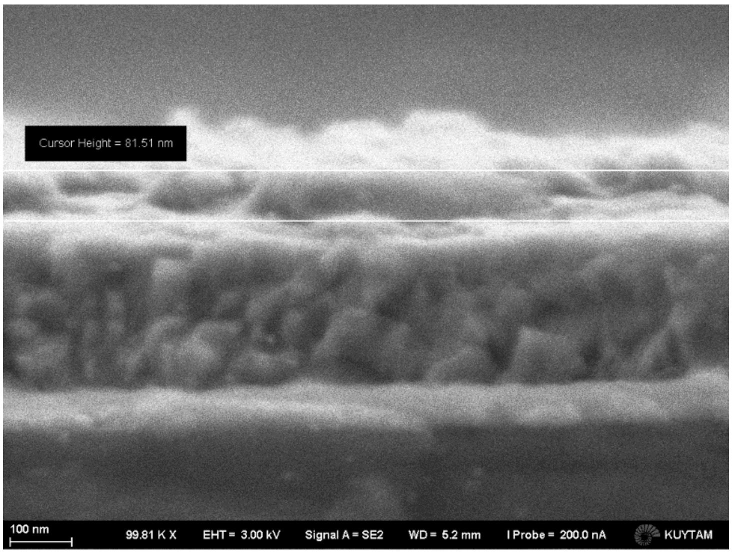

Figure 4.27 SEM image of scCO2_WO3_O2_3h film in cross-sectional view.

Measured thickness of the film was 81.51 nm**.** On the other hand, the cross-sectional view cannot be attained as the actual film thickness since it is not continuous. The reason is for that might be the uncompleted film layer growth or in other words, film growth is initiated but not completed. Thin layer was also observed covering the surface via SEM, but it was hard to distinguish it from the tin coated substrate layer. Hence, SEM is not sufficient enough to attain a thickness of these films, and further determination with TEM is recommended.

Crystal structure of the films was analysed via GIXRD. Figure 4.28 illustrates the X-ray spectra of the WO_3 film produced via supercritical CO_2 deposition and film prepared from the colloidal solution of the WO_3 powder and ethylene glycol.

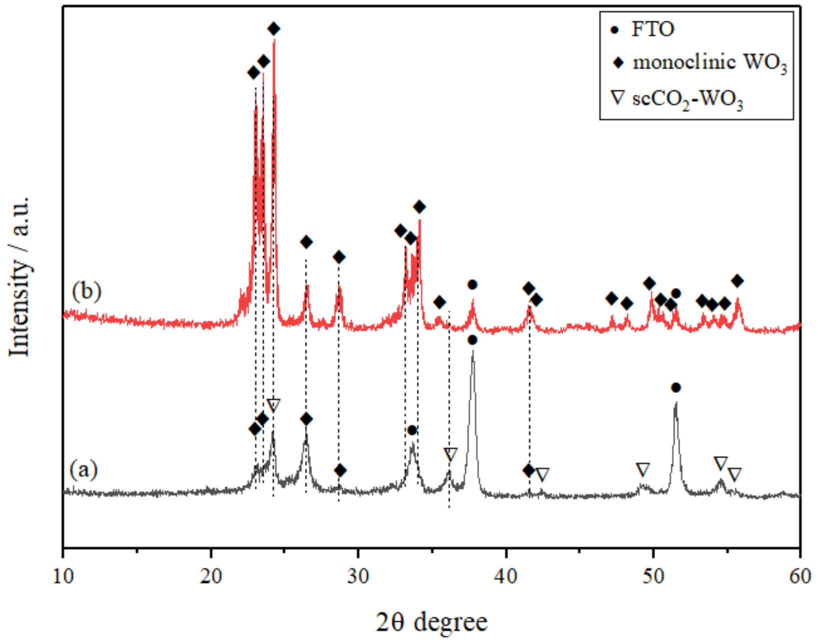

Figure 4.28 X-ray diffraction pattern of WO_3 films (a) scCO2_WO3_O2_3h and (b) HTP_WO3.

Peaks observed around 23.12 and 26.59 ^{0} were as attributed to the monoclinic phase of WO_3. Moreover, small peaks around 23.58, 26.59 and 41.44 ^{o} which began to form also corresponds to the monoclinic structure of WO_3. Two peaks, which were near the corresponding peak of FTO substrate around 33.7 2θ degree, also started to form monoclinic structure. Although it was hard to distinguish them from the FTO, the peak was very broad to be a single FTO peak. The peaks belong to the WO_3 film produced by $scCO_2$ deposition, which were specified with the inverted triangle in Fig. 4.28, could not be attained as the any structure form of tungsten oxides including different states from +6, any form of the tungsten carbide or tungsten hexacarbonyl. Sharp peak around 24.16° seemed to be attained as the orthorhombic phase of the WO_3 with the face orientation of (200), but orthorhombic structure of WO_3 is not a stable phase. This phase is obtained at higher temperatures and when the sample is cooled to room temperature it reverse to the monoclinic phase [51,85]. Thus, this peak was just a little bit shifted towards left 200 orientation of the monoclinic WO_3 structure at 24.38°. Other peaks observed around at 2θ degrees of 36.00, 41.36, 49.20,54.46 and 55.60 can be the peaks initiation of the fully oxidized to W^{+6} state of the WO_3 monoclinic structure. Peaks at 36 and 42.46° can shift to left and peaks at 54.46 and 55.6° can form dissociated peaks of monoclinic phase with further annealing.

4.4.3.3 Material Properties of the Film Deposited with Oxygen Injection

WO_3 film produced by O_2 injection after waiting 1-h was also analysed by Raman spectroscopy. Figure 4.29 demonstrates the Raman spectra of the scCO2_WO3_O2inj_4h films as prepared and annealed. Corresponding peaks of FTO are specified as dashed lines.

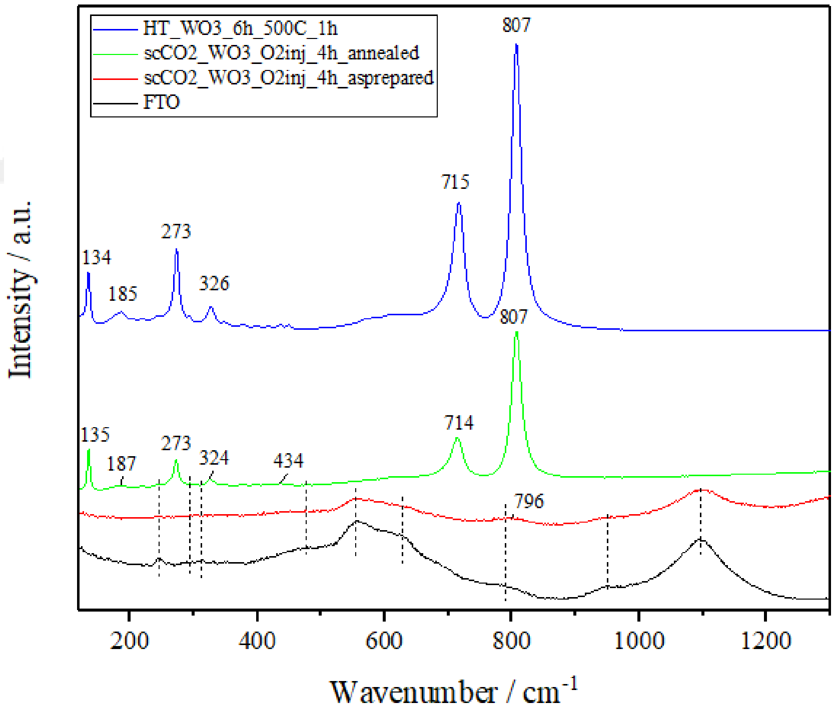

Figure 4.29 Raman spectra of FTO (black line), scCO2_WO3_O2inj_4h films as prepared (red line) and WO_3 film annealed at 500 °C for 1 h (green line), HT_WO3_6h_500C_1h (blue line). Intensities were rescaled for clearer representation.

Observed band at 794 cm^{-1} in the Raman spectra of as-prepared film can be assigned as the W-O stretching vibration [84].

Annealed film shows band features that belong to the monoclinic phase of WO_3 (Bands at 807, 714, 434, 324,273,187 and 135 cm^{-1}). Small peaks around 450 cm^{-1} are also more visible for this sample and they correspond to the lattice modes of WO_3 [86]. When the obtained spectra of the WO_3 film grown directly on FTO via hydrothermal synthesis and film produced by SCD method was compared, corresponding peaks of monoclinic WO_3 were found very similar. Thus, from the Raman data, it can be said that WO_3 production via SCD on FTO was achieved.

For the surface morphology analysis, SEM images were taken from the annealed film. Figure 4.30 shows the SEM images of scCO2_WO3_O2inj_4h and bare FTO at two different magnifications to compare coated surface.

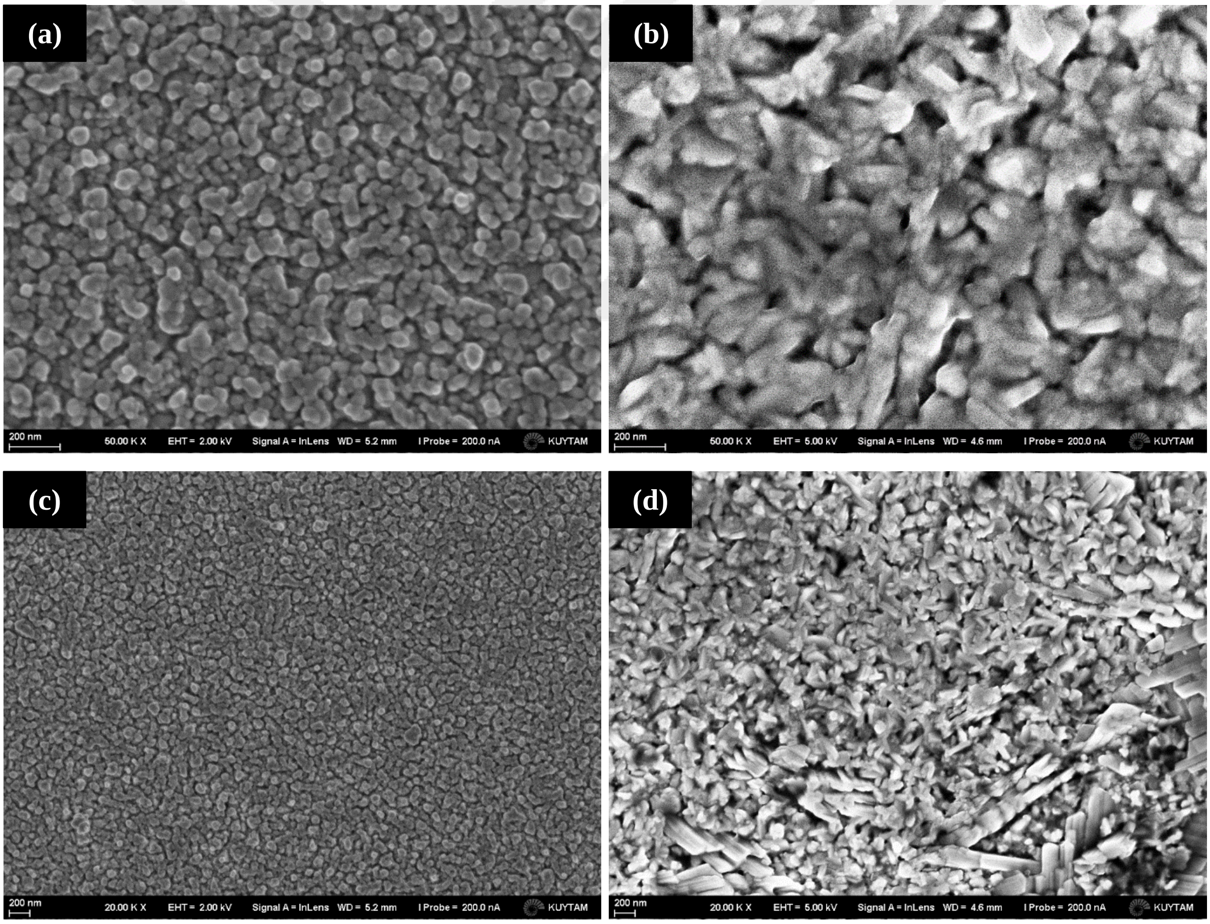

Figure 4.30 SEM images of annealed scCO2_WO3_O2inj_4h film (a, c) and bare FTO substrate (b, d) in different magnifications.

Surface of the coated sample appeared different from the surface of bare FTO. Also, it was highly similar to the WO_3 films scCO2_WO3 _3h and scCO2_WO3_O2_3h. Figure 4.31 demonstrates the results of the EDX data obtained from the surface analysis via SEM.

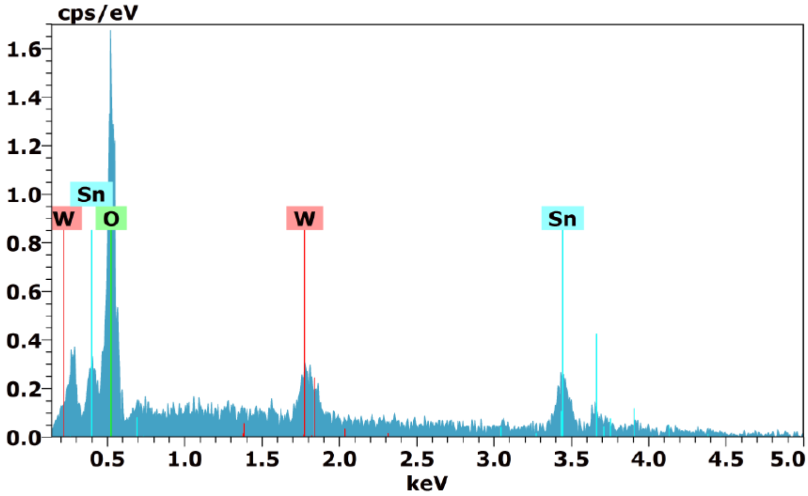

Figure 4.31 EDX spectra of scCO2_WO3_O2inj_4h film calcined at 500 °C for 1 h.

From the EDX data, tungsten existence on the surface of FTO substrate was observed.

For this film, the cross-sectional view was observed in SEM analysis. Figure 4.32 illustrates the SEM image of the scCO2_WO3_O2inj_4h film in cross-section view.

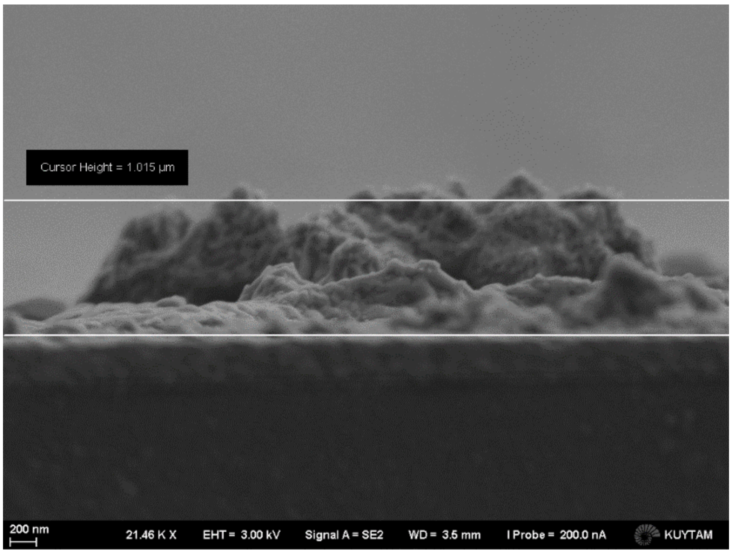

Figure 4.32 SEM image of scCO2_WO3_O2inj_4h film in cross-sectional view.

Thickness was measured as 1.015 µm. This thickness does not indicate the actual thickness, as in the film scCO2_WO3_O2_3h. Thin layer was also observed slightly, but again it was not very selective from the tin coated glass (FTO).

Although the film was very thin, the structural analysis could be performed via GIXRD. Figure 4.33 represents the results of the GIXRD analysis of the WO_3 films produced via supercritical CO_2 method (scCO2_WO3_O2inj_4h**)** and hydrothermal method (HTP_WO3).

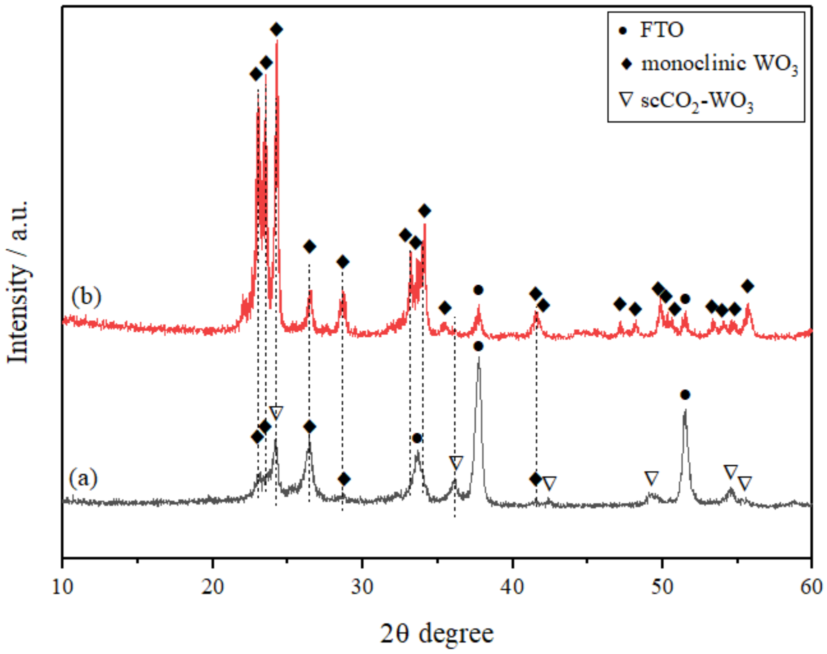

Figure 4.33 X-ray diffraction pattern of WO_3 films (a) scCO2_WO3_O2_3h and (b) HTP_WO3.

Small peaks around 2θ degrees of 23.12,23.58,26.30 and 33.30 correspond to monoclinic structure of WO_3. Peaks belong to FTO substrate were also observed unlike the Raman spectra of this film (see Fig. 4.29).The reason is for that might be correlated to the thickness of the spot where the Raman spectra measurement was performed. This is also can be explained from the SEM image of the sample in cross-sectional view. Peaks at 24.14, 36.12,49.2 and 54.64° specific to our sample could not be attain to any known structure. Most probably these peaks correspond to the tungsten oxide with a different state of tungsten. Moreover, the XRD measurement of the WO_3 film does not match with the result of the Raman spectra exactly but, it can be said that the film was exhibited monoclinic structure.

Further annealing can be a solution for scCO2_WO3_O2_3h film to development of a complete monoclinic structure.

4.4.3.4 Material Properties of the Film Deposited as 2 layers

WO_3 films deposited on WO_3 coated FTO via oxygen injection after the stage reach to the desired deposition temperature was investigated via Raman spectroscopy. Figure 4.34 demonstrates the results of the Raman spectroscopy analysis obtained from the calcined scCO2_WO3_O2inj_4h_2layer WO_3 seed layer on FTO was also prepared by injecting oxygen as same method and by annealing at 500 °C for 1 h. Dashed lines indicated the corresponding peak positions of FTO substrate.

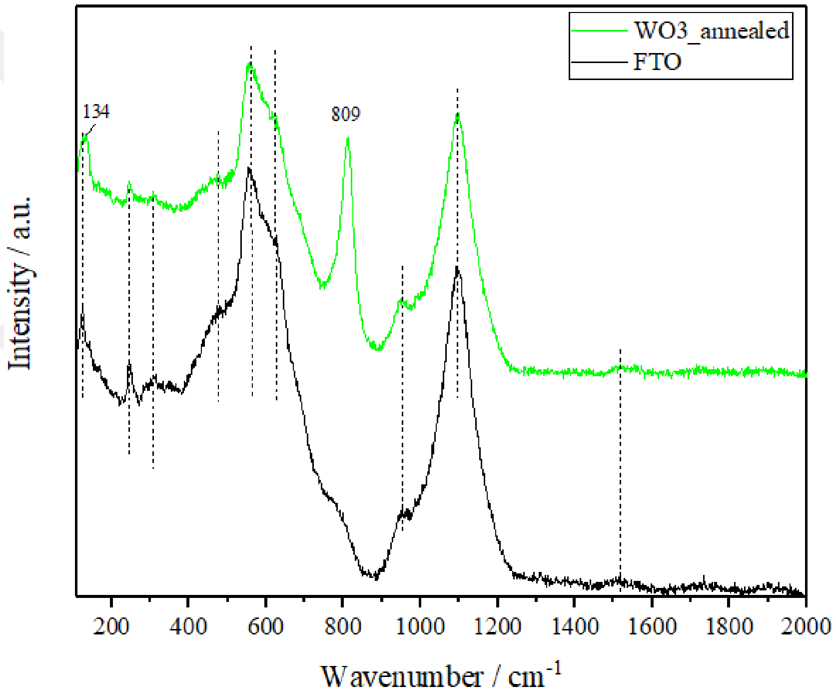

Figure 4.34 Raman spectra of FTO (black line), scCO2_WO3_O2inj_4h_2layer film annealed at 500 °C for 1 h (green line). Intensities were rescaled for clearer representation.

Only two peaks are visible, in the Raman spectra of the WO_3 film prepared on a seed layer. Peak at 809 cm^{-1} corresponds to the stretching modes of O-W-O and peak at 134 cm^{-1} corresponds to the lattice mode bond of monoclinic WO_3.

Surface morphologies of the WO_3 films on FTO substrate were investigated via SEM. Figure 4.35 shows the SEM images of the bare FTO and WO_3 films produced by supercritical CO_2.

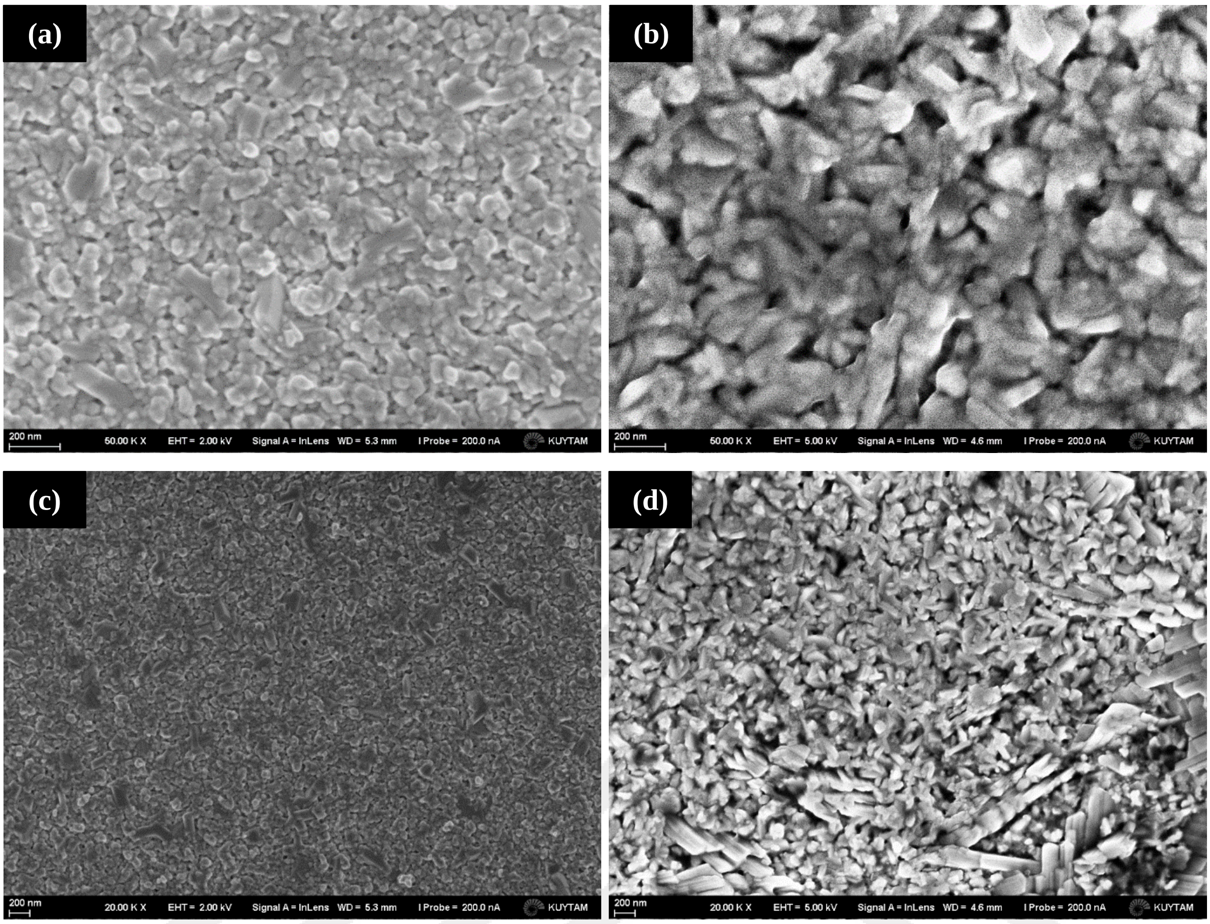

Figure 4.35 SEM images of bare FTO (b, d) and scCO2_WO3_O2inj_4h_2layer film deposited on FTO with post calcination at 500 °C for 1h (a, c).

Different surface morphology was observed from this coating method compared to the previous films deposited via SCD. From the SEM images the surface of the scCO2_WO3_O2inj_4h_2layer film was more alike to the FTO surface. Figure 4.36 shows the EDX analysis of the film was done for the material determination on the surface.

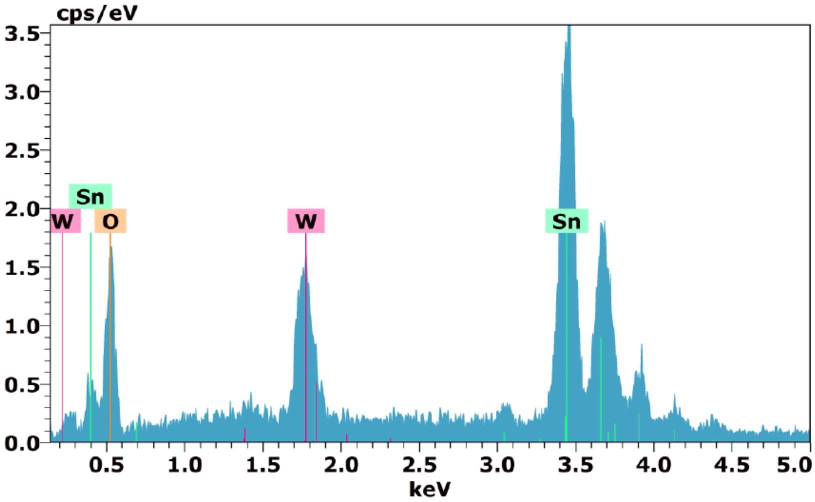

Figure 4. 36 EDX spectra of scCO2_WO3_O2inj_4h_2layer film calcined at 500 °C for 1 h.

Tungsten was present on the surface of the FTO, but the intensity of the peak was much less in comparison to the intensity of the Sn peak from the substrate.

Cross-sectional view was also observed from the film produced by this method via SEM. Figure 4.37 shows the SEM image of the film scCO2_WO3_O2inj_4h_2layer deposited by oxygen injection via supercritical CO_2 deposition technique on WO_3 coated FTO.

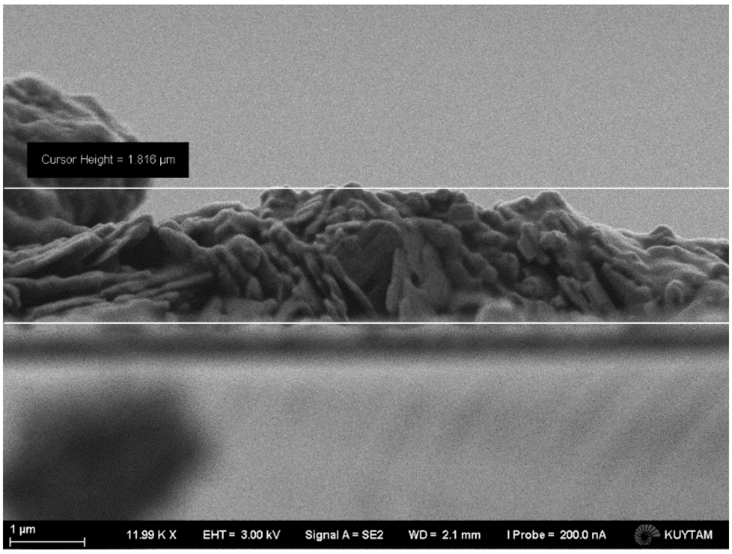

Figure 4.37 SEM image of scCO2_WO3_O2inj_4h film in cross-sectional view.

Thickness was measured as 1.816 µm from the part of the coated surface. It was not the actual thickness from the same reasons of the previous methods.

Further characterization of this deposited WO_3 film on a WO_3 coated FTO was carried out by GIXRD. Figure 4.38 shows the result of the grazing incident X-ray diffractometry annealed WO_3 film at 500 °C for 1 h. To compare the structure of the film produced via supercritical CO_2 deposition, GIXRD spectra of the WO_3 film which was obtained from the colloidal solution of hydrothermally prepared powder was also illustrated in Figure 4.35.

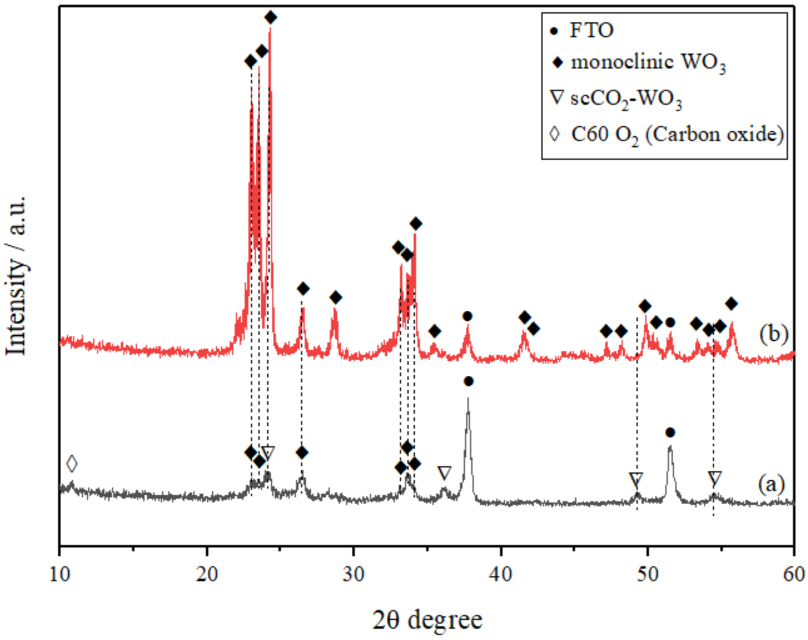

Figure 4.38 X-ray diffraction pattern of WO_3 films (a) scCO2_WO3_O2inj_4h_2layer and (b) HTP_WO3.

From the X-ray diffraction pattern, it was hard to determine a structure for the obtained film since signals coming from the FTO substrate were highly intense compared to the coated film. The peak at 10.74° can be ascribed as the Carbon oxide peak of C60 material. The reason of this small peak might be carbon residue left from the hexacarbonyl precursor. Peaks at 23.1 and 23.5° correspond to the monoclinic phase of WO_3. In addition to that, three peaks between 33-35° are the indicator of the monoclinic structure, but they are not completely dissociated as in the X-ray pattern of the hydrothermally prepared WO_3 film. Peak belong to our sample around 24.1 also little bit shifted compared to the monoclinic 200 crystal plane. As in the spectra of the WO_3 films produced via SCD, peaks around 36.14, 49.20 and 54.52° could not be attained to any structure of tungsten oxides or tungsten carbides. These peaks might be the sign of any tungsten oxide with a different tungsten state from the fully oxidized state of W^{+6}.

In order to compare SCD methods that were used, XRD patterns of all WO_3 films prepared via SCD with the addition of oxygen were summarized in Figure 4.39. XRD pattern could not be obtained from the film deposited in the presence of oxygen (scCO2_WO3_3h). The reason was for that might be the thickness of the film since it was very thin.

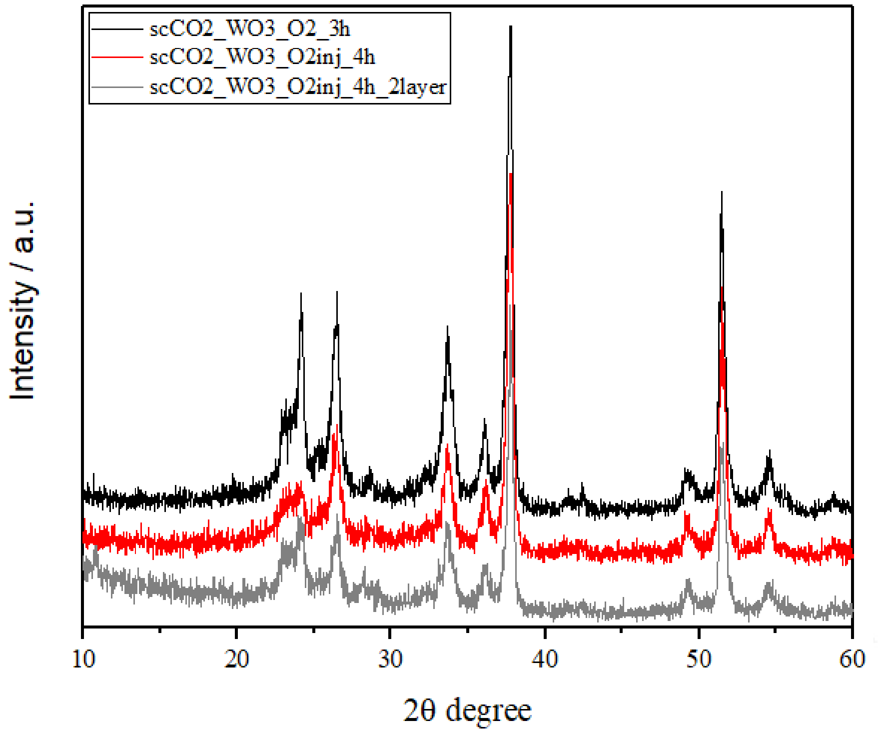

Figure 4.39 X-ray diffraction patterns of WO3 films produced via SCD: scCO2_WO3_O2_3h (black line), scCO2_WO3_O2inj_4h (red line) and scCO2_WO3_O2inj_4h_2layer (grey line).

The addition of O_2 gas had affect the thickness of a film since X-ray diffraction pattern could not be obtained from the film produced only in the presence of air while it was observed from the other films. Moreover, from the Fig. 4.39 it was obvious that the step in which the O_2 introduced during deposition and amount of the O_2 have also impact on a structure of a film. Also, corresponding peaks of monoclinic WO_3 between 22-25° are more dissociated in sample scCO2_WO3_O2_3h but also intensities of the FTO substrate peaks are slightly higher in this sample.

4.4.4 Photoelectrochemistry

Cyclic voltammetry measurements were performed under dark and under illumination in 1 M H_2SO_4 and in 1 M H_2SO_4 with 10%vol. CH_3OH from the annealed WO_3 films produced via SCD. Figure 4.40 illustrates the current density versus potential plot of the WO_3 film in 1 M H_2SO_4 with and without methanol.

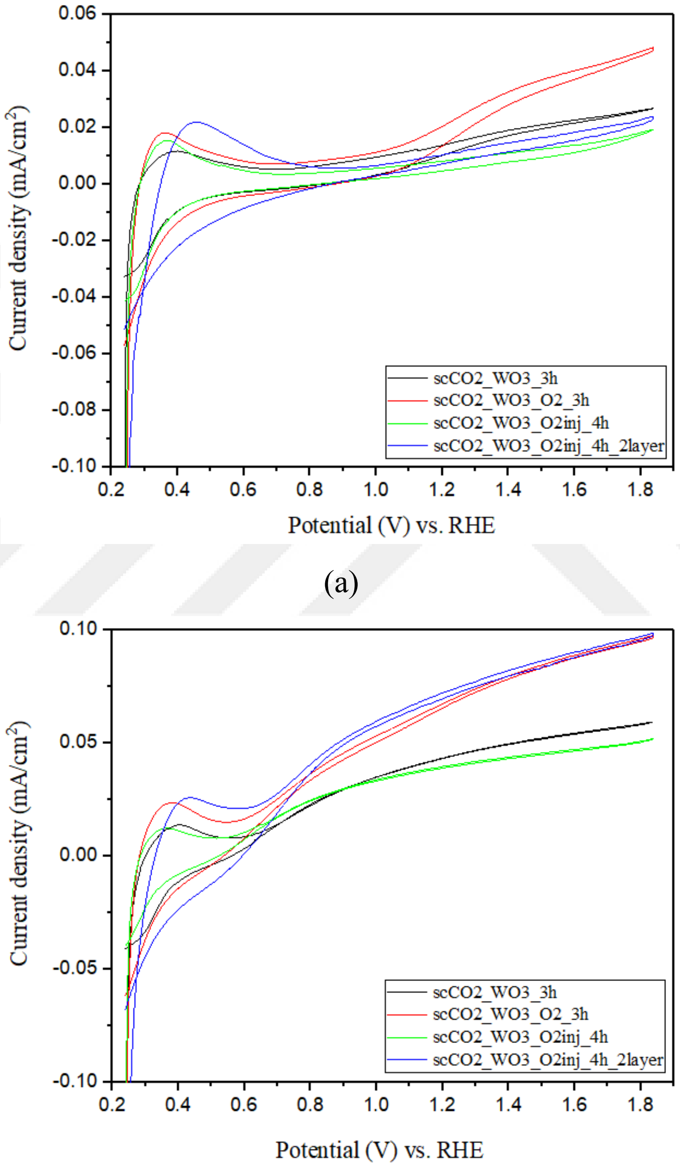

(a)

(b)

Figure 4.40 Current density (mA/cm^2) vs. potential with respect to RHE (V) obtained from the PEC test of the calcined WO_3 films produced via SCD: scCO2_WO3_3h (black line), scCO2_WO3_O2_3h (red line), scCO2_WO3_O2inj_4h (yellow line) and scCO2_WO3_O2inj_4h_2layer (blue line) in (a) 1M H_2SO_4 and (b) in 1 M H_2SO_4 / 10%vol. CH_3OH.

Onset potentials were measured from the WO_3 films in 1 M H_2SO_4 as follows: 0.7, 0.7, 0.71 and 0.9 V (vs. RHE) for the films scCO2_WO3_3h, scCO2_WO3_O2_3h, scCO2_WO3_O2inj_4h and scCO2_WO3_O2inj_4h_2layer respectively. The best photocurrent density at 1.23 V was obtained from the film scCO2_WO3_O2_3h with a value of 0.0225 mA/cm^2. Photocurrent densities measured at 1.23 V from the WO_3 films scCO2_WO3_3h and scCO2_WO3_O2inj_4h_2layer were observed very close to each other with current densities of 0.0146 and 0.0110 mA/cm^2. The lowest photocurrent density was obtained as 0.0085 mA/cm^2 from the film scCO2_WO3_O2inj_4h. The main reason of the value was quite low due to the thickness of the sample. Absorbance of the light hitting on the surface of the WO_3 photoanode was less since the films were very thin. Thus, it would not be right to compare these values with the current densities obtained from the hydrothermal synthesis which is a conventional method. The small peak observed between the potentials 1.3-1.5 V during the photoelectrochemical characterization in 1 M H_2SO_4 from the films scCO2_WO3_O2_3h and scCO2_WO3_3h. This peak was the indicator of that the something was oxidized.

By the addition of the hole scavenger (methanol), the photocurrent onset potentials were lowered to the 0.57, 0.55, 0.53 and 0.58 V for the films scCO2_WO3_3h, scCO2_WO3_O2_3h, scCO2_WO3_O2inj_4h and scCO2_WO3_O2inj_4h_2layer respectively. The photocurrent density at 1.23 V of the film scCO2_WO3_O2inj_4h_2layer increased from 0.0110 to 0.0737 mA/cm^2 since the hole scavenger prevented the recombination of the created electron and hole pairs. Then, it was followed by the film scCO2_WO3_O2_3h with a current density of 0.0693 mA/cm^2. Current densities of 0.044 and 0.0403 mA/cm^2 were obtained from the WO_3 films scCO2_WO3_3h and scCO2_WO3_O2inj_4h.

When the obtained current densities measured in 1 M H_2SO_4 with and without addition of hole scavenger were compared, differences were observed in the increase of the photocurrent. The reason is for that might the better interaction of the scavenger with the surface of the sample scCO2_WO3_O2inj_4h_2layer.

Chapter 5

CONCLUSION AND FUTURE WORK

In this study, supercritical fluid deposition was presented as a new technique for the tungsten oxide film production to use in the photoelectrochemical water splitting. Hydrothermal synthesis of WO_3 was also studied to make comparison between the new developed SCD method and conventional technique.

In the first part of the study, WO_3 films were produced by hydrothermal technique to investigate the structure and photoelectrochemical characterization. Two types of deposition methods were applied: direct growth on FTO substrate and drop cast of the particulate solution prepared from hydrothermally synthesized WO_3 powder and ethylene glycol on FTO. Post calcination effect on particle size, structure and photoactivity was investigated. Annealing at 500 °C for 1 h was found as the best condition for the better photoactivity. Fully developed monoclinic structure were also obtained for the heat treatment condition of 500 °C for 1 h which was confirmed via XRD. Film growth directly on FTO was studied by carrying out the hydrothermal reaction at constant temperature for different periods (1 h, 3 h, 4 h, 5 h, 6 h, and 10 h). Deposition time effected on the morphology was observed from the SEM images of the films. It was observed that the 1-hour reaction time was not enough for the formation of complete nanostructure. Increasing reaction time was not resulted in higher thicknesses for each case because of the pealing from the films due weak adhesion of films on the surface of FTO. This situation was observed from the films deposited for 5 h and 10 h. Photoelectrochemical characterization were studied for each film. The best photocurrent density was obtained from the WO_3 film deposited for a 6 h. The on-set potential and current density at 1.23 V were measured as 0.62 V vs. RHE and 0.75 mA/cm^2. Effect of hole scavenger in the photoelectrochemical measurements was also investigated. The on-set potential was lowered to 0.51 V and activity was increased to 1.48 mA/cm^2. Front and back side measurements were performed for this sample. Better transport properties were observed from the back-side illumination because of the thickness was very thick. To overcome the transport limitations due to thickness, thinner films were obtained by preparing colloidal solution of WO_3 powder. Although, increase in the photoactivity of the film was not observed measurements in 1 M H_2SO_4, it was increased by 48.36% in 1 M H_2SO_4 / CH_3OH.

In the second part of the study, production of WO_3 film on FTO substrate by SCD technique was studied. $W(CO)_6$ was used as tungsten source due the ability of dissolution in $scCO_2$. To determine the precursor amount, solubility of the $W(CO)_6$ was examined. Solubility of the precursor was found as 1.97×10^{-3} at 35 °C and 4.1×10^{-3} at 45 °C. The solubility of it was also tested without using a stirrer. Complete dissolution was obtained in the end of 2.5 h when the precursor loading was 0.4 wt. % and temperature was 80 °C. For the metal oxide film production, a cold-wall reactor was designed where the film growth occurred on a heated substrate. Depositions were performed at 8.27 MPa CO_2 and a heating stage temperature of 300 °C. 4 different methods were applied with no additional oxygen (O_2) gas and with addition of O_2 in different steps of the deposition. Investigation of the surface of the films via SEM and EDX showed that the coating on FTO substrate were achieved. The cross-sectional view of SEM images revealed that the films very thin (<100 nm) and the surface of the films consist of the incomplete growth. Structure analysis of the films via XRD showed the monoclinic structure. For the additional peaks, further investigation was needed to be done. Photo activity was observed from all films although the obtained current densities were very low due to the thickness of the films. The best photocurrent density was obtained as 0.0225 mA/cm^2 at 1.23 V in the solution of 1 M H_2SO_4 from the film produced with the addition of oxygen before starting the deposition. In the solution with hole scavenger, the highest activity was observed from the film deposited on a seed layer with a current density of 0.0737 mA/cm^2.

The photoactivity of the films produced by SCD could be improved by the deposition of thicker films. This could be done by deposition of the films at higher temperatures. Fully oxidized state of the tungsten (+6) could be achieved by longer deposition time.

Within the lights of all results, SCD method can be an alternative for WO_3 photoelectrode production since the films showed activity even though the films were very thin. This method also can offer a different perspective to those interested in photoelectrode production as it is an unprecedented method in this area.

BIBLIOGRAPHY

[1] BP Statistical Review of World Energy 2017, (n.d.) 52.
[2] R.S. of Chemistry, Energy, (2014). http://www.rsc.org/campaigning-outreach/global-challenges/energy/ (accessed July 4, 2018).
[3] M.G. Walter, E.L. Warren, J.R. McKone, S.W. Boettcher, Q. Mi, E.A. Santori, N.S. Lewis, Solar Water Splitting Cells, Chem. Rev. 110 (2010) 6446–6473. doi:10.1021/cr1002326.
[4] R. van de Krol, M. Grätzel, eds., Photoelectrochemical Hydrogen Production, Springer US, 2012. //www.springer.com/gp/book/9781461413790 (accessed July 4, 2018).
[5] A. Kudo, Y. Miseki, Heterogeneous photocatalyst materials for water splitting, Chem. Soc. Rev. 38 (2008) 253–278. doi:10.1039/B800489G.
[6] X. Li, J. Yu, J. Low, Y. Fang, J. Xiao, X. Chen, Engineering heterogeneous semiconductors for solar water splitting, J. Mater. Chem. A. 3 (2015) 2485–2534. doi:10.1039/C4TA04461D.
[7] I.C. Man, H.-Y. Su, F. Calle-Vallejo, H.A. Hansen, J.I. Martínez, N.G. Inoglu, J. Kitchin, T.F. Jaramillo, J.K. Nørskov, J. Rossmeisl, Universality in Oxygen Evolution Electrocatalysis on Oxide Surfaces, ChemCatChem. 3 (n.d.) 1159–1165. doi:10.1002/cctc.201000397.
[8] A. Fujishima, K. Honda, Electrochemical Photolysis of Water at a Semiconductor Electrode, Nature. 238 (1972) 37–38. doi:10.1038/238037a0.
[9] S.S. Kalanur, Y.J. Hwang, S.Y. Chae, O.S. Joo, Facile growth of aligned WO3 nanorods on FTO substrate for enhanced photoanodic water oxidation activity, J. Mater. Chem. A. 1 (2013) 3479–3488. doi:10.1039/C3TA01175E.
[10] X. Liu, F. Wang, Q. Wang, Nanostructure-based WO3 photoanodes for photoelectrochemical water splitting, Phys. Chem. Chem. Phys. PCCP. 14 (2012) 7894–7911. doi:10.1039/c2cp40976c.
[11] G. Hodes, D. Cahen, J. Manassen, Tungsten trioxide as a photoanode for a photoelectrochemical cell (PEC), Nature. 260 (1976) 312–313. doi:10.1038/260312a0.
[12] C. Santato, M. Ulmann, J. Augustynski, Photoelectrochemical Properties of Nanostructured Tungsten Trioxide Films, J. Phys. Chem. B. 105 (2001) 936–940. doi:10.1021/jp002232q.
[13] Crystallographically Oriented Mesoporous WO3 Films: Synthesis, Characterization, and Applications - Journal of the American Chemical Society (ACS Publications), (n.d.). https://pubs.acs.org/doi/abs/10.1021/ja011315x (accessed July 4, 2018).
[14] B. Yang, Y. Zhang, E. Drabarek, P.R.F. Barnes, V. Luca, Enhanced Photoelectrochemical Activity of Sol−Gel Tungsten Trioxide Films through Textural Control, Chem. Mater. 19 (2007) 5664–5672. doi:10.1021/cm071603d.
[15] B. Yang, P.R.F. Barnes, W. Bertram, V. Luca, Strong photoresponse of nanostructured tungsten trioxide films prepared via a sol–gel route, J. Mater. Chem. 17 (2007) 2722–2729. doi:10.1039/B702097J.
[16] M. Yagi, S. Maruyama, K. Sone, K. Nagai, T. Norimatsu, Preparation and photoelectrocatalytic activity of a nano-structured WO3 platelet film, J. Solid State Chem. 181 (2008) 175–182. doi:10.1016/j.jssc.2007.11.018.

Bibliography

[17] J.K. Kim, K. Shin, S.M. Cho, T.-W. Lee, J.H. Park, Synthesis of transparent mesoporous tungsten trioxide films with enhanced photoelectrochemical response: application to unassisted solar water splitting, Energy Environ. Sci. 4 (2011) 1465–1470. doi:10.1039/C0EE00469C.

[18] P.-T. Hsiao, L.-C. Chen, T.-L. Li, H. Teng, Vapor treatment of nanocrystalline WO3 photoanodes for enhanced photoelectrochemical performance in the decomposition of water, J. Mater. Chem. 21 (2011) 19402–19409. doi:10.1039/C1JM14785D.

[19] H. Wang, T. Lindgren, J. He, A. Hagfeldt, S.-E. Lindquist, Photolelectrochemistry of Nanostructured WO3 Thin Film Electrodes for Water Oxidation: Mechanism of Electron Transport, J. Phys. Chem. B. 104 (2000) 5686–5696. doi:10.1021/jp0002751.

[20] N.R. de Tacconi, C.R. Chenthamarakshan, G. Yogeeswaran, A. Watcharenwong, R.S. de Zoysa, N.A. Basit, K. Rajeshwar, Nanoporous TiO2 and WO3 Films by Anodization of Titanium and Tungsten Substrates: Influence of Process Variables on Morphology and Photoelectrochemical Response, J. Phys. Chem. B. 110 (2006) 25347–25355. doi:10.1021/jp064527v.

[21] W. Li, J. Li, X. Wang, S. Luo, J. Xiao, Q. Chen, Visible light photoelectrochemical responsiveness of self-organized nanoporous WO3 films, Electrochimica Acta. 56 (2010) 620–625. doi:10.1016/j.electacta.2010.06.025.

[22] J.Z. Ou, R.A. Rani, S. Balendhran, A.S. Zoolfakar, M.R. Field, S. Zhuiykov, A.P. O'Mullane, K. Kalantar-zadeh, Anodic formation of a thick three-dimensional nanoporous WO3 film and its photocatalytic property, Electrochem. Commun. 27 (2013) 128–132. doi:10.1016/j.elecom.2012.11.009.

[23] H. Qi, J. Wolfe, D. Wang, H.J. Fan, D. Fichou, Z. Chen, Triple-layered nanostructured WO $_3$ photoanodes with enhanced photocurrent generation and superior stability for photoelectrochemical solar energy conversion, Nanoscale. 6 (2014) 13457–13462. doi:10.1039/C4NR03982C.

[24] J. Su, X. Feng, J.D. Sloppy, L. Guo, C.A. Grimes, Vertically Aligned WO3 Nanowire Arrays Grown Directly on Transparent Conducting Oxide Coated Glass: Synthesis and Photoelectrochemical Properties, Nano Lett. 11 (2011) 203–208. doi:10.1021/nl1034573.

[25] J. Zhang, P. Zhang, T. Wang, J. Gong, Monoclinic WO3 nanomultilayers with preferentially exposed (002) facets for photoelectrochemical water splitting, Nano Energy. 11 (2015) 189–195. doi:10.1016/j.nanoen.2014.10.021.

[26] S.J. Hong, H. Jun, P.H. Borse, J.S. Lee, Size effects of WO3 nanocrystals for photooxidation of water in particulate suspension and photoelectrochemical film systems, Int. J. Hydrog. Energy. 34 (2009) 3234–3242. doi:10.1016/j.ijhydene.2009.02.006.

[27] F. Amano, M. Tian, G. Wu, B. Ohtani, A. Chen, Facile Preparation of Platelike Tungsten Oxide Thin Film Electrodes with High Photoelectrode Activity, ACS Appl. Mater. Interfaces. 3 (2011) 4047–4052. doi:10.1021/am200897n.

[28] F. Amano, D. Li, B. Ohtani, Photoelectrochemical Property of Tungsten Oxide Films of Vertically Aligned Flakes for Visible-Light-Induced Water Oxidation, J. Electrochem. Soc. 158 (2011) K42–K46. doi:10.1149/1.3525624.

[29] Z. Jiao, J. Wang, L. Ke, X.W. Sun, H.V. Demir, Morphology-Tailored Synthesis of Tungsten Trioxide (Hydrate) Thin Films and Their Photocatalytic Properties, ACS Appl. Mater. Interfaces. 3 (2011) 229–236. doi:10.1021/am100875z.

[30] D.-D. Qin, C.-L. Tao, S. A. Friesen, T.-H. Wang, O. K. Varghese, N.-Z. Bao, Z.-Y. Yang, T. E. Mallouk, C. A. Grimes, Dense layers of vertically oriented WO 3 crystals as anodes for photoelectrochemical water oxidation, Chem. Commun. 48 (2012) 729–731. doi:10.1039/C1CC15691H.

[31] X. Feng, Y. Chen, Z. Qin, M. Wang, L. Guo, Facile Fabrication of Sandwich Structured WO3 Nanoplate Arrays for Efficient Photoelectrochemical Water Splitting, ACS Appl. Mater. Interfaces. 8 (2016) 18089–18096. doi:10.1021/acsami.6b04887.

[32] W.L. Kwong, H. Qiu, A. Nakaruk, P. Koshy, C.C. Sorrell, Photoelectrochemical Properties of WO3 Thin Films Prepared by Electrodeposition, Energy Procedia. 34 (2013) 617–626. doi:10.1016/j.egypro.2013.06.793.

[33] J.C. Hill, K.-S. Choi, Effect of Electrolytes on the Selectivity and Stability of n-type WO3 Photoelectrodes for Use in Solar Water Oxidation, J. Phys. Chem. C. 116 (2012) 7612–7620. doi:10.1021/jp209909b.

[34] R. Liu, Y. Lin, L.-Y. Chou, S.W. Sheehan, W. He, F. Zhang, H.J.M. Hou, D. Wang, Water Splitting by Tungsten Oxide Prepared by Atomic Layer Deposition and Decorated with an Oxygen-Evolving Catalyst, Angew. Chem. 123 (n.d.) 519–522. doi:10.1002/ange.201004801.

[35] Y. Sun, C.J. Murphy, K.R. Reyes-Gil, E.A. Reyes-Garcia, J.M. Thornton, N.A. Morris, D. Raftery, Photoelectrochemical and structural characterization of carbon-doped WO3 films prepared via spray pyrolysis, Int. J. Hydrog. Energy. 34 (2009) 8476–8484. doi:10.1016/j.ijhydene.2009.08.015.

[36] P.M. Rao, I.S. Cho, X. Zheng, Flame synthesis of WO3 nanotubes and nanowires for efficient photoelectrochemical water-splitting, Proc. Combust. Inst. 34 (2013) 2187–2195. doi:10.1016/j.proci.2012.06.122.

[37] V. Chakrapani, J. Thangala, M.K. Sunkara, WO3 and W2N nanowire arrays for photoelectrochemical hydrogen production, Int. J. Hydrog. Energy. 34 (2009) 9050–9059. doi:10.1016/j.ijhydene.2009.09.031.

[38] X. Zhang, X. Lu, Y. Shen, J. Han, L. Yuan, L. Gong, Z. Xu, X. Bai, M. Wei, Y. Tong, Y. Gao, J. Chen, J. Zhou, Z.L. Wang, Three-dimensional WO3 nanostructures on carbon paper: photoelectrochemical property and visible light driven photocatalysis, Chem. Commun. 47 (2011) 5804–5806. doi:10.1039/C1CC10389J.

[39] J. Yang, W. Li, J. Li, D. Sun, Q. Chen, Hydrothermal synthesis and photoelectrochemical properties of vertically aligned tungsten trioxide (hydrate) plate-like arrays fabricated directly on FTO substrates, J. Mater. Chem. 22 (2012) 17744–17752. doi:10.1039/C2JM33199C.

[40] Y. Zong, J.J. Watkins, Deposition of Copper by the H2-Assisted Reduction of Cu(tmod)2 in Supercritical Carbon Dioxide: Kinetics and Reaction Mechanism, Chem. Mater. 17 (2005) 560–565. doi:10.1021/cm048665d.

[41] E.T. Hunde, J.J. Watkins, Reactive Deposition of Cobalt and Nickel Films from Their Metallocenes in Supercritical Carbon Dioxide Solution, Chem. Mater. 16 (2004) 498–503. doi:10.1021/cm034433n.

[42] E. Kondoh, H. Kato, Characteristics of copper deposition in a supercritical CO2 fluid, Microelectron. Eng. 64 (2002) 495–499. doi:10.1016/S0167-9317(02)00826-2.

[43] A. Cabañas, D.P. Long, J.J. Watkins, Deposition of Gold Films and Nanostructures from Supercritical Carbon Dioxide, Chem. Mater. 16 (2004) 2028–2033. doi:10.1021/cm034739u.

[44] Y. Zhao, K. Jung, Y. Shimoyama, Y. Shimogaki, T. Momose, Conformal Bismuth Titanate Formation Using Supercritical Fluid Deposition, ECS J. Solid State Sci. Technol. 6 (2017) P483–P488. doi:10.1149/2.0011708jss.

[45] A. O'Nei, J.J. Watkins, Reactive Deposition of Conformal Metal Oxide Films from Supercritical Carbon Dioxide, Chem. Mater. 19 (2007) 5460–5466. doi:10.1021/cm070288s.

[46] T. Gougousi, D. Barua, E.D. Young, G.N. Parsons, Metal Oxide Thin Films Deposited from Metal Organic Precursors in Supercritical CO2 Solutions, Chem. Mater. 17 (2005) 5093–5100. doi:10.1021/cm0510965.
[47] Y. Zhao, K. Jung, T. Momose, Y. Shimogaki, Smooth and Conformal TiO2 Thin-Film Formation Using Supercritical Fluid Deposition, ECS J. Solid State Sci. Technol. 2 (2013) N191–N195. doi:10.1149/2.003311jss.
[48] C. Erkey, Preparation of metallic supported nanoparticles and films using supercritical fluid deposition, J. Supercrit. Fluids. 47 (2009) 517–522. doi:10.1016/j.supflu.2008.10.019.
[49] Supercritical Fluids and Organometallic Compounds, Volume 1 - 1st Edition, (n.d.). https://www.elsevier.com/books/supercritical-fluids-and-organometallic-compounds/erkey/978-0-08-045329-3 (accessed July 10, 2018).
[50] P.M. Woodward, A.W. Sleight, T. Vogt, Ferroelectric Tungsten Trioxide, J. Solid State Chem. 131 (1997) 9–17. doi:10.1006/jssc.1997.7268.
[51] Nanostructured Tungsten Oxide – Properties, Synthesis, and Applications - Zheng - 2011 - Advanced Functional Materials - Wiley Online Library, (n.d.). https://onlinelibrary.wiley.com/doi/abs/10.1002/adfm.201002477 (accessed July 9, 2018).
[52] W. Li, J. Li, X. Wang, J. Ma, Q. Chen, Photoelectrochemical and physical properties of WO3 films obtained by the polymeric precursor method, Int. J. Hydrog. Energy. 35 (2010) 13137–13145. doi:10.1016/j.ijhydene.2010.09.011.
[53] A.C. Jones, M.L. Hitchman, Chemical Vapour Deposition: Precursors, Processes and Applications, Royal Society of Chemistry, 2009.
[54] G.A. Niklasson, C.G. Granqvist, Electrochromics for smart windows: thin films of tungsten oxide and nickel oxide, and devices based on these, J. Mater. Chem. 17 (2006) 127–156. doi:10.1039/B612174H.
[55] K. Byrappa, T. Adschiri, Hydrothermal technology for nanotechnology, Prog. Cryst. Growth Charact. Mater. 53 (2007) 117–166. doi:10.1016/j.pcrysgrow.2007.04.001.
[56] D.-D. Qin, C.-L. Tao, S. In, Z.-Y. Yang, T.E. Mallouk, N. Bao, C.A. Grimes, Facile Solvothermal Method for Fabricating Arrays of Vertically Oriented α-Fe2O3 Nanowires and Their Application in Photoelectrochemical Water Oxidation, Energy Fuels. 25 (2011) 5257–5263. doi:10.1021/ef201367q.
[57] M. Majimel, S. Marre, E. Garrido, C. Aymonier, Supercritical Fluid Chemical Deposition as an Alternative Process to CVD for the Surface Modification of Materials, Chem. Vap. Depos. 17 (n.d.) 342–352. doi:10.1002/cvde.201106921.
[58] R.B. Gupta, J.-J. Shim, Solubility in Supercritical Carbon Dioxide, CRC Press, 2006.
[59] L. Laboureur, M. Ollero, D. Touboul, Lipidomics by Supercritical Fluid Chromatography, Int. J. Mol. Sci. 16 (2015) 13868–13884. doi:10.3390/ijms160613868.
[60] N.G. Smart, T. Carleson, T. Kast, A.A. Clifford, M.D. Burford, C.M. Wai, Solubility of chelating agents and metal-containing compounds in supercritical fluid carbon dioxide, Talanta. 44 (1997) 137–150. doi:10.1016/S0039-9140(96)02008-5.
[61] M. Türk, M. Crone, G. Upper, Effect of gas pressure on the phase behaviour of organometallic compounds, J. Supercrit. Fluids. 58 (2011) 1–6. doi:10.1016/j.supflu.2011.05.016.
[62] Y. Zhang, D. Kang, C. Saquing, M. Aindow, C. Erkey, Supported Platinum Nanoparticles by Supercritical Deposition, Ind. Eng. Chem. Res. 44 (2005) 4161–4164. doi:10.1021/ie050345w.
[63] J.J. Watkins, J.M. Blackburn, T.J. McCarthy, Chemical Fluid Deposition: Reactive Deposition of Platinum Metal from Carbon Dioxide Solution, Chem. Mater. 11 (1999) 213–215. doi:10.1021/cm981016f.

[64] R.U. Kirss, L. Meda, Chemical vapor deposition of tungsten oxide, Appl. Organomet. Chem. 12 (1998) 155–160. doi:10.1002/(SICI)1099-0739(199803)12:3<155::AID-AOC688>3.0.CO;2-Z.

[65] Tungsten hexacarbonyl 472956, Sigma-Aldrich. (n.d.). https://www.sigmaaldrich.com/catalog/product/aldrich/472956 (accessed July 11, 2018).

[66] M. McHugh, V. Krukonis, Supercritical Fluid Extraction: Principles and Practice, Elsevier, 2013.

[67] Q. Peng, D. Hojo, K.J. Park, G.N. Parsons, Low temperature metal oxide film deposition and reaction kinetics in supercritical carbon dioxide, Thin Solid Films. 516 (2008) 4997–5003. doi:10.1016/j.tsf.2007.10.057.

[68] C.F. Karanikas, Supercritical Fluid Deposition Of Thin Metal Films: Kinetics, Mechanics And Applications, (n.d.) 230.

[69] X. Shan, D.P. Schmidt, J.J. Watkins, Study of natural convection in supercritical CO2 cold wall reactors: Simulations and experiments, J. Supercrit. Fluids. 40 (2007) 84–92. doi:10.1016/j.supflu.2006.03.023.

[70] A. O'Nei, J.J. Watkins, Reactive Deposition of Conformal Ruthenium Films from Supercritical Carbon Dioxide, Chem. Mater. 18 (2006) 5652–5658. doi:10.1021/cm060142d.

[71] I. Székely, G. Kovács, L. Baia, V. Danciu, Z. Pap, Synthesis of Shape-Tailored WO3 Micro-/Nanocrystals and the Photocatalytic Activity of WO3/TiO2 Composites, Materials. 9 (2016). doi:10.3390/ma9040258.

[72] P. Scherrer, Bestimmung der Größe und der inneren Struktur von Kolloidteilchen mittels Röntgenstrahlen, Nachrichten Von Ges. Wiss. Zu Gött. Math.-Phys. Kl. 1918 (1918) 98–100.

[73] P.P. Simeonova, N. Opopol, M.I. Luster, Nanotechnology - Toxicological Issues and Environmental Safety, Springer Science & Business Media, 2007.

[74] Optical Properties and Electronic Structure of Amorphous Germanium - Tauc - 1966 - physica status solidi (b) - Wiley Online Library, (n.d.). https://onlinelibrary.wiley.com/doi/abs/10.1002/pssb.19660150224 (accessed July 29, 2018).

[75] D.G. Barton, M. Shtein, R.D. Wilson, S.L. Soled, E. Iglesia, Structure and Electronic Properties of Solid Acids Based on Tungsten Oxide Nanostructures, J. Phys. Chem. B. 103 (1999) 630–640. doi:10.1021/jp983555d.

[76] A.E. Morales, E.S. Mora, U. Pal, Use of diffuse reflectance spectroscopy for optical characterization of un-supported nanostructures, (2007) 5.

[77] F.F. Abdi, R. van de Krol, Nature and Light Dependence of Bulk Recombination in Co-Pi-Catalyzed BiVO4 Photoanodes, J. Phys. Chem. C. 116 (2012) 9398–9404. doi:10.1021/jp3007552.

[78] M.F. Daniel, B. Desbat, J.C. Lassegues, B. Gerand, M. Figlarz, Infrared and Raman study of WO3 tungsten trioxides and WO3, xH2O tungsten trioxide tydrates, J. Solid State Chem. 67 (1987) 235–247. doi:10.1016/0022-4596(87)90359-8.

[79] J. Díaz-Reyes, V. Dorantes-García, A. Pérez-Benítez, J.A. Balderas-López, Obtaining of films of tungsten trioxide (WO3) by resistive heating of a tungsten filament, (2008) 6.

[80] V. Cristino, S. Caramori, R. Argazzi, L. Meda, G.L. Marra, C.A. Bignozzi, Efficient Photoelectrochemical Water Splitting by Anodically Grown WO3 Electrodes, Langmuir. 27 (2011) 7276–7284. doi:10.1021/la200595x.

[81] M. Gotić, M. Ivanda, S. Popović, S. Music, Synthesis of tungsten trioxide hydrates and their structural properties, Mater. Sci. Eng. B. 77 (2000) 193–201. doi:10.1016/S0921-5107(00)00488-8.

[82] S.E. Mrabet, M.D. Abad, C. López-Cartes, D. Martínez-Martínez, J.C. Sánchez-López, Thermal Evolution of WC/C Nanostructured Coatings by Raman and In Situ XRD Analysis, Plasma Process. Polym. 6 (n.d.) S444–S449. doi:10.1002/ppap.200931004.

[83] G.L. Frey, A. Rothschild, J. Sloan, R. Rosentsveig, R. Popovitz-Biro, R. Tenne, Investigations of Nonstoichiometric Tungsten Oxide Nanoparticles, J. Solid State Chem. 162 (2001) 300–314. doi:10.1006/jssc.2001.9319.

[84] M.P. Thi, G. Velasco, Raman study of WO3 thin films, Solid State Ion. 14 (1984) 217–220. doi:10.1016/0167-2738(84)90101-2.

[85] C.V. Ramana, S. Utsunomiya, R.C. Ewing, C.M. Julien, U. Becker, Structural Stability and Phase Transitions in WO3 Thin Films, J. Phys. Chem. B. 110 (2006) 10430–10435. doi:10.1021/jp056664i.

[86] A. Takase, K. Miyakawa, Raman Study on Sol-Gel Derived Tungsten Oxides from Tungsten Ethoxide, Jpn. J. Appl. Phys. 30 (1991) L1508. doi:10.1143/JJAP.30.L1508.